

# AN ABSTRACT OF THE DISSERTATION OF

Aaron A. Kriss for the degree of Doctor of Philosophy in Radiation Health Physics  
presented on June 3, 2004.

Title: A Beta Dosimeter and Spectrometer Utilizing Plastic Scintillators and a Large-  
Area Avalanche Photodiode.

Abstract approved:

---

David M. Hamby

The purpose of this research was to develop and test a radiation detector to perform beta dosimetry and spectroscopy. The detector utilizes plastic scintillator volumes to produce scintillation light in proportion to the amount of energy deposited in them, and a large-area avalanche photodiode to convert the light to electrical signals. Pulse processing electronics transform the electrical signals into a format useful for analysis, and various software programs are used to analyze the resulting data. The detector proved capable of measuring dose, as compared to Monte Carlo n-Particle simulations, to within about 50% or better, depending on geometry and source type. Spectroscopy results, in conjunction with MCNP-based spectral enhancement methods, proved the detector capable of recording beta spectra with endpoint energies greater than about 250 keV. The detector shows promise for further development as a portable beta detector for field use in beta-contaminated areas.

©Copyright by Aaron A. Kriss  
June 3, 2004  
All Rights Reserved

A Beta Dosimeter and Spectrometer Utilizing Plastic Scintillators and a Large-Area  
Avalanche Photodiode

By  
Aaron A. Kriss

A DISSERTATION

Submitted to  
Oregon State University

In partial fulfillment of  
The requirements for the  
degree of

Doctor of Philosophy

Presented June 3, 2004

Commencement June 2005

Doctor of Philosophy dissertation of Aaron A. Kriss

presented on June 3, 2004.

APPROVED:

---

Major Professor, representing Radiation Health Physics

---

Head of the Department of Nuclear Engineering and Radiation Health Physics

---

Dean of the Graduate School

I understand that my dissertation will become part of the permanent collection of Oregon State University libraries. My signature below authorizes release of my dissertation to any reader upon request.

---

Aaron A. Kriss, Author

## ACKNOWLEDGEMENTS

This research was made possible through a U. S. Department of Energy funded Nuclear Engineering Education Research (NEER) grant, number 02ID14331, administered by Idaho National Engineering and Environmental Laboratory (INEEL). The author is grateful for the opportunity made possible by this grant.

The author also wishes to express his appreciation to the following people, without whom this research could not have been completed: Professor David M. Hamby, for guiding the course of this work; the members of my committee, who answered my questions and provided useful advice; Dr. Scott Menn, who shared his expertise with me; Professors Palmer and Binney, for assistance with MCNP; and to Steve Smith, who built many of the devices I needed to carry out this research, and who was a sounding board for many of my ideas.

Your help was of the utmost importance.

# TABLE OF CONTENTS

	<u>Page</u>
1 Introduction.....	1
1.1 Historical background.....	1
1.2 Background of the research.....	2
1.3 Overview of the research.....	4
1.4 Objectives of the research.....	6
1.5 Significance of the research.....	6
2 Fundamentals of Beta Radiation.....	7
2.1 Theory of beta decay.....	7
2.2 Interaction of betas with matter.....	11
2.3 Effects of beta radiation on tissue.....	14
2.4 Empirical beta dose calculation.....	15
3 Review of the literature.....	17
3.1 Theoretical beta dosimetry.....	17
3.2 Beta dosimetry and spectroscopy with plastic scintillators.....	17
3.3 Avalanche photodiodes and large-area avalanche photodiodes	21
4 Materials and Methods.....	27
4.1 Scintillators.....	27
4.1.1 Scintillation theory.....	27
4.1.2 Scintillator properties.....	29
4.2 Photodiodes and avalanche photodiodes.....	34
4.2.1 Diode structure.....	34
4.2.2 Photodiodes.....	35
4.2.3 Avalanche photodiodes.....	35

## TABLE OF CONTENTS (Continued)

	<u>Page</u>
4.2.4 Large-area avalanche photodiodes.....	36
4.3 Large-area avalanche photodiode module.....	40
4.4 Beta sources and auxiliary equipment.....	45
4.4.1 Sources.....	45
4.4.2 Source holder and spacers.....	46
4.4.3 Scintillator-LAAPD coupling.....	47
4.5 Pulse processing.....	49
4.6 Energy calibration.....	51
4.7 Data processing.....	58
4.8 Dose calculation methodology.....	59
4.9 Monte Carlo N-Particle modeling.....	62
4.10 Spectral enhancement.....	65
4.10.1 Overview.....	65
4.10.2 Analysis.....	68
4.10.3 Modeling the AFED effect.....	75
4.10.4 AFED removal algorithm.....	79
4.10.5 Algorithm implementation.....	80
5 Results.....	83
5.1 Dosimetry.....	83
5.2 Spectroscopy.....	99
5.3 Spectral enhancement.....	103
6 Discussion.....	106
6.1 Factors affecting the results.....	106
6.1.1 Background radiation.....	106
6.1.2 Cerenkov radiation.....	107

## TABLE OF CONTENTS (Continued)

	<u>Page</u>
6.1.3 Direct LAAPD interactions.....	107
6.1.4 Handling background, Cerenkov, and direct interactions...	109
6.1.5 Instrumentation noise.....	109
6.2 Dosimetry.....	112
6.3 Spectroscopy.....	117
6.4 Spectral enhancement.....	119
7 Conclusions.....	124
Bibliography.....	128
Appendices.....	136
Appendix A MCNP input files.....	137
Appendix B Mathematica program for implementing the AFED removal algorithm.....	152



## LIST OF FIGURES

<u>Figure</u>	<u>Page</u>
2.1 Theoretical emission spectrum of $^{14}\text{C}$ .....	10
2.2 Theoretical emission spectrum of $^{204}\text{Tl}$ .....	10
2.3 Theoretical emission spectrum of $^{210}\text{Bi}$ .....	11
4.1 The emission spectrum for BC-430 plastic.....	30
4.2 Scintillator geometry for beta dose measurement.....	31
4.3 Beveled-edge LAAPD.....	37
4.4 Electric field profile across the LAAPD.....	37
4.5 The LAAPD module.....	41
4.6 High voltage versus gain curve for the LAAPD module.....	43
4.7 High voltage (lower curve) and temperature v. time.....	44
4.8 Pulse shape from the LAAPD module.....	45
4.9 Beta source holder (aluminum).....	46
4.10 Measurement geometry.....	47
4.11 Diagram of the scintillator assembly.....	48
4.12 Block diagram of pulse processing instrumentation.....	52
4.13 LAAPD module output.....	53
4.14 142A preamp output.....	53
4.15 Signal from the Ortec 460 delay line amplifier output with 0.1 microsecond integration constant and gain at about 12.....	54
4.16 Output from the stretcher, Ortec 442.....	54

## LIST OF FIGURES (CONTINUED)

<u>Figure</u>	<u>Page</u>
4.17 Output from the Ortec 427A delay amplifier, 2 V amplitude and 1.5 microseconds width.....	55
4.18 Cs-137 spectrum showing the peak (at about 600 keV) from the 624 keV conversion electrons.....	56
4.19 Compton edges from Cs-137 and Co-60.....	58
4.20 Profile of the MCNP simulation geometry (not to scale).....	65
4.21 Geometry used to analyze the AI effect.....	70
4.22 Energy deposition spectrum for 100 keV electrons incident on the scintillator at various angles.....	70
4.23 Energy deposition spectrum for 1 MeV electrons incident on the scintillator at various angles.....	71
4.24 At any energy, a greater angle of incidence will result in a higher probability of scatter leading to a FED event: there is more empty space to scatter into.....	72
4.25 Profile of the MCNP geometry used to analyze the AI effect, including edge effects.....	73
4.26 An example of spectra with, and without, the AI effect present.....	74
4.27 Energy spectra for monoenergetic electrons from point isotropic sources of energies 300 keV and 1 MeV, incident on the scintillator.....	78
4.28 Fractional deposition values at 300 keV, for kernels covering the range 400 to 2300 keV.....	79
5.1 Cl-36 surface dose spectrum at source-detector distance (SDD)=5 mm..	85
5.2 Cl-36 surface dose spectrum at SDD = 10 mm.....	85
5.3 Cl-36 surface dose spectrum at SDD = 20 mm.....	86

## LIST OF FIGURES (CONTINUED)

<u>Figure</u>	<u>Page</u>
5.4 Cl-36 surface dose spectrum at SDD = 30 mm.....	86
5.5 Bi-210 surface dose spectrum for SDD = 5 mm.....	87
5.6 Bi-210 surface dose spectrum for SDD = 10 mm.....	87
5.7 Bi-210 surface dose spectrum for SDD = 20 mm.....	88
5.8 Bi-210 surface dose spectrum for SDD = 30 mm.....	88
5.9 Sr/Y-90 surface dose spectrum for SDD = 5 mm.....	89
5.10 Sr/Y-90 surface dose spectrum for SDD = 10 mm.....	89
5.11 Sr/Y-90 surface dose spectrum for SDD = 20 mm.....	90
5.12 Sr/Y-90 surface dose spectrum for SDD = 30 mm.....	90
5.13 Cl-36 shallow dose spectrum for SDD = 5 mm.....	91
5.14 Cl-36 shallow dose spectrum for SDD = 10 mm.....	91
5.15 Cl-36 shallow dose spectrum for SDD = 20 mm.....	92
5.16 Cl-36 shallow dose spectrum for SDD = 30 mm.....	92
5.17 Bi-210 shallow dose spectrum for SDD = 5 mm.....	93
5.18 Bi-210 shallow dose spectrum for SDD = 10 mm.....	93
5.19 Bi-210 shallow dose spectrum for SDD = 20 mm.....	94
5.20 Bi-210 shallow dose spectrum for SDD = 30 mm.....	94
5.21 Sr/Y-90 shallow dose spectrum for SDD = 5 mm.....	95
5.22 Sr/Y-90 shallow dose spectrum for SDD = 10 mm.....	95
5.23 Sr/Y-90 shallow dose spectrum for SDD = 20 mm.....	96

## LIST OF FIGURES (CONTINUED)

<u>Figure</u>	<u>Page</u>
5.24 Sr/Y-90 shallow dose spectrum for SDD = 30 mm.....	96
5.25 Sr/Y-90 measured spectrum and theoretical emission spectrum.....	100
5.26 Cl-36 measured spectrum and theoretical emission spectrum.....	100
5.27 Bi-210 measured spectrum and theoretical emission spectrum.....	101
5.28 Carbon-14 spectrum recorded by direct interaction in the LAAPD.....	102
5.29 Technetium-99 spectrum recorded by direct interaction in the LAAPD.....	102
5.30 Carbon-14 spectrum, before and after processing, compared to theoretical emission spectrum.....	103
5.31 Chlorine-36 spectrum, before and after processing, compared to theoretical emission spectrum.....	104
5.32 Yttrium-90 spectrum, before and after processing, compared to theoretical emission spectrum.....	104
5.33 Application of the algorithm to a measured $^{90}\text{Sr}/^{90}\text{Y}$ spectrum.....	105
6.1 Surface dose efficiencies.....	113
6.2 Shallow dose efficiencies.....	113
6.3 Chlorine-36 spectrum showing the influence of mylar encapsulation and air on the MCNP modeled spectrum.....	122
6.4 Effect of processing a Strontium/Yttrium-90 spectrum that included the effects of mylar encapsulation and air.....	122

## LIST OF TABLES

<u>Table</u>	<u>Page</u>
4.1 Properties of BC-430 plastic scintillator.....	30
4.2 Properties of BC-802.....	31
4.3 Parameters used to calculate light collection efficiency from the scintillator.....	33
4.4 Operating parameters of the LAAPD module.....	42
4.5 Beta source properties.....	46
4.6 NIM bin modules and settings.....	55
4.7 Comparison of MCNP beta doses to establish tissue-equivalency of PVT plastic scintillator for beta dosimetry.....	61
4.8 Structure parameters for MCNP modeling.....	65
4.9 Example of data calculated from a mono-energetic, isotropic, electron point source incident on the scintillator.....	77
4.10 The 600 keV and 700 keV kernels were calculated using MCNP.....	82
5.1 Measured and modeled surface doses (mGy) at several source-detector distances for $^{90}\text{Sr}/^{90}\text{Y}$ .....	97
5.2 Measured and modeled surface doses (mGy) at several source-detector distances for $^{36}\text{Cl}$ .....	97
5.3 Measured and modeled surface doses (mGy) at several source-detector distances for $^{210}\text{Bi}$ .....	97
5.4 Measured and modeled shallow doses (mGy) at several source-detector distances for $^{90}\text{Sr}/^{90}\text{Y}$ .....	98
5.5 Measured and modeled shallow doses (mGy) at several source-detector distances for $^{36}\text{Cl}$ .....	98

## LIST OF TABLES (CONTINUED)

<u>Table</u>	<u>Page</u>
5.6 Measured and modeled shallow doses (mGy) at several source-detector distances for $^{210}\text{Bi}$ .....	98
6.1 Efficiency calculated as a function of energy range for $^{90}\text{Sr}/^{90}\text{Y}$ .....	111
6.2 Efficiency calculated as a function of energy range for $^{36}\text{Cl}$ .....	112
6.3 Endpoint energy losses through mylar encapsulation and air for several radionuclides.....	118

## LIST OF APPENDIX FIGURES

<u>Figure</u>	<u>Page</u>
A.1 Strontium-90 spectroscopy configuration.....	138
A.2 Chlorine-36 spectroscopy configuration.....	139
A.3 Bismuth-210 spectroscopy input file.....	140
A.4 Yttrium-90 spectroscopy input file.....	141
A.5 Strontium-90 surface dose MCNP input file.....	142
A.6 Chlorine-36 surface dose MCNP input file.....	143
A.7 Bismuth-210 surface dose MCNP input file.....	144
A.8 Yttrium-90 surface dose MCNP input file.....	145
A.9 Strontium-90 shallow dose MCNP input file.....	146
A.10 Chlorine-36 shallow dose MCNP input file.....	147
A.11 Bismuth-210 shallow dose MCNP input file.....	148
A.12 Yttrium-90 shallow dose MCNP input file.....	150
A.13 Kernel calculation MCNP input file.....	151

# **A BETA DOSIMETER AND SPECTROMETER UTILIZING PLASTIC SCINTILLATORS AND A LARGE-AREA AVALANCHE PHOTODIODE**

## **1 INTRODUCTION**

### ***1.1 Historical background***

After Becquerel observed the mysterious fogging of his photographic plates in 1896 when they were in close proximity to, but opaquely separated from, uranium salts, he postulated the existence of some new “radiation effect”, unrelated to any other known sort: i.e., radioactivity (Brown 2002). Becquerel had made a momentous discovery, but he did not understand the physics underlying what was occurring. This was to be expected, since Roentgen had only discovered x rays the year before. Thomson, at the Cavendish Laboratory, would not definitively discover the electron until the following year (Brown 2002). It was not until Rutherford and Soddy made the revolutionary assertion early in the 20th century that Becquerel’s mysterious radiation was in fact the product of the transformation of certain elements into different elements, that an understanding of the phenomenon of radioactivity was born (Brown 2002). The doors to discovery were wide open. So were the doors to a whole new kind of health hazard.

Roentgen’s x ray discovery took very little time to make its way around the globe, and very little more to become a medical tool. In the meantime, basic research related to radioactivity took center stage in the work of the Curies and others. The research took place in an environment where little or no thought was given to safety, not



because the researchers were careless, but because they were not aware of ionizing radiation's biological hazards. There were clues, though.

Researchers had noted the ulcerating effect of x-rays after 1895 (Brown 2002). In 1903 Rutherford noticed that the hands of Pierre Curie, as he held a flask of glowing radium, were scarred. Curie had a difficult time handling the flask due to the radiation burns. Becquerel also suffered a chest burn from a small flask of radium, given to him by the Curies, that he had held in a vest pocket for a length of time. Radium is an intense gamma emitter, and it is the gamma phenomenon that initially drew all the attention related to safety. In many ways, at least for external exposures, this is still true. It is not hard to understand why: the deep penetration capabilities of gammas and x-rays make them the most important of the non-neutron radiations in matters of external safety. Under certain conditions, however, short-range charged particle radiations, such as the beta (a name given by Rutherford before 1900 to the then-mysterious charged radiation), become important in external radiation protection.

## ***1.2 Background of the research***

Protection against betas is usually a simple matter of interposing a thin layer of low-Z material between source and target. But if the goal is to measure beta dose rates, from an accident, for example, or identify unknown radionuclides, instruments specially built for the purpose are required.

This amounts to quantifying, in some way, the energy of the beta and, for dosimetry purposes, where it deposits its energy. There are many ways to do this (Knoll

2000). One approach is to analyze the light produced when beta particles traverse a scintillator. With the proper tools and analysis, the scintillation light can be employed to determine not only the beta spectrum, and thus the radionuclide's identity, but also the dose delivered by the betas to some mass of interest.

The triple phoswich (TPS) design is one approach to analyzing beta spectra (Bush-Goddard 2000). The concept involves layering three scintillators on top of a photomultiplier tube. Low-energy betas will stop in the first layer, intermediate betas in the second layer, and high-energy betas in the third layer. Each scintillator has a unique scintillation decay time. By analyzing the decay time of the photomultiplier's output, some conclusions can be reached as to which layer produced the signal. This provides a quantitative idea of the energy range of the betas incident on the detector.

Dose from ionizing radiation is defined as energy imparted to mass, divided by that mass (Attix 1986). The design of the TPS made it difficult to extract dose information directly from the data. The face of the detector is relatively large, which makes it difficult to achieve uniform irradiation conditions using small point sources. Also, one of the scintillators is an inorganic type with a density considerably different than human tissue, which adds complexity to dose calculations. Finally, the differing light output of each scintillator, in photons per MeV of energy deposited, creates a scenario whereby the total output from the photomultiplier cannot be related linearly to energy deposited. Through the application of sophisticated digital signal capture and analysis equipment, it may be possible to extend the usefulness of the TPS design to dose measurements at some future date.

An extension of the TPS design was conceived to overcome the difficulties described above. Instead of analyzing the scintillators' timing properties, their scintillation emission wavelengths would form the basis for determining the energy deposited in any one layer. The three layers would be tissue-equivalent plastics, each emitting scintillation light of distinct wavelengths. An optical filter system would separate the wavelengths and direct the light to individual photomultipliers or photodiodes. This would provide a quantitative determination of the amount of energy deposited in each layer, since each scintillator could be calibrated independently with respect to photons emitted per MeV of energy deposited. Unfortunately, though three plastic scintillators were found that emitted light at wavelengths sufficiently far apart to allow optical separation, the nature of the scintillation process precluded this idea from coming to fruition. Two of the three scintillators were of the wave-shifting type; that is, the original scintillation photons were re-absorbed by the scintillator and emitted at a longer wavelength. In practice, this meant an original photon from one scintillator might interact in another scintillator and cause a secondary emission, thus eliminating the ability to tell which photon belonged to which scintillator. This prompted the design for the instrument ultimately used in this research.

### ***1.3 Overview of the research***

By building a scintillator with specific dimensions corresponding to a mass distribution of interest, for example a layer of skin, dose to that mass can be inferred by quantifying the light output from the scintillator. From the light output, the energy

imparted to the scintillator can be determined, and if the scintillator has characteristics that are closely tissue-equivalent (density close to water and atomic composition near to that of tissue), then dose can be calculated by dividing energy by mass.

Because of the difficulties encountered in using combinations of scintillators, such as those described above, it was decided instead to use a single scintillator type, in various geometries (described in full in Materials and Methods), to achieve the goal of measuring beta dose and spectra. Plastic scintillators meet the requirements of tissue equivalency and can be employed for measuring beta spectra. Since plastic scintillator material can be easily shaped to nearly any specification, a plastic scintillator was chosen for this research.

In addition to creating unique scintillator shapes for dosimetry and spectroscopy, the use of a large-area avalanche photodiode (LAAPD) was explored for detecting the scintillation light. The LAAPD is a solid-state alternative to the photomultiplier tube. It is incorporated into a module that allows gain adjustment and that controls unwanted temperature-induced gain changes. The LAAPD can also serve as a direct detector of beta radiation, in the absence of a scintillator. Its usefulness in this regard is also examined in this research.

Finally, Monte Carlo methods have been developed to enhance the recorded beta spectra. The particular geometry of a detector system has an effect on the spectral results. A way has been found to filter unwanted spectral deformations caused by the way betas interact with the detector, in the measurement geometry used.

### ***1.4 Objectives of the research***

This research will extend the current level of capability for analyzing beta spectra and beta dose, by development of a new, dual-purpose beta detector. The device will serve alternately as a dosimeter and a spectrometer, by utilizing near tissue-equivalent plastic scintillator material in precise configurations, coupled to a large area avalanche photodiode. The photodiode will also serve as a direct beta interaction spectrometer. Efforts will also be made to enhance measured spectra, accounting for various physical phenomena that degrade the measured beta spectra.

### ***1.5 Significance of the research***

Beta particles take a back seat to gamma rays in the area of external radiation protection, for the simple reason that betas are far more easily protected against. Thus, betas pose a lesser hazard. However, there are cases in which betas constitute a danger. For example, large-scale accidents on the order of Chernobyl may result in considerable beta emitter distribution, as may a terrorist “dirty” bomb. In these cases, the ability to quickly acquire an accurate dose estimate, as well as an analysis of the fallout’s composition, will be of significant value. Our device is designed to provide this capability.

## 2 FUNDAMENTALS OF BETA RADIATION

### 2.1 Theory of Beta Decay.

The beta decay process involves the transformation of a nuclear neutron into a proton, for negatron emission, and a proton into a neutron, for positron emission. Each process, in order to conserve energy and momentum, produces another particle: the neutrino for positron emission, and the antineutrino for negatron emission. The processes are summarized by:

$$\begin{aligned} n &\rightarrow p + \beta^- + \bar{\nu} \\ p &\rightarrow n + \beta^+ + \nu \end{aligned} \quad [2.1]$$

A competing process for positron decay is electron capture, whereby an orbital electron is captured by the nucleus. The result is the same for both processes, though the initial conditions that permit either electron capture or positron decay differ. Electron capture is not considered further.

In terms of energy, negatron emission occurs if the following energy value is positive:

$$E = [M_{Z,A} - M_{Z+1,A}]c^2 \quad [2.2]$$

This energy represents the energy of the negatron decay process (beta energy plus neutrino energy), and is simply the difference between the parent atomic mass and daughter atomic mass. For positron emission, the equivalent condition is

$$E = [M_{Z,A} - M_{Z-1,A} - 2m]c^2 \quad [2.3]$$

where  $m$  is the electron rest mass. Positron emission is less common than negatron emission since positron emitters must be produced deliberately (i.e. from accelerators)

whereas negatron emitters are found in many fission products. Since only negatron emitting nuclides are used in this research, it is understood from this point on that the term “beta” refers exclusively to negatron emitters.

The complex interplay between the beta particle and its antineutrino determines the shape of the beta energy spectrum. In 1934 Enrico Fermi set forth the basic equations that determine beta spectra shapes [Cottingham and Greenwood 1986]. Subsequent experiments verified the equations’ accuracy. The equation that predicts beta spectra shapes is

$$N(W) = p \cdot W \cdot (W_0 - W)^2 \cdot F(Z, W) \cdot a_n(Z, W) \quad [2.4]$$

where

$W$  is the total energy of the electron in units of  $m_e c^2$ ,

$W_0$  is the total energy at the maximum kinetic energy,

$p$  is the beta’s momentum in units of  $m_e c$ ,

$m_e$  is the electron mass,

$c$  is the speed of light,

$Z$  is the daughter nucleus’ atomic number,

$F(Z, W)$  is the Fermi factor, which accounts for the Coulomb force between the beta and the daughter nucleus,

and  $a_n(Z, W)$  is called the shape factor, which relates to the “forbiddenness” of the transition. When  $a_n(Z, W)$  equals 1, the spectrum is “allowed” (ICRU 56 1994).

The terms “allowed” and “forbidden” are a bit misleading, since even forbidden decays are clearly occurring. The nomenclature actually refers to a state whereby a beta decay is forbidden from following one set of rules and instead must follow another. Fundamentally, the change in nuclear spin in going from the parent to the daughter by beta decay determines whether a process is forbidden or allowed, and also determines the degree of forbiddenness.

The Fermi factor and shape factor can be calculated from complex expressions. As the atomic number increases, the Fermi factor must be adjusted to take into account screening by atomic electrons and deviations due to nuclear size (ICRU 1994).

Fortunately, libraries of beta spectrum data are available that include hundreds of beta emitters (Cross 1983, RADAR 2003)]. Beta spectrum shapes vary widely, depending on the quantum properties of the nuclei involved. Figures 2.1 through 2.3 illustrate some of the variability in beta spectra.



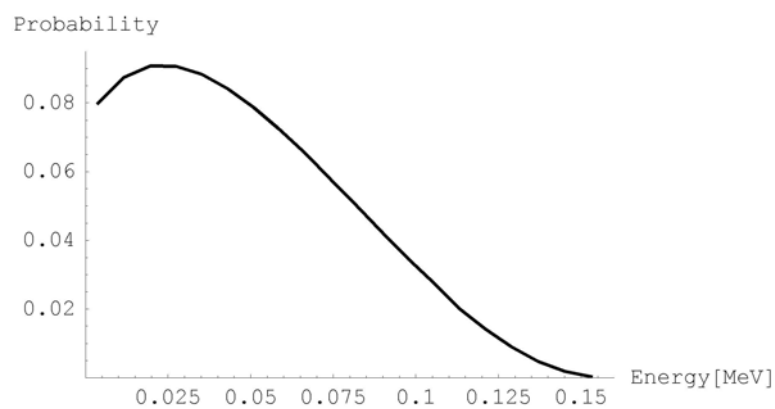


Fig. 2.1. Theoretical emission spectrum of  $^{14}\text{C}$ .

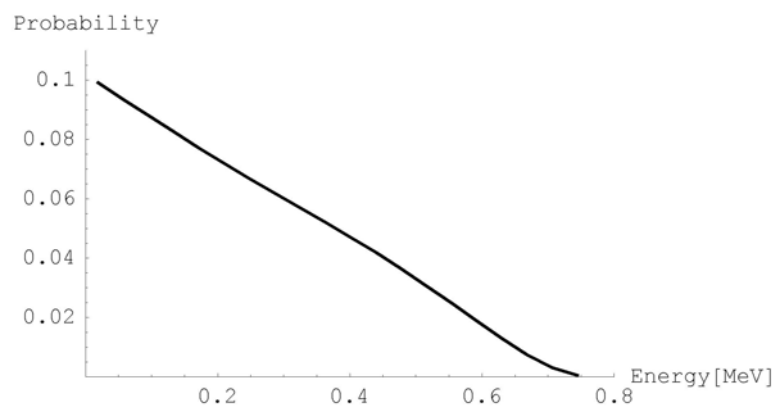


Fig. 2.2. Theoretical emission spectrum of  $^{204}\text{Tl}$ .

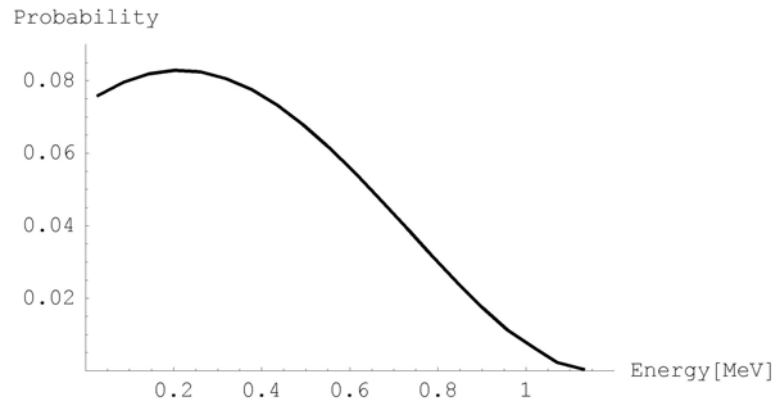


Fig. 2.3. Theoretical emission spectrum of  $^{210}\text{Bi}$ .

## 2.2 Interaction of betas with matter

Since betas are charged particles, they interact continuously with the Coulomb field of the matter through which they pass. These interactions fall into several categories: elastic collisions with atomic electrons, elastic collisions with atomic nuclei, inelastic collisions with atomic electrons, and inelastic collisions with atomic nuclei (Evans 1955). Each of these interactions has a different consequence for the incident beta.

Elastic collisions between an incident beta and atomic electrons may result in a deflection of the incident beta, but typically result in an insignificant energy loss. Only very-low-energy betas, less than 100 eV, are significantly affected (Evans 1955).

Elastic nuclear scattering is very likely for incident betas. The result is a change in direction of the beta, but only the loss of enough kinetic energy to conserve momentum (Evans 1955). Elastic nuclear scattering is the primary reason electrons

follow unpredictable paths. The cross section for elastic nuclear scatter is proportional to  $Z^2$  (Attix 1986).

Inelastic collisions between a beta and atomic electrons are the primary mechanisms for energy loss by a beta in matter. The collisions may result in ionization or excitation of the atomic electrons, followed possibly by emission of fluorescence x-rays or Auger electrons. The struck electron, if removed from the nucleus, becomes a secondary, or “knock-on”, electron. The secondary electron’s behavior is then governed by the same rules that apply to the incident beta.

Inelastic collisions between betas and atomic electrons can be categorized by differentiating between collisions that occur at a distance (impact parameter  $\gg$  atomic radius) and those that occur in close proximity (impact parameter  $\sim$  atomic radius) (Attix 1986). The former are characterized as “soft” collisions, the latter as “hard” collisions. The total energy loss experienced by the incident betas is about equal from hard and soft collisions, though soft collisions are considerably more common (Attix 1986).

Inelastic nuclear collisions will deflect the incident beta, with an accompanying loss of kinetic energy. Depending on the circumstances, this energy loss may result in the emission of a bremsstrahlung x-ray (Evans 1955). The cross section for bremsstrahlung production is proportional to  $Z^2$  and inversely proportional to the square of the beta’s mass. For low-Z materials, such as scintillator plastic and tissue, bremsstrahlung production is insignificant. Inelastic collisions account for only 2 to 3% of all beta – nucleus collisions; the remainder are elastic (Attix 1986).

The term “stopping power” is used to describe the rate at which an electron loses energy in matter. It has units of energy per unit length, typically MeV per centimeter. The “mass” stopping power is a related term, derived by dividing the stopping power by the matter’s density. Typical units are MeV cm<sup>2</sup>/g. Stopping power can be divided into two constituents: collision stopping power, and radiative stopping power. The collision component accounts for energy losses that do not involve a loss of energy due to radiative emission, whereas the radiative component usually refers to the energy lost via bremsstrahlung x-rays. For low-Z materials, the radiative component is a small fraction of the total stopping power. The collision term may be subdivided into hard and soft components (Attix 1986). The expression for mass collision stopping power is

$$\left( \frac{dT}{\rho dx} \right)_c = k \left[ \ln \left( \frac{\tau^2(\tau + 2)}{2(I/m_0c^2)^2} \right) + F(\tau) - \delta - \frac{2C}{Z} \right] \quad [2.5]$$

where

$$F(\tau) \equiv 1 - \beta^2 + \frac{\tau^2/8 - (2\tau + 1)\ln 2}{(\tau + 1)^2} \quad [2.6]$$

$I$  is the mean excitation potential of the medium,  $\tau$  is the ratio of kinetic energy to rest energy,  $\beta$  is the ratio of particle velocity to the speed of light,  $C/Z$  is a correction term related to the shell correction,  $\delta$  corrects for the polarization effect, and  $k$  is a combination of charge, mass, and velocity terms (Attix 1986). Extensive tables of stopping power values exist for numerous materials and energies (Attix 1986, NIST 2003).

The range of a beta in matter must be carefully defined. Since betas follow a winding path, the farthest distance they penetrate into matter will not necessarily correspond to the total path length. The total path length is what is defined as “range”. A common measure of range is known as the continuous slowing down approximation range, or CSDA range. This is defined as the integral of the inverse of the mass stopping power, integrated over the energy interval from zero to the maximum beta energy. The units are in  $\text{g cm}^{-2}$ . A variety of empirical expressions exist to allow calculation of the penetration depth of electrons in matter (Martin 2000, Cember 1992). For betas, it turns out that the maximum depth of penetration and the CSDA range are quite close for low-Z materials. Since extensive tables of CSDA range are available, this is convenient for calculations that require knowledge of the maximum penetration depth (Attix 1986, NIST 2003).

### ***2.3 Effects of beta radiation on tissue***

The tissue most affected by external beta radiation is the skin. Most beta particles, even those having several MeV of kinetic energy, do not penetrate farther than the lower layer of skin. The overall effect depends on energy and quantity, and also varies depending on which part of the body the skin is irradiated. The energy lost in the skin is governed by the interactions described in the previous section.

The skin is divided into two major layers, the epidermis (outer layer) and the dermis. The epidermis is in turn subdivided into a basal layer of dividing cells, and between 10 and 20 layers of differentiating and keratinizing cells. The outermost few

layers, comprising the stratum corneum, are dead. The total thickness of the epidermis ranges from 30 to 300 microns, depending on location, with an average thickness of 100 microns. The dermis consists of connective tissue, rich with blood vessels, that ranges from 1 to 3 mm thick. The basal layer of the epidermis and the blood vessels and fibroblasts in the dermis are the primary recipients of radiation damage (Hall 2000).

Betas of sufficiently low energy will not penetrate the stratum corneum, and hence will not have any damaging effect. Assuming a total depth of 3 mm for the epidermis and dermis together, a beta would need over 0.8 MeV of energy to penetrate beyond the skin. For most beta emitters of interest, therefore, the majority of energy lost as the beta progresses will be in the skin. If sufficient dose is delivered to the basal layer, the basal cells will die and the skin will be lost. Provided the damage does not extend over the entire body, skin can be regenerated from neighboring intact areas. Skin reddening is common at high doses, due to capillary damage in the dermis (Hall 2000). Long-term effects, primarily skin cancer, may occur due to beta exposure.

## ***2.4 Empirical beta dose calculation***

A common technique for determining beta dose to a specified depth in tissue is described in Martin (2000). Given a flux of betas  $\phi_\beta$  [ $\beta \text{ cm}^{-2} \text{ s}^{-1}$ ] from an emitter of maximum energy  $E_{max}$  [MeV] and average energy  $\bar{E}$  [MeV], and having calculated an effective attenuation coefficient  $\mu_\beta$  [ $\text{cm}^2 \text{ g}^{-1}$ ], the beta dose at skin surface is given by

$$\dot{D}_\beta = 5.8 \times 10^{-5} \cdot \phi_\beta \cdot \bar{E} \cdot \mu_\beta \quad [2.7]$$

in units of rads/hour. The effective attenuation coefficient is calculated from empirically derived formulas; there are separate formulas for air, tissue, and one for all other materials. Since the dose just at skin surface is not very useful, the above expression is usually modified to calculate dose at some depth, by attaching an exponential term that accounts for attenuation in tissue. Another exponential term might be attached to account for attenuation in air.

This sort of method is of limited use at best. It requires knowledge of the flux, which may be non-uniform, knowledge of the maximum energy, and a certain amount of faith that the effective attenuation coefficients are appropriate to the situation. Under circumstances where beta exposures are in a known geometry, with a known emitter, and with a uniform flux, this method may provide a reasonable estimate of the beta dose.

### 3 REVIEW OF THE LITERATURE

#### ***3.1 Theoretical beta dosimetry***

The ICRU categorizes theoretical beta dosimetry by technique. These include analytical or deterministic methods, Monte Carlo methods, tables of absorbed dose distributions, derived computer methods such as VARSKIN, and empirical expressions for absorbed dose distributions (ICRU 1994). Loevinger developed empirical formulas for beta dose distributions around point sources based on apparent attenuation coefficients and the average and maximum beta energies (1950, 1954, 1956). Cross extended this work by more accurately modeling the parameters that defined Loevinger's method (1997). Berger derived point kernels for determining beta dose for situations such as immersion in a radioactive cloud (1974). A number of authors studied beta dose, or more properly electron dose, using Monte Carlo methods (Gualdrini and Padoani 1994; Hirayama 1994). Fell put forth a method for calculating skin dose based on the continuous slowing down approximation (CSDA), from which he derived a semi-empirical point dose function (1991). Kocher and Eckerman formulated electron dose-rate conversion factors for skin exposure for a variety of geometries, based on Berger's work (1981).

#### ***3.2 Beta dosimetry and spectroscopy with plastic scintillators***

Theoretical dose calculations are useful for purely predictive or retrospective analyses, but for real-world situations there must be measurement as well. We can roughly divide beta dose measurement into these categories: dose derived from



spectral measurements, dose derived from “delayed” media such as thermoluminescent dosimeters and film, dose derived from “immediate” media such as scintillators and ion chambers, and dose derived from biological media such as hair diameter and skin erythema levels (ICRU 56 1994). This research involves dosimetry derived from scintillators of specific geometries.

Scintillation dosimeters may be categorized by function: those that are used in medical settings for measuring patient dose, those that are used in lab or work settings to measure occupational dose, and those developed for special research purposes.

In the medical setting, much of the effort has gone into dose measurements of high-energy photon beams (Beddar and others 1992a, 1992b; de Boer and others 1993; Mainardi and others 1997; Clift and others 2000). Though not measuring beta dose, the materials are the same, namely plastic scintillators coupled to a light detector and associated electronics. The complications are also similar, for instance, the need to account for Cerenkov radiation. Not all efforts have been directed towards photon radiation therapy: Bambynek and others (2000) developed a dosimetry system for cardiovascular brachytherapy beta sources using a plastic scintillator, Williamson and others (1998) worked on plastic scintillator response to low-energy photons from brachytherapy sources, as did Kirov and others (1999) and Flühs and others (1996), and de Sousa and others (2000) studied a dosimeter for patients undergoing diagnostic radiology procedures. The primary advantages of plastic scintillator material in all of these cases are its near-water equivalence, a property useful when dose to tissue is desired, and small backscatter factors.

In the lab or workplace, a common technique used to measure beta dose is to first measure the beta spectrum with a scintillator, and then calculate a dose from that information. Martz and others (1986) used a plastic scintillator 2.5 cm diameter by 0.9 cm deep to measure beta spectra and convert those spectra to dose. They used a beta energy deposition function, derived from calibrated sources, to convert the measured spectra to dose at a depth of  $7 \text{ mg/cm}^2$ . Thus, calculation of dose relied not only on direct extrapolation of scintillator light output to dose, but on previously derived calibration curves, in order to isolate the dose to a thin layer at a specific depth. Gammas were excluded by measuring spectra with and without a beta shield. Shen and others (1987) used plastic scintillators to measure spectra, from which they subsequently calculated doses using electron transport theory as applied to TLDs. Swinth and others (1989) constructed a combination proportional counter-plastic scintillation counter for measuring beta spectra and dose. They used coincidence gating to exclude gamma events. Dose was calculated from spectral information and compared to extrapolation chamber data for calibration. Horowitz and others (1993) developed a two-detector telescope device consisting of a thin, front silicon detector and a thick, back plastic scintillator. Again, gamma rejection was accomplished by coincidence analysis. Dose was calculated by comparison to Monte Carlo depth distributions for the spectra measured. Vapirev and others (1996) employed a plastic scintillator to measure beta spectra after passage of the betas through absorbers of various thicknesses. Dose was calculated via specific energy losses,  $dE/dx$ , taken from

ICRU 37, and the spectra. Results were compared to the calculations of Cross and Marr (1960).

Several authors have studied thin plastic scintillators for beta dosimetry. Bingo and others (1980) developed a beta dose survey meter using a 2 mm thick scintillator. The premise was that there existed a certain thickness of scintillator that would satisfy a directly proportional relationship between count rate and dose rate, for all beta energies, i.e. independent of beta energy. Two millimeters happened to be the experimentally determined optimum thickness. Johnson and others (1983) deliberately chose to use a very thin plastic scintillator, backed by a 1 cm thick Lucite light pipe, to measure dose to skin directly. Our device will be similar, except that we will study several configurations of scintillator layers of somewhat greater thickness, and most importantly we will use a large area avalanche photodiode instead of a photomultiplier tube.

Finally, on a somewhat esoteric note, Watt and Alkharam (1995) proposed using extremely thin (20  $\mu\text{m}$ ) plastic scintillators to directly simulate DNA damage, in the sense that the fluor spacing in the scintillator is analogous to the DNA diameter of around 2 nm. So, two scintillation emissions within 2 nm can be considered a double strand break, and thus an indication of dose.

For examples of techniques used to determine beta spectra independently of dose considerations, see Simons and Higginbotham (1990), who developed a beta spectroscopy with gamma discrimination capabilities, and Palazzolo and others

(1992), who built a well-type plastic scintillator with gamma anticoincidence properties.

The theory of beta decay and the expressions predicting beta spectrum shape are covered in Evans (1955) and ICRU 56 (1994). Cross and others (1983) have published beta energy-emission spectral shapes for about 100 nuclides.

For general consideration of scintillation theory and its application to radiation detection, see Knoll (2000). For insight into specific scintillator characteristics such as light yield, see Sysoeva and others (2002), Moszynski and others (1994, 1997a, 1997b) and Dorenbos and others (1995). These papers provide valuable insight into experimental method.

### ***3.3 Avalanche photodiodes and large-area avalanche photodiodes***

McKay and McAfee, of Bell Labs, gave the first account of an electron avalanche process occurring in a semiconductor solid (1953). They observed that by creating a high electric field across a p-n junction electron multiplication took place after injection of an electron. Similar multiplication took place of electrons produced by the photoelectric effect. Though not explicitly interested in possible radiation detection applications of their new device, part of the experimental procedure involved bombarding the semiconductor with alpha particles, with the objective of determining the timing characteristics of the avalanche process. Thus, even in the very earliest days of the solid-state era, avalanche photodiodes had played a role, however inadvertent, in radiation detection.

Johnson, of Texas Instruments, provided evidence that the signal-to-noise and noise-equivalent-power characteristics of diodes biased to breakdown levels appeared to provide the “solid-state analog of the photomultiplier tube” (1965). Again, the focus of his research was not on radiation detection, but rather on communications technology. However, given the importance of the photomultiplier tube in radiation detection, any device that behaved similarly had potential in that field.

McIntyre, of RCA Victor Company, further analyzed the noise characteristics of avalanche diodes (1966). His effort was directed toward understanding the noise generated during the multiplication process, from which he derived an expression for the noise spectral density, for any distribution of injected carriers.

Locker and Huth, of General Electric Company’s Space Sciences Laboratory, first utilized avalanche diodes for radiation detection in 1966 (1966). Their work involved detecting low-energy x rays and protons directly in the diodes, which were only 0.1 cm squared in area. By using suitable electronics they were able to detect x-ray energies as low as 1.49 keV. The authors, with McKinney, extended their research in 1968 to developing a germanium avalanche diode specifically for detecting x rays in the energy range 10-30 keV (Huth and others 1968). Their main observation was on the difficulty of achieving uniform multiplication across the face of the diode, a problem of obvious importance if the diode areas were to be increased significantly.

Webb and McIntyre studied large area reach-through avalanche photodiodes as applied to x-ray spectroscopy at room temperature, limiting themselves to energies between 1.5 and 20 keV (1976). The diode sizes studied were 12 mm<sup>2</sup> and 25 mm<sup>2</sup>

areas, small by current standards, but large for the time. Gain was limited to about 63, and energy resolution was at best 600 eV FWHM for  $^{55}\text{Fe}$ . The various contributors to the noise were studied, such as dark current and gain non-uniformity.

Gelezunas and others studied avalanche photodiodes with areas of 20 and 330  $\text{mm}^2$  (1977). Their focus was on an improved fabrication process for producing uniform gain across the area of the diode, a crucial factor governing the usefulness of large-area devices. They achieved a gain variation of about  $\pm 7\%$  across the diode faces. In addition, their device was of the p-n junction type, as opposed to the reach-through type of Webb and McIntyre, so much larger gains of 400 to 800 were attainable, though at a sacrifice of energy resolution.

Reiff and others covered the basic advantages of large area avalanche photodiodes over photomultiplier tubes (1983). These include ruggedness, high quantum efficiency, light weight and small size, and insensitivity to external magnetic and electric fields. The authors describe their experiments with a 1-inch squared area APD, which they used both coupled to a BGO crystal and directly exposed to low-energy x-rays. It was speculated that such APDs might replace the PMTs in PET scanners, a circumstance that eventually came to pass.

By 1989, Lecomte and others had developed BGO-APD arrays for PET scanners (1989). They achieved energy resolutions of between 16 and 20% for 0.662 MeV gamma rays. In addition, they demonstrated that when coupled to fast plastic detectors, APDs could be used successfully in fast timing measurements.

By the 1990's, research with and about APDs accelerated. Baron and Ruby (1994) investigated the time responses of x-rays detected directly in large-area APDs of various sizes. Of particular value is their description of how the response varies depending on which part of the APD the x-ray deposits its energy. Response times were typically several nanoseconds. Lorenz and others made similar studies (1994). Schmelz and others extended the use of APDs for PET scanners, achieving spatial resolutions of  $2.3 \pm 0.1$  mm, energy resolution of 15%, and time resolution of 2.6 nsec (1995).

From the mid-90s until the present, a significant number of papers directly concerned with the LAAPD design used in this research began to be published. Ochi and others wrote favorably regarding their experiments with a 16 mm diameter LAAPD from Advanced Photonix (1996). They studied performance characteristics such as gain dependence on temperature, and timing. X-ray interactions were examined in CsI(Tl) scintillators coupled to the APDs, as well as directly in the LAAPD. Results were good, with energy resolution as low as 4% for small scintillators. Important results were also obtained proving the strong dependence of gain on ambient temperature; consequently, for stable operation, the LAAPD's temperature must be monitored and held constant, if possible.

Moszynski and various collaborators have been particularly productive in studying LAAPDs from Advanced Photonix. Timing studies involving LSO (lutetium oxyortho-silicate) crystals coupled to LAAPDs of 10 and 16 mm diameter were carried out (Moszynski and others 1996). Response times of less than 20 ns were

measured at a gain of 300. In addition, quantum efficiencies of 55% for the 16 mm diode and 65% for the 10 mm diode were observed. LAAPDs can be configured either with a window or without; the researchers found that the number of e-h pairs produced in the APD was reduced by a factor of 2 with the window in place. For that reason we have chosen to use a window-less version for our work.

Since many scintillators emit light in the UV to blue range, and most APDs are preferentially sensitive to longer wavelengths, development of a blue-sensitive APD would be useful. Just such a blue-enhanced LAAPD was examined (Moszynski and others 1997b). The characteristics of the device were found to be just as good as the non-enhanced versions. Though our scintillator of choice is a long wavelength variety, the blue-enhanced LAAPD is still a better match than the non-enhanced type. Therefore, we chose to use a blue-enhanced version in our research.

Further work with LAAPDs from Advanced Photonix has continued, including very recent work (Moszynski and others 1998; Moszynski and others 2000; Moszynski and others 2001a, 2001b; Moszynski and others 2002; Belogurov and others 2003). The emphasis has gradually shifted from examining the LAAPDs themselves, to simply using them for work on such things as characterizing exotic scintillators at low temperatures. The results of these efforts indicated that LAAPDs could be successfully employed in this research.

Other individuals and groups have employed APDs and LAAPDs. Pansart examined using an APD in high-energy physics experiments (1997). Solovov and others used an LAAPD to examine detection of scintillation light from liquid xenon



(2000). Allier and others did the same for a  $\text{LaCl}_3(\text{Ce}^{3+})$  scintillation crystal (2002). Renker reviewed the properties of APDs and LAAPDs for uses such as high-energy physics, astrophysics and medical imaging (2002). Shi and others studied APDs for use in a tokamak, as soft x-ray detectors (2002). Finally, Rafecas and others incorporated APDs into their small animal PET scanner, the amusingly named MADPET-II (2003).

For a general consideration of semiconductor radiation detectors, see Knoll (2000) and Lutz (1999). For in-depth coverage of semiconductor devices of all sorts, see Sze (1981). A useful source for photonic devices of all kinds, including avalanche photodiodes, is Saleh (1991).

## 4 MATERIALS AND METHODS

### *4.1 Scintillators*

#### **4.1.1 Scintillation theory**

A material is classified as a scintillator if, when its electrons are raised to an excited state by some means, it emits light when the electrons return to their ground states. Scintillation light falls under the general categories of prompt fluorescence, phosphorescence, and delayed fluorescence. Phosphorescence is generally an undesirable characteristic of scintillators, as is delayed fluorescence. To be effective, a scintillator must produce the majority of its light output as prompt fluorescence.

Scintillators fall under the broad categories of inorganic and organic types. Inorganic scintillators generally enjoy higher light output per unit energy deposited, are linear in output down to a lower energy, and are generally composed of high-Z material. These properties make inorganic scintillators useful for gamma spectroscopy. Organic scintillators generally have a lower light output per unit energy deposited than inorganic types, enjoy less linearity in output at lower energies, and are composed of low-Z material. This makes them more suitable for neutron and charged particle applications. Of the two types, organics tend to have faster decay times than inorganics.

In addition to their differences in composition and output properties, organics and inorganics differ in the mechanism by which they produce light. The inorganic scintillation process involves the crystal lattice of the scintillator material. Briefly, the atomic electrons in inorganic scintillators may be excited from the valence band to the conduction band by a charged particle. When the electron falls back to the valence

band, light is emitted. Inorganic scintillators usually employ activators, elements or compounds that exist at energy states between the valence and conduction bands of the scintillator. The excited electron falls into this activator energy band and causes it to become excited, and then decay. The activator decay actually determines the spectral output and decay time of the scintillator. A typical example is NaI (Tl), where the NaI is the bulk of the scintillator material, and the thallium is the activator. Without the thallium activator, NaI is a very weak scintillator.

Organic scintillators emit light by a different mechanism. Instead of individual electrons decaying from excited states in a crystal, the organic molecule as a whole is involved. As charged particles pass by an organic molecule, the electronic structure of the molecule is altered to an excited state. When the excited molecule returns to the ground state, some of the energy lost may be emitted as light. Energy may also be lost through vibrational means, as heat. The decay time is usually on the order of nanoseconds. Organic scintillators may have additional compounds added to them that act as waveshifters: the original scintillation photons are reabsorbed by the waveshifter and re-emitted at longer wavelengths. This provides a mechanism for matching the spectral output of the scintillator to the photosensitive device used to detect the scintillation light. It is possible to have more than one waveshifter in a single scintillator. Organic scintillators can be solids, liquids, or gases. Since the scintillation process occurs at a molecular level, it is independent of physical state.

The light output from an organic scintillator can be described by the expression

$$I = I_0(e^{-t/\tau} - e^{-t/\tau_1}) \quad [4.1]$$

where  $\tau$  is the decay time constant and  $\tau_1$  is the excitation time constant (Knoll 2000). As indicated earlier, typical values of  $\tau$  are measured in nanoseconds for organic scintillators.

#### **4.1.2 Scintillator properties**

The first documented use of plastic as a scintillator dates to 1950 (Schorr and Torney). Since then a wide variety of plastics have become available for radiation detection applications. The scintillator used in this research is BC-430 plastic, purchased from Saint-Gobain (Saint-Gobain Crystals and Detectors, Newbury, OH). BC-430 is designated as a “red” scintillator, though the plastic has a distinct orange color, and the emission spectrum is peaked in the orange-yellow region around 580 nm (Fig.4.1).

BC-430 is a double waveshifting scintillator: the original photons from the ionizing radiation interaction are absorbed by one shifter and emitted at a higher wavelength, which are in turn absorbed by a second shifter and emitted at the final, still higher, wavelength. This particular scintillator plastic was chosen because its emission spectrum closely matches the spectral sensitivity of the photodetector. Full specifications for BC-430 are summarized in Table 4.1.

To achieve the goal of measuring beta dose and beta spectra, several scintillator geometries were designed and constructed. Each scintillator is a cylinder 15 mm in diameter and 13 mm long. Dimensions were chosen to correspond to the photodetector’s diameter and to provide sufficient thickness to fully stop betas with a maximum energy of 2.5 MeV.

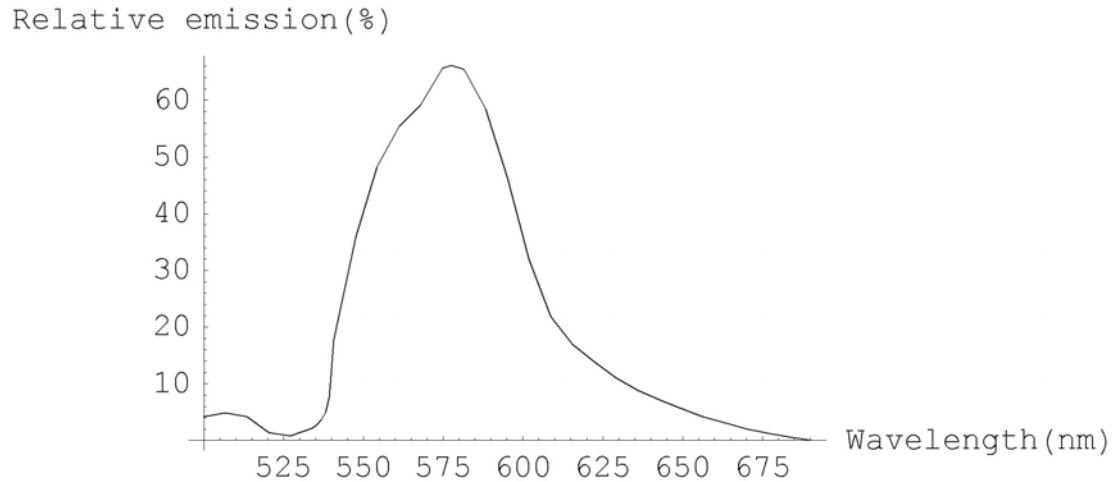


Fig. 4.1: The emission spectrum for BC-430 plastic.

Table 4.1. Properties of BC-430 plastic scintillator.

Property	Value <sup>a</sup>
Light output (%Anthracene)	45
Rise time (ns)	3.2
Decay time (ns)	16.8
Wavelength of maximum emission (nm)	580
Base	Polyvinyltoluene
Density (g/cc)	1.032
Refractive index	1.58

Two scintillators were designed for beta dosimetry (Fig. 4.2). The first consists of a layer of plastic scintillator 1 mm thick, followed by 12 mm of transparent, inert acrylic plastic (BC-802; see Table 4.2). This configuration is designed to measure surface dose. The second has 1 mm of inert plastic followed by 2 mm of scintillator

<sup>a</sup> Values from the Saint Gobain datasheet for BC-430.

plastic, and a third layer 10 mm thick, inert like the first layer. This second configuration records dose at depth, hereon referred to as “shallow” dose.

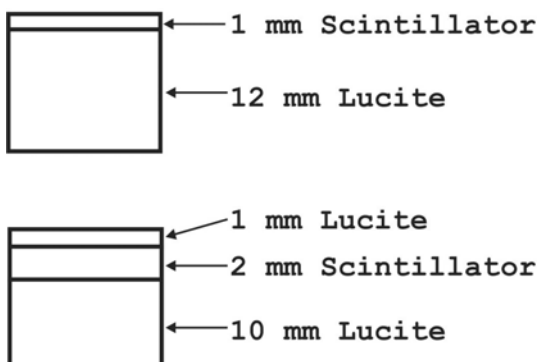


Figure 4.2: Scintillator geometry for beta dose measurement.

Table 4.2. Properties of BC-802

Property	Value <sup>b</sup>
Density (g cm <sup>-3</sup> )	1.19
Refractive index	1.49
Transmission range (nm)	>80% at >400

The surface and shallow configurations do not have precise anatomic equivalents, but in general the following is true: the surface case, 1 mm deep, corresponds to the epidermal skin layer and some of the dermal skin layer. The shallow case, 1 mm deep and 2 mm thick, corresponds to the rest of the dermal layer and some deeper connective tissue. The main concern was not to model anatomic features exactly, since the depth of the epidermis and dermis varies depending on location, but to prove the concept that doses at different depths can be measured with these scintillator configurations.

<sup>b</sup> Values from the Saint Gobain datasheet for BC-802.

rations. Since the scintillation material's properties (density and stopping power) are nearly that of water, and thus of tissue, it was assumed that 1 mm of scintillator is the equivalent of 1 mm of tissue. Monte Carlo modeling was done to prove this assumption.

One scintillator was designed for beta spectroscopy and for calibration of the multichannel analyzer, and consists entirely of scintillation plastic. Each cylinder is covered on all sides, except the side facing the photodetector, with a diffusely reflective, titanium dioxide based paint.

The amount of light collected from the scintillator volumes is the primary quantity that determines the size of the signal at the end of the signal processing chain. There has been some work regarding the efficiency of light collection from scintillators of various shapes (Baronov and others 1996; Bea and others 1994). Using the methods of Baronov, it was possible to calculate a rough value of the light collection efficiency (defined as the percentage of scintillation light made available to the photodiode) for the spectroscopy scintillator. The average number of reflection cycles is given by

$$\bar{k} = 1/(\beta\bar{l} + \varepsilon + \omega - \varepsilon\omega) \quad [4.2]$$

where  $\beta$  is the inverse of the light attenuation length,  $\bar{l}$  is four times the scintillator volume divided by the scintillator surface area,  $\varepsilon$  is the photodiode surface area divided by the scintillator surface area, and  $\omega$  is one minus the reflectance,  $r$ . Values for these variables are listed in Table 4.3. The expression for  $\bar{k}$  is insensitive over a wide range of beta values, so the number used is that given by Baranov. On the other hand,

$\bar{k}$  is very sensitive to the reflectance coefficient. The value chosen is from the literature, where the reflective properties of titanium dioxide were studied (Vargas and Niklasson 1997).

Table 4.3. Parameters used to calculate light collection efficiency from the scintillator.

Parameter	Value
$\beta$ (cm <sup>-1</sup> )	0.002
$\bar{l}$ (cm)	0.951
$\varepsilon$	0.183
$\omega$	0.5

Once  $\bar{k}$  is known, the collection efficiency is given by  $(f_{\bar{k}})^{\bar{k}}$ , where  $f_{\bar{k}}$  is given by  $f_{\bar{k}} = re^{-\bar{l}\beta}$  [4.3]. Carrying through the calculation gives a value of 37% for the collection efficiency, a result in line with similar calculations found in the literature that predict a collection efficiency of between 40 and 50% (Falk and Sparrman 1970). There is a high degree of uncertainty in this value due to the sensitivity of the result to changes in  $r$ . However, it does indicate that since BC-430 produces only about 7000 photons of light per MeV of energy deposited, the total number of photons available at the photodiode surface is not large. It also indicates that at lower energies, where the number of photons becomes quite small, there is likely to be a high degree of uncertainty in the accuracy of the recorded results, assuming they can be recorded at all.



## ***4.2 Photodiodes and avalanche photodiodes***

### **4.2.1 Diode structure**

The use of photomultiplier tubes to detect scintillation light is widespread in radiation detection. An alternative to the standard photomultiplier has been developed: the large-area avalanche photodiode, or LAAPD. The LAAPD under consideration is a semiconductor diode at its heart. A diode consists essentially of two semiconductor materials joined together: a p-type (doped with acceptor atoms, meaning having a deficiency of valence electrons) and an n-type (doped with donor atoms, meaning having excess valence electrons). The point at which they meet is called the p-n junction. At the p-n junction, mobile electrons from the n side are attracted to the p side, and holes from the p side are attracted to the n side. This leaves positively charged, static ions in the n side and negatively charged, static ions in the p side. The region around the junction is therefore depleted of mobile charge carriers, and is referred to as the depletion region. An electric field exists in the depletion region and points from the n side toward the p side. Depending on the application, a bias may be applied to the diode either in the forward (positive bias to the p side) or reverse (positive bias to the n side) direction. If a wider depletion region is needed, for example in order to increase the area of the photosensitive part of a photodiode, a piece of intrinsic (undoped) semiconductor material is placed between the n and p-types. This also serves to lower the junction capacitance, thereby increasing the response time of the diode (Saleh 1991). This construction is called a p-i-n diode.

### **4.2.2 Photodiodes**

Many semiconductor materials are sensitive to light, in the sense that an incident photon, subject to wavelength restrictions, may be absorbed in the semiconductor and elevate an electron from the valence band to the conduction band. This is an example of the photoeffect, photoconductivity, to be precise, since the elevated electron remains in the semiconductor (Saleh 1991). In the case of a photodiode, the p-n junction absorbs light and produces conduction electrons in the depletion region. These electrons are transported by the internal electric field in the depletion region and become available as an electric current. P-n photodiodes are generally reverse biased, so the electrons move to the n side of the diode. A strong reverse bias improves the operating characteristics of a photodiode: it widens the depletion region, making available a larger photosensitive area; it decreases the junction capacitance, thereby increasing response time; it reduces charge carrier transit time in the depletion region (Saleh 1991).

### **4.2.3 Avalanche photodiodes**

Neither p-n nor p-i-n photodiodes exhibit any signal gain. If the reverse bias is strong enough, however, a condition where impact ionization occurs can be achieved. Impact ionization refers to an electron, elevated to the valence layer by the internal photoeffect, being accelerated sufficiently by the applied electric field so as to cause other valence electrons to be elevated to the conduction layer by collision processes.

These secondary electrons are in turn accelerated and will create impact electrons, and so on. The process is termed an avalanche. The avalanche characteristics are determined by the impact ionization coefficient  $\alpha$ , in units of  $\text{cm}^{-1}$ , which represents the rate of ionization. The inverse of  $\alpha$  is the average distance between ionizations. Alpha increases with applied electric field strength and decreases with temperature. There are separate  $\alpha$  values for electrons and holes; generally, either one or the other is dominant in the avalanche process, in order to limit noise. If the excess noise factor is given by (Sze 1981)

$$F = M \left( \frac{\alpha_h}{\alpha_e} \right) + \left( 2 - \frac{1}{M} \right) \left( 1 - \frac{\alpha_h}{\alpha_e} \right) \quad [4.4]$$

where  $M$  is the avalanche multiplication factor, then it is advisable to make the ratio of  $\alpha_h$  to  $\alpha_e$  as small as possible. Response time for avalanche photodiodes is slower than for p-n and p-i-n photodiodes, due to the time required for the avalanche process to take place.

#### 4.2.4 Large-area avalanche photodiodes

An avalanche photodiode is considered large if the active surface diameter is  $\geq 5 \text{ mm}$  (Moszynski 2002). The general term for this type of APD is LAAPD, for large-area avalanche photodiode. There are several common avalanche photodiode designs, such as reach-through and beveled-edge types. The APD used in this research is of the beveled-edge type (Fig.4.3), which allows the applied electric field to maintain a high degree of uniformity across a plane parallel to and in the avalanche region. The elec-

tric field profile is seen in Fig. 4.4. This is crucial to making the device practical, since non-uniformities in gain would make the output of doubtful use.

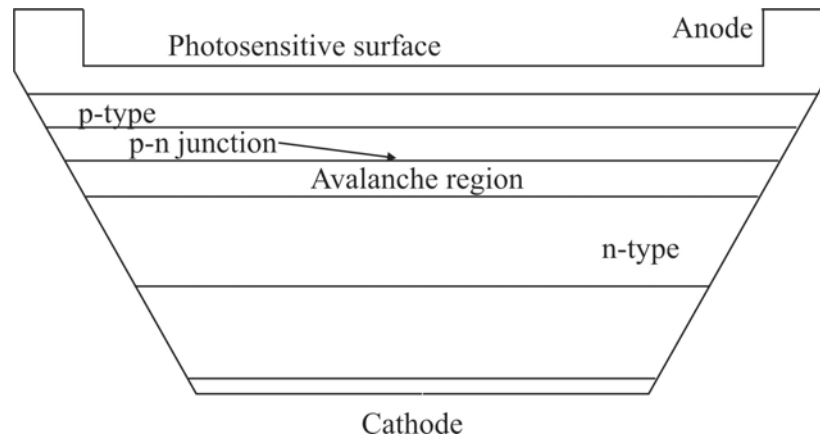


Fig. 4.3: Beveled-edge LAAPD.

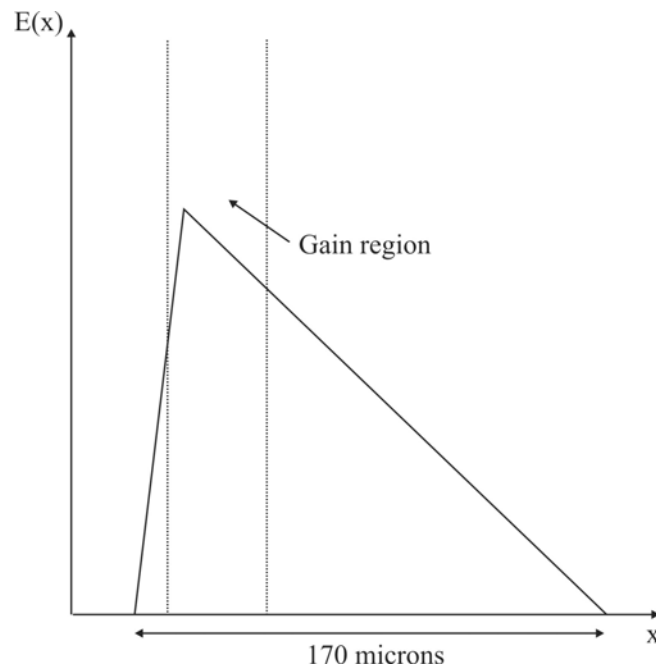


Fig. 4.4: Electric field profile across the LAAPD.

An LAAPD may be enhanced to increase its sensitivity to certain wavelengths of incident light. This is often necessary because the emitted light from different scintillators varies widely in wavelength. Most photodiodes are maximally sensitive at larger wavelengths, in the red to infrared zones. To be efficient at smaller wavelengths, where most scintillators operate, the maximal sensitivity must be shifted down. The scintillator in this research emits light at a peak wavelength of about 580 nm. To get a better match between the LAAPD sensitivity and the scintillator output, a blue-enhanced version of the LAAPD was chosen. “Blue-enhanced” is somewhat of a misnomer, since the peak sensitivity is not really in the blue spectral region; it merely refers to a shifting of the sensitivity towards lower wavelengths.

With the advantage of signal gain comes the disadvantage of increased noise in avalanche photodiodes. Noise refers not only to extraneous undesirable signals, but also to fluctuations in the number of charge carriers produced at various stages during signal generation. A given number of photons incident on the detector will produce a lesser quantity of photoelectrons that will fluctuate around some average value; the average photoelectron value divided by the number of incident photons is called the quantum efficiency, or QE. All photodiodes, whether avalanche types or not, suffer from the uncertainty associated with the QE of the device. Gain noise refers to the uncertainty in the number of avalanche electrons produced in an APD. Under the same initial conditions, the number of avalanche electrons, and hence the signal magnitude, will vary around an average value. There is also a dark-current component to the noise caused primarily by thermal effects; dark-current is always present in some capacity,

whether incident light is present or not. Background noise refers to unwanted incident light; this component can be eliminated with careful experimental procedures (Saleh 1991).

Dark current is divided into two components. The first results from electron-hole pairs generated in the non-avalanching n-region (un-amplified bulk dark current) and surface leakage current. This component,  $I_{ds}$ , does not undergo any amplification in the APD, which lessens its significance. The second component,  $I_{db}$ , consists of bulk dark current from electron-hole pairs generated in the p-region of the APD; this component does undergo avalanche multiplication (Advanced Photonix 1991). Overall, the total output from an avalanche photodiode can be represented as

$$I = I_{ds} + M_{db}I_{db} + M_0I_0 \quad [4.5]$$

where  $M_{db}$  is the avalanche multiplier for the dark current component that undergoes avalanche multiplication, and  $M_0$  is the avalanche multiplier for the signal current  $I_0$ . It is a valid approximation that  $M_0$  and  $M_{db}$  are equivalent (Advanced Photonix 1991). The key point is that avalanche gain is a double-edged sword: the higher the gain, the less significant  $I_{ds}$  becomes, but the more significant  $I_{db}$  becomes. Past a certain bias voltage (gain), noise due to dark current becomes excessive. From the literature, a gain of about 100 corresponded to the optimal value for minimizing noise (Advanced Photonix 1991). During the course of this research the gain was maintained at or below 100. The amplifier shaping time constant also affects the total noise. Shorter time constants decrease the noise, though too short a time constant will prevent full signal col-

lection (Moszynski 2002). Of the three values available on the amplifier used in this research, a time constant of 0.1 microseconds produced the best signal.

### ***4.3 Large-area avalanche photodiode module***

Recently, a LAAPD has been incorporated into a module that includes a pre-amplifier and a gain adjustment control. The LAAPD module not only takes the place of the photomultiplier tube/preamplifier combination in detecting scintillation light, but also acts as a detector in its own right. The focus of this research is on using the LAAPD module to detect and measure beta spectra via a plastic scintillator coupled to the LAAPD, in the absence of any significant gamma field. With suitable signal processing it is possible to record energies as low as about 100 keV. This ability allows a wide variety of beta emitters to be studied.

The module is a product of Advanced Photonix, Inc., Camarillo, CA, USA (Fig. 4.5). The LAAPD in this module is of the beveled-edge type. It has an avalanche zone thickness of about 15  $\mu\text{m}$ , and an overall thickness of about 170  $\mu\text{m}$  (Moszynski 2002). It has a diameter of 16mm, is windowless, and is blue-enhanced to shift its peak spectral sensitivity to lower wavelengths. The properties of the avalanche photodiode are summarized in Table 4.4. Advantages of a LAAPD over a photomultiplier tube include compact size, ruggedness, imperviousness to magnetic fields, higher quantum efficiency, and for this module in particular freedom from an external high voltage source. Disadvantages include smaller size, smaller gain, and noise effects due to dark current.



Fig. 4.5: The LAAPD module. Top: View of the LAAPD. Bottom: View with scintillator attached. The entire module is about 6 inches long by 2 inches wide and deep.



Table 4.4. Operating parameters of the LAAPD module.

Parameter	Value
Diameter (mm)	16
Dark current (nA)	280
Quantum efficiency at 550 nm and gain of 200 (%)	95
Spectral enhancement	Blue
NEP (pW/ $\sqrt{\text{Hz}}$ )	0.43
Frequency range (Mhz)	0.002-10
Output impedance ( $\Omega$ )	40
Output stability (%/ $^{\circ}\text{C}$ )	1.2
Operating voltage (V)	12
Current at $\pm 12$ V (mA)	20-150

The module requires  $\pm 12$  volts, supplied through a LEMO connector from the NIM Bin. Output is through a BNC connector from the built-in pre-amplifier. The module has a potentiometer adjustment screw that allows the high voltage generated by the module to be varied, according to the desired gain. There is also a temperature sensitive high voltage compensator circuit built into the module; as the photodiode temperature increases, the gain decreases, and the compensator circuit raises the high voltage at a rate necessary to compensate. The entire module is about 6 inches long by 2 inches wide.

At any particular temperature there is a gain versus high voltage curve that allows the gain to be known at any particular setting of the high voltage (Fig. 4.6).

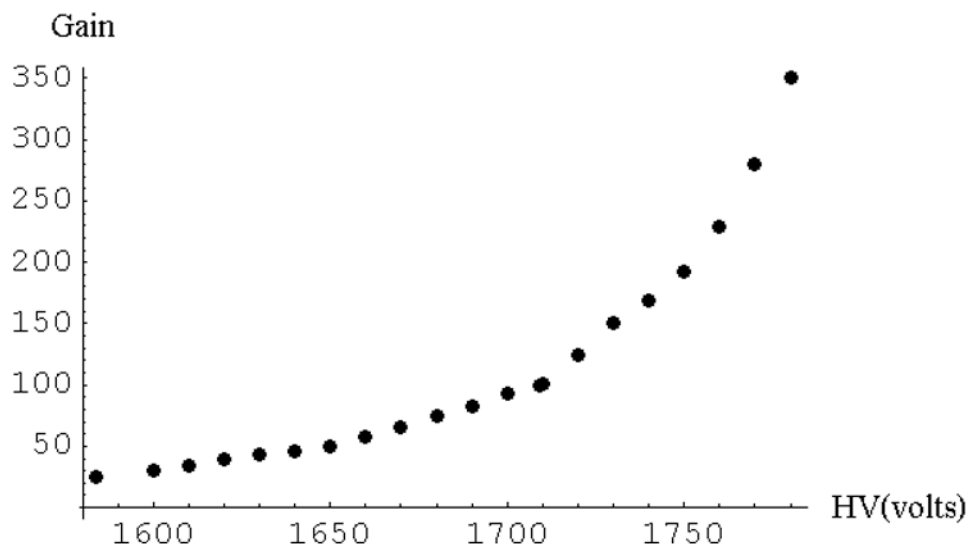


Fig. 4.6: High voltage versus gain curve for the LAAPD module.

The curve supplied by the manufacturer is specified at 17.2 degrees Celsius. As the lab temperature was consistently higher, and varied throughout the day, the manufacturer's curve acted only as a general guide to determining the gain. In order to get a quantitative grasp on the relationship between high voltage and temperature, both were measured every minute over an 8-hour period. A Fluke Hydra portable data acquisition system model 2635A (Fluke Corporation, Everett, WA), controlled by a laptop PC, recorded temperature information from a lead attached to the brass LAAPD housing ring. An opaque rubber cap covered the face of the LAAPD. The resulting high voltage and temperature versus time curve is seen in Fig. 4.7.

Overall, the HV compensation circuit raised the voltage at a rate of about 4 volts per degree Celsius. Based on these results, the module was allowed at least ninety minutes of warm-up time before taking spectral data, thus avoiding the steep

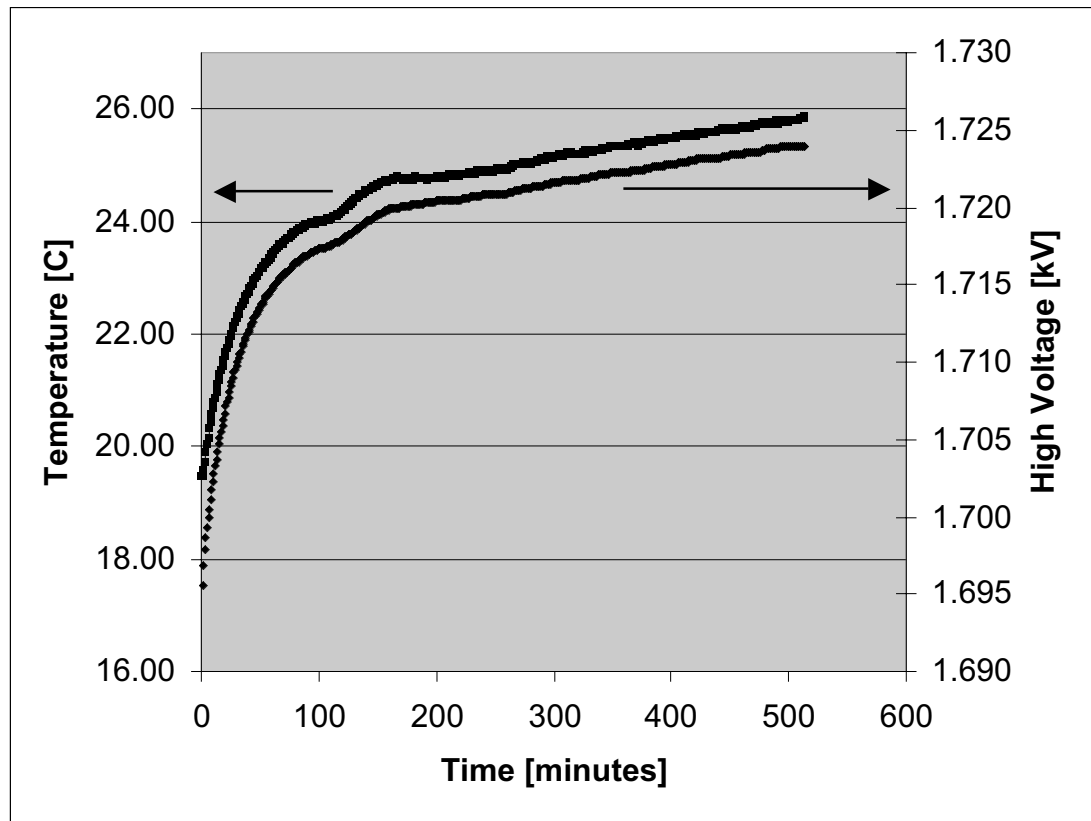


Fig. 4.7: High voltage (lower curve) and temperature v. time. The change in temperature is clearly tracked by the change in high voltage, resulting in constant gain maintained by electronic temperature compensation.

portion of the curve. In general, the temperature in the lab increased several degrees Celsius throughout the course of the day, more during the summer than the winter; however, the high voltage compensation circuit kept the gain steady and recalibration was not necessary. High voltage was monitored with a digital voltmeter.

The module's output is a positive, unipolar pulse with a rise time of about 27 ns and a fall time of approximately 40 ns. The FWHM is about 50 ns, and amplitude varies depending on the gain setting and beta energy (Fig. 4.8). Pulses tended to be no higher than 20 mV at our settings. This pulse shape posed some challenges for the in-

strumentation at our disposal, an issue covered in depth in the pulse processing section.

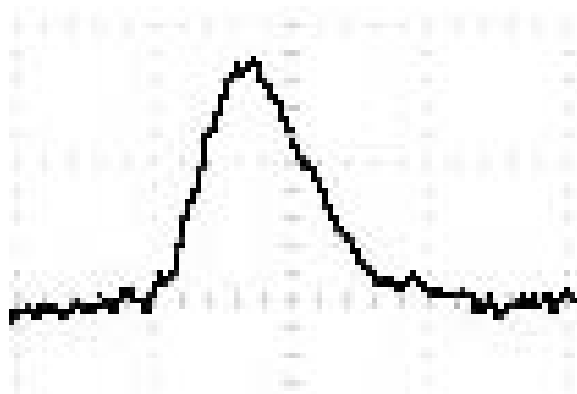


Fig. 4.8: Pulse shape from the LAAPD module. Pulse is about 18 mV amplitude and 50 ns FWHM.

## ***4.4 Beta sources and auxiliary equipment***

### **4.4.1 Sources**

$^{90}\text{Sr}/^{90}\text{Y}$ ,  $^{36}\text{Cl}$ ,  $^{99}\text{Tc}$ ,  $^{14}\text{C}$ , and  $^{210}\text{Bi}$  beta sources were used for this experiment, as well as  $^{137}\text{Cs}$  and  $^{133}\text{Ba}$  conversion electron sources, and  $^{60}\text{Co}$  and  $^{137}\text{Cs}$  gamma check sources. With the exception of  $^{210}\text{Bi}$ , the beta sources are spot sources of less than 5 mm diameter; they are sandwiched between  $0.9 \text{ mg cm}^{-2}$  thick aluminized mylar layers 24 mm in diameter, an encapsulation thin enough to minimize self-absorption while preventing contamination. The  $^{210}\text{Bi}$  has an aluminum backing, which causes backscatter to become a factor. The CE sources are unencapsulated and required careful handling. The gamma check sources were confined in plastic disks. The beta

source specifications are listed in Table 4.5. The activity listed for  $^{90}\text{Sr}/^{90}\text{Y}$  is for  $^{90}\text{Sr}$  alone; actual activity is twice that due to secular equilibrium of  $^{90}\text{Sr}$  and  $^{90}\text{Y}$ .

Table 4.5. Beta source properties.

Nuclide	Activity (dpm)	Maximum Energy (keV)
C-14	244200	156
Tc-99	70992	292
Cl-36	41735	709
Sr/Y-90	29927	546/2281
Bi-210	33207	1160

#### 4.4.2 Source holder and spacers

In order to ensure measurement repeatability, minimize backscatter from behind the source, and enable accurate Monte Carlo simulation, a special source holder was built (Fig.4.9).

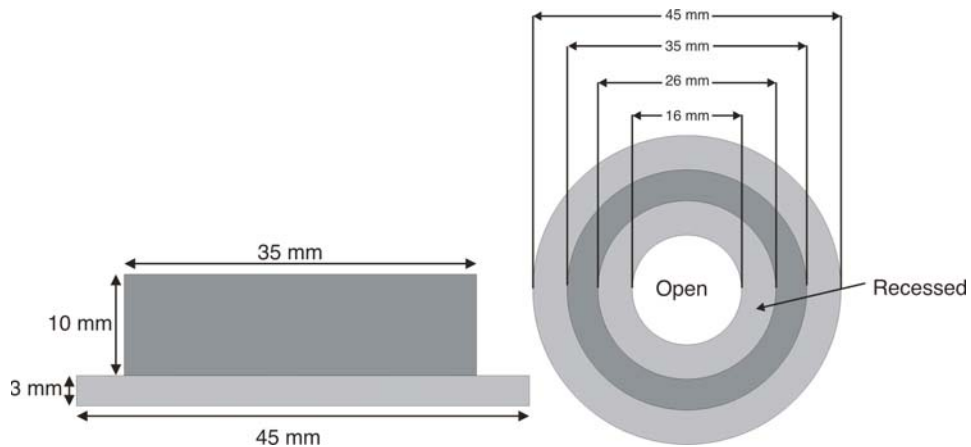


Fig. 4.9: Beta source holder (aluminum). Left: side view. Right: top view.

In addition, four cylindrical, steel spacers were constructed that fit over the source holder and aluminum locking collar attached to the LAAPD module, allowing the distance from the source to the detector face to be known to within 1 millimeter. These spacers allow measurements to be taken at source-detector distances of 5, 10, 20, and 30 mm. They also fulfill the role of keeping ambient light from striking the detector, a vital consideration since the reflective paint on the scintillator is not opaque to outside light. The overall setup is illustrated in Fig. 4.10. Low-activity lead bricks surrounded the detector, in order to minimize background radiation.

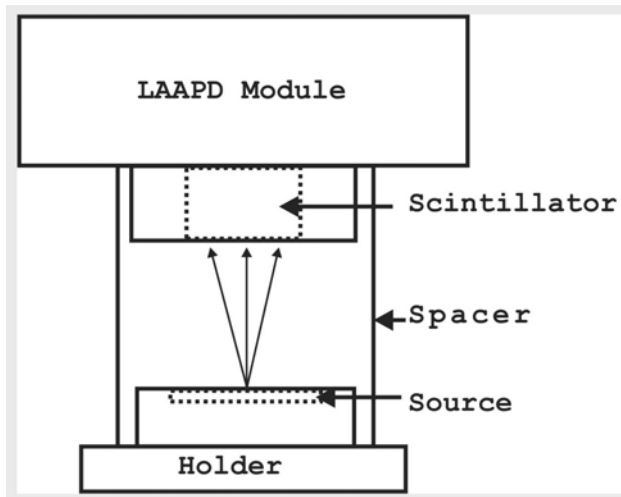


Fig. 4.10: Measurement geometry.

#### 4.4.3 Scintillator-LAAPD coupling

The scintillator couples directly onto the LAAPD face. Optical coupling compound is not used, since the compound would have to be carefully cleaned from the

APD before using the LAAPD as a detector by itself, without the scintillator. The manufacturer warned that removing a compound-coupled scintillator from the LAAPD risked physical damage to the diode. Furthermore, since it was frequently necessary to change from one scintillator to another, the process was made considerably simpler by dispensing with optical coupling compound. Near the completion of data acquisition for this research, coupling compound was used, with no benefit. The faces of the scintillator and LAAPD are smooth and flat, minimizing any air gap that might degrade light collection efficiency. To keep the scintillator in firm contact with the photodiode face, it was enclosed in a lucite ring that matched the outer diameter of the photodiode housing, then further enclosed in an aluminum locking collar that fit around the lucite-scintillator combination and over the photodiode housing (Fig. 4.11).

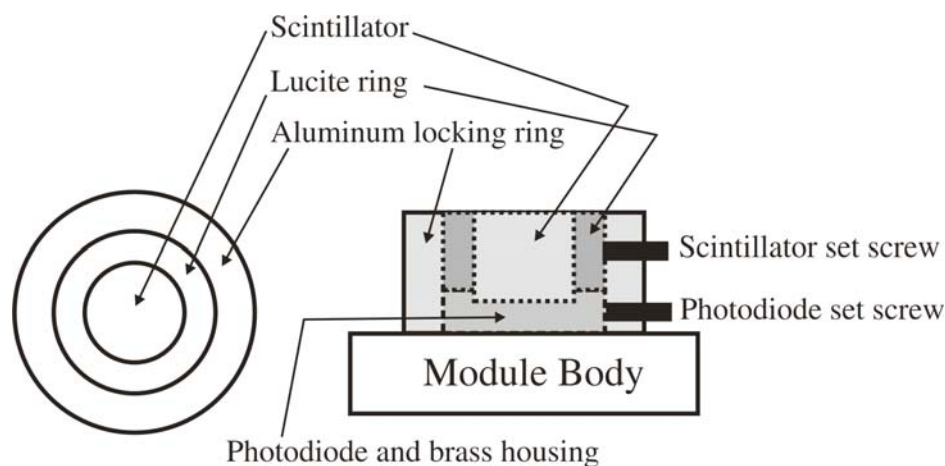


Fig. 4.11: Diagram of the scintillator assembly. The scintillator, 13 mm thick, is flush with the LAAPD face. The Lucite ring and aluminum locking ring were custom fabricated at OSU.

### ***4.5 Pulse Processing***

The NIM bin and other equipment used for pulse processing underwent a gradual evolution before a final configuration was chosen. Referring back to Fig. 4.8, the output from the LAAPD module is small and fast. Available NIM bin equipment was inadequate for the sort of signal coming from the LAAPD module. The amplifier, a double delay-line type, couldn't handle the fast, small pulse properly. Even at maximum gain, less than half the channels on the MCA displayed counts for the highest energy betas, 2,281 keV from  $^{90}\text{Y}$ . This spectral compression was undesirable since it limited the ability to see details in the spectra, especially for low-energy emitters. From a dosimetry standpoint it was also undesirable, since the energy bin width became too large, thus limiting the dose calculation resolution.

The first effort to remedy this problem involved boosting the module's output by feeding it to a ZPUL-50P signal amplifier (Mini-Circuits, Brooklyn, NY) before passing it to the NIM delay-line amplifier. The signal was boosted by a factor of about 20, but it was still too fast. Also, the Mini-Circuits amplifier was subject to transient bursts of noise, possibly temperature related, that periodically would wipe out data being collected. This solution was therefore abandoned as impractical.

Besides the amplitude and speed of the signal, the narrow width of the signal posed a problem for the MCA. The MCA input requires a signal of at least 0.5 microseconds in width in order to adequately process the signal. Since the LAAPD module output was only on the order of 40 nanoseconds FWHM, accurate recording of pulses



was further impeded. The solution was to place a NIM stretcher module between the delay-line amplifier and the MCA input. A stretcher simply takes a narrow signal and widens it at its maximum amplitude to the necessary width. However, another difficulty now arose. The stretcher required input pulses of at least 100 mV amplitude, clearly above the 20 mV maximum from the module. The solution to this problem was found by passing the signal from the module through a charge sensitive preamplifier. Not only did this allow the use of the stretcher module, but it permitted the delay-line amplifier gain, heretofore set at maximum, to be decreased to about 12, a setting chosen for reasons made clear in the section on data processing.

Due to the presence of low-energy noise from the LAAPD module, the discriminator on the stretcher was set high enough to screen most of it out before it reached the MCA. However, the discriminator itself had some difficulty producing a sharp cutoff energy; the spectrum seen on the MCA invariably included excess noise events at the cutoff energy. To eliminate this noise as much as possible, the signal from the stretcher was split between a single channel analyzer (SCA) and a delay amplifier. By using the oscilloscope to set the timing between the two signals properly, it was now possible to use the gate function on the MCA to further keep low-energy noise signals out of the spectrum. The signal from the delay amplifier went to the energy input of the MCA; the timing signal from the SCA went to the gate input of the MCA. All the spectra seen in the Results section were recorded using this setup. The overall instrument chain is illustrated in Fig. 4.12. The evolution of the signal shape, from LAAPD module to delay amplifier output, is seen in Figs. 4.13 through 4.17

(pulses are representative; they did not originate from the same event). Table 4.6 lists the NIM bin modules used in the final configuration.

The multichannel analyzer is an Ortec Trump PCI, controlled by Ortec's Maestro software. The Trump PCI is a full-sized card that takes up one PCI expansion slot, and runs on a Windows NT platform. It is capable of 2k (2048) channels.

#### ***4.6 Energy calibration***

Before any spectroscopy or dosimetry measurements can be done, the detector system must be calibrated. The traditional way to calibrate a scintillator is to use a gamma emitter that will produce a photopeak of suitable sharpness on the MCA. However, due to the small size of this scintillator, and the physical fact that plastic provides a very small cross-section for photoelectric absorption, this approach could not be taken, since no photopeak was produced. Therefore, it was determined that the next best way was to use conversion electrons over a range of energies. Two conversion electron sources,  $^{137}\text{Cs}$  and  $^{133}\text{Ba}$ , were purchased for this task. Cesium-137 produces conversion electrons at two major energies, 656 and 624 keV, whereas  $^{133}\text{Ba}$  produces conversion electrons at many energies from about 350 keV down. It was hoped that these energies would permit calibration of the MCA. However, this turned out not to be the case.

Since conversion electrons occur as an alternative to gamma emission, there was significant gamma emission from  $^{137}\text{Cs}$  and  $^{133}\text{Ba}$ . Though the photoelectric cross-section was small, the Compton cross-section was high enough to cause most of the

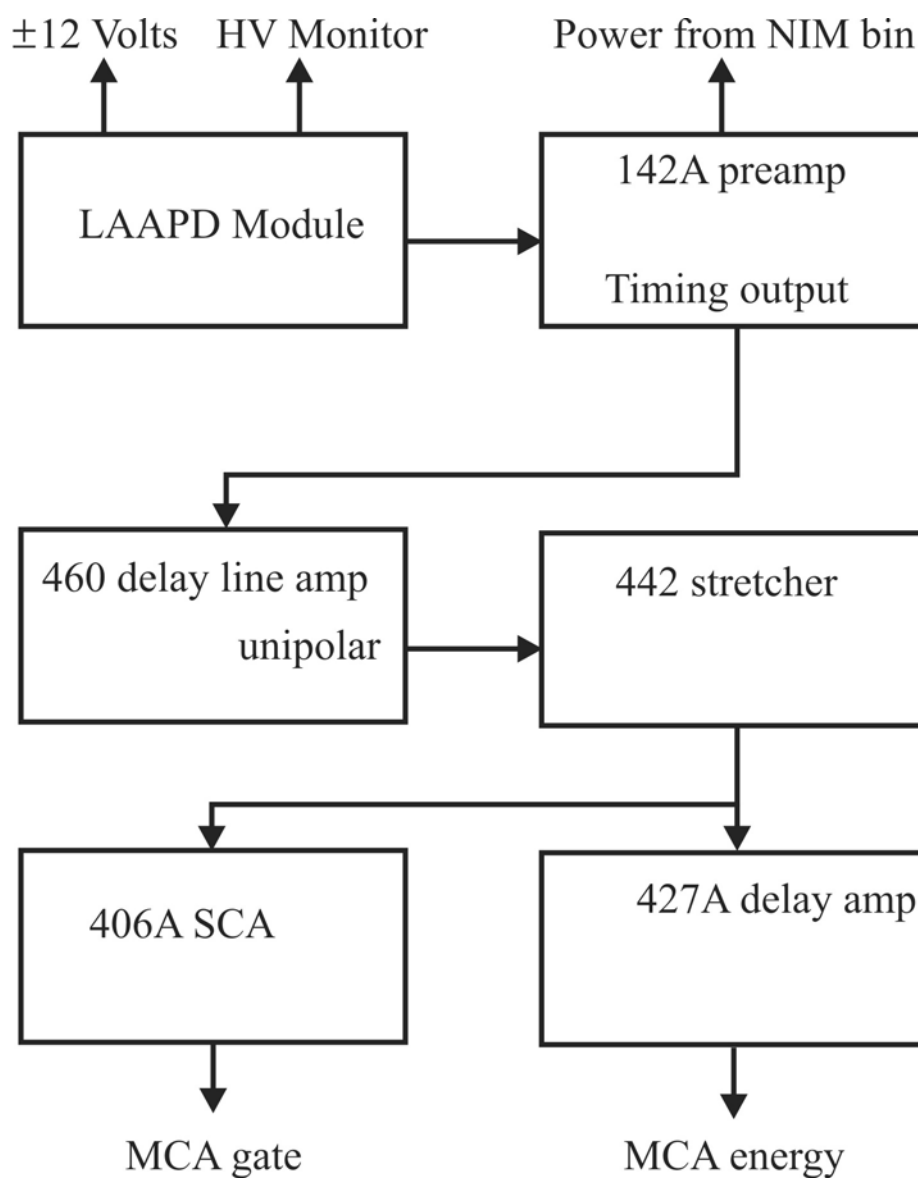


Fig. 4.12: Block diagram of pulse processing instrumentation.

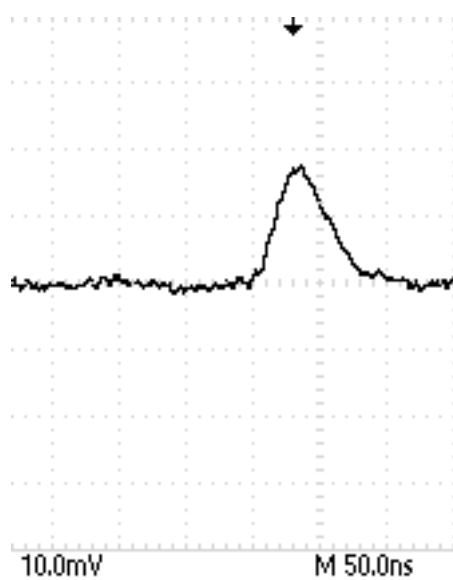


Fig. 4.13: LAAPD module output; generally 5 to 15 mV in height, 27 ns rise and 40 ns fall time, 50 ns FWHM.

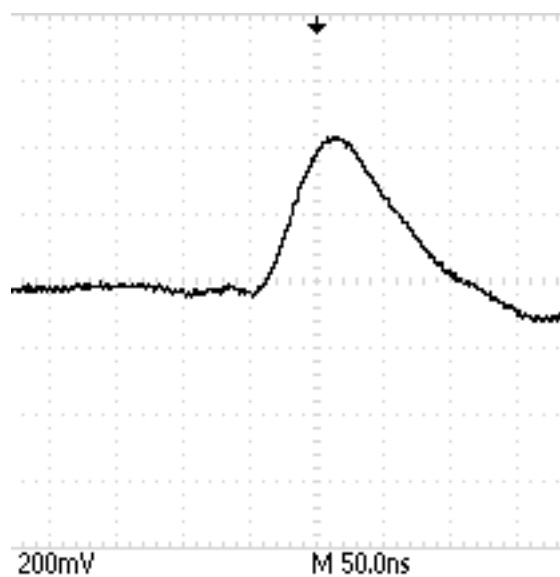


Fig. 4.14: 142A preamp output.

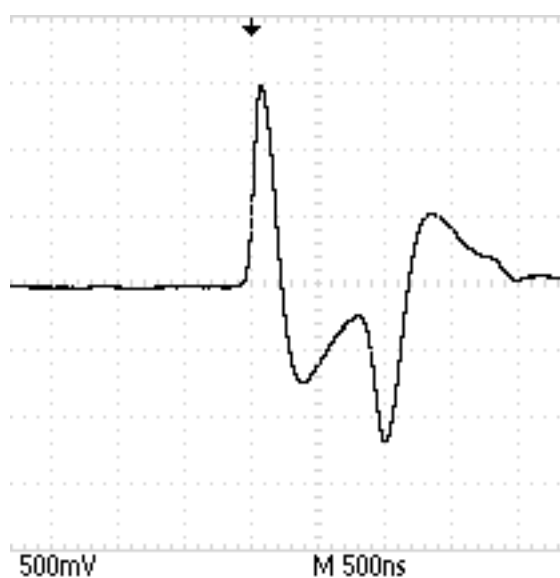


Fig. 4.15: Signal from the Ortec 460 delay line amplifier output with 0.1 microsecond integration constant and gain at about 12; about 1.5 V height, 200 ns FWHM.



Fig. 4.16: Output from the stretcher, Ortec 442; 1.5 microsecond width and 2.5 V amplitude.

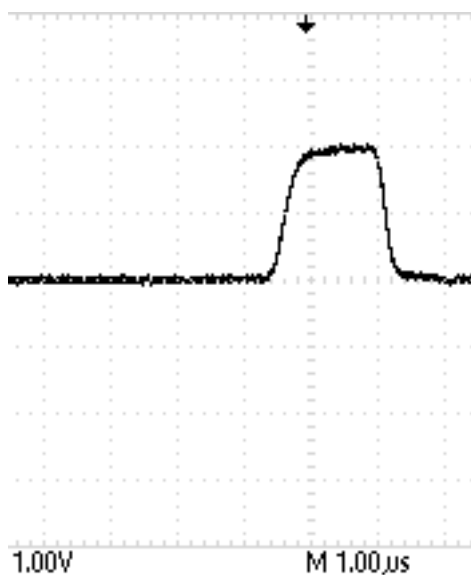


Fig. 4.17: Output from the Ortec 427A delay amplifier, 2 V amplitude and 1.5 micro-seconds width. The 427A provides the necessary delay for gating the signal.

Table 4.6. NIM bin modules and settings.

Module	Settings
Ortec 142A charge sensitive preamp	Timing output
Ortec 460 delay line amplifier	0.1 $\mu$ s time constant; gain $\approx$ 12; positive pulse; unipolar output
Ortec 442 linear gate and stretcher	DC couple; normal
Ortec 406A single channel analyzer	Normal
Ortec 427A delay amplifier	0.25 $\mu$ s delay

conversion electron peaks to become obscured. Efforts were made, unsuccessfully, to reveal the CE peaks by subtracting a Compton background count from a Compton and CE count. The only CE peak that could be unequivocally identified as such was the 624 keV  $^{137}\text{Cs}$  peak (Fig.4.18). However, it was too broad to be of use, probably be-

cause of the inherently poor energy resolution enjoyed by plastic scintillators. The conclusion was that CE sources are best used to advantage with other sorts of detectors, such as surface barrier types, where gamma interference is minimized.

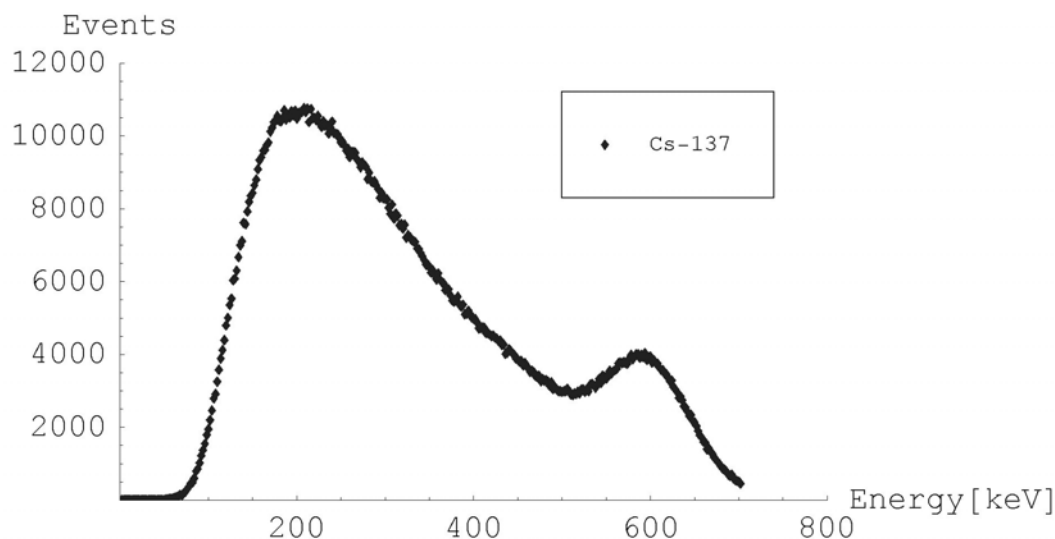


Fig. 4.18: Cs-137 spectrum showing the peak (at about 600 keV) from the 624 keV conversion electrons. The peak is too broad for effective energy calibration.

It was finally decided that the only way to achieve a reasonably accurate calibration was to count with the  $^{90}\text{Sr}/^{90}\text{Y}$  source for an hour, and set the end channel of the spectrum at the endpoint energy, 2,281 keV. Once this was done, it was possible to count other nuclides, such as  $^{36}\text{Cl}$  and  $^{99}\text{Tc}$ , and verify that their spectral endpoints fell at the right energies, keeping in mind the energy losses that might occur due to source encapsulation and air absorption. Though there were uncertainties in calibrating in this manner (deciding exactly in which channel the endpoint energy lies was somewhat

subjective), overall it proved accurate enough for identifying the radionuclides of interest.

Any change of the amplifier or LAAPD gain would require a recalibration. Because the measured results were ultimately to be compared to MCNP models, it was desired that the calibration of the MCA correspond to the energy bin width of the MCNP simulations. The MCNP simulations were all performed with a 2 keV energy bin width, so it was necessary to adjust the gain on the amplifier until a calibration was achieved that resulted in 2 keV per channel on the MCA, assuming no change in the LAAPD gain. In practice it was impossible to achieve exactly 2 keV per channel, however, the error over the energy range of interest (up to about 2300 keV), amounted to less than 2 keV.

In order to verify the calibration's stability, a series of 16 measurements, each 30 minutes in length, was taken of the  $^{90}\text{Sr}/^{90}\text{Y}$  source. A Maestro batch file was written to automate the process. By examining the channel positions of the distinctive parts of the spectra it was confirmed that the calibration remained steady after the initial warm-up period. As a final verification,  $^{137}\text{Cs}$  and  $^{60}\text{Co}$  check sources were counted until the Compton edges were clear. The Compton edges fell where they were expected, at about 478 keV for  $^{137}\text{Cs}$ , and 1,038 keV for  $^{60}\text{Co}$  (Fig. 4.19).

The solid scintillator cylinder was used for spectroscopy and energy calibration of the detector. Betas of energy up to 2.5 MeV can be measured before the occurrence of a beta penetrating entirely through the scintillator becomes possible. If a beta penetrates the scintillator and enters the LAAPD, it will deposit some or all of its remain-



ing energy in the silicon. Since the loss of energy in silicon results in the creation of far more electron-hole pairs than an equivalent energy loss in the scintillator, an accurate calibration can only be achieved if direct-in-silicon interactions are excluded. If it is desired to measure betas of higher energy, a thicker scintillator will be needed.

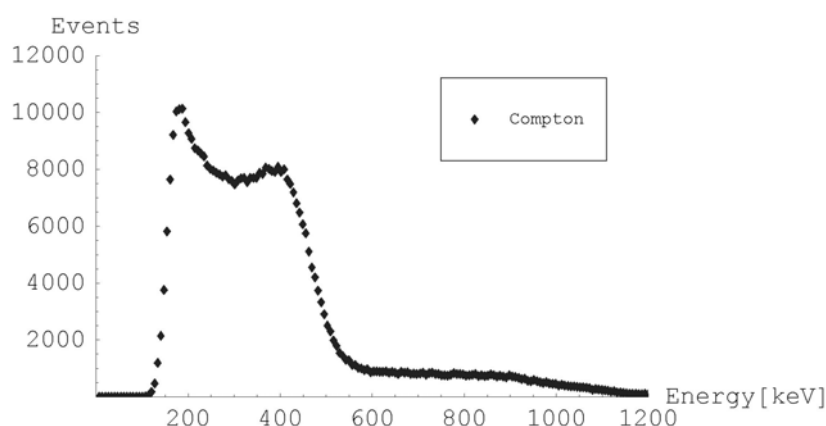


Fig. 4.19: Compton edges from Cs-137 (~478 keV) and Co-60 (~1038 keV). The edges are broad, especially for Co-60, but occur at the expected energies.

## 4.7 Data Processing

Measured spectral data are stored in files with a .chn attribute, called Integer CHN files. The files contain energy and count information, but must be processed by a separate program before they can be inspected or interpreted. The Maestro instruction book provided the CHN file format information, if one wanted to write a C program to read the data. However, it proved easier to download a program called AttenCHN (Allday 2002), which can read an Integer CHN file and place the data in an Excel (Mi-

Microsoft Corporation, Redmond, WA) spreadsheet. The data could then be formatted as needed.

The dose calculations from measured data were calculated in Excel. However, for certain calculations and for creating detailed graphs, Mathematica (Wolfram Research, Inc., Champaign, IL) proved to be a better tool. To import the data into Mathematica, it was necessary to copy it from Excel and paste it into a Microsoft WordPad text file, from which Mathematica could easily access the data. The same mechanism was used to analyze the Monte Carlo generated data, minus the AttenCHN step.

#### ***4.8 Dose calculation methodology***

Dose to tissue is defined as energy  $E$  imparted to a mass  $M$ , divided by  $M$ . As the betas traverse the scintillator, they give up some or all of their energy, which produces a proportional quantity of scintillation light. This light is converted to an electrical signal by a large-area avalanche photodiode and associated electronics, until it is recorded as part of a pulse-height spectrum in a multichannel analyzer. After a spectrum of energy depositions in the scintillator volumes is recorded, multiplying the number of counts at each energy of the spectrum by the spectrum energy, and summing those products, yields the total energy deposited. Knowing the mass of the scintillator volume, dose is calculated by dividing the total energy deposited by the mass. Mathematically,

$$E_{total} = \sum_i N_i \times E_i \quad [4.6]$$

where

$E_{total}$  = energy deposited in the scintillator volume (keV),

$N_i$  = the number of counts at spectrum position  $i$ ;

$E_i$  = the energy at spectrum position  $i$  (keV).

and

$$D = 1.602 \times 10^{-16} * E_{total} * \frac{1}{M} \quad [4.7]$$

where

$D$  = absorbed dose, (Gy);

$M$  = mass, (kg).

These dose calculations involve some simplifications. Since a beta particle loses most of its energy in close proximity to its travel path, it makes little sense to divide the entire mass of the scintillator into the energy deposited by one beta. There must be many betas, uniformly irradiating the scintillator, for the dose value to have meaning. Furthermore, the beta energy cannot be so low that all of the energy is deposited in a thin surface layer of the scintillator volume, as dividing by the entire scintillator mass will severely underestimate the dose. For the surface scintillator, this precludes using low-energy betas such as  $^{14}\text{C}$  or  $^{99}\text{Tc}$ , which have maximum energies of only 156 keV and 292 keV, respectively. The energy corresponding to a CSDA range of 2 mm in BC-430 plastic is about 550 keV; beta emitters with maximum energies much lower than that will not produce accurate results in the surface dose case. By the

same reasoning, only high-energy beta emitters such as  $^{210}\text{Bi}$  and  $^{90}\text{Y}$  will provide useful results for the shallow dose case.

Since scintillator plastic is not actually tissue, it was necessary to establish that it was indeed close enough to tissue equivalency for the purposes of beta dosimetry. This was done by comparing Monte Carlo simulations using plastic scintillator material to those using A-150 tissue equivalent plastic and water. The geometry consisted of an isotropic source 10 mm from a sphere of material 5 mm in diameter. As seen in Table 4.7, dose values in plastic scintillator differ from dose values in A-150 plastic by just under 10% for  $^{36}\text{Cl}$  and  $^{90}\text{Sr}$ , and just over 1% for  $^{90}\text{Y}$ . Dose values are not substantially different compared to water. These results indicate that polyvinyltoluene-based (PVT) scintillator is a reasonable substitute for tissue for use in beta dosimetry.

Table 4.7. Comparison of MCNP beta doses to establish tissue-equivalency of PVT plastic scintillator for beta dosimetry. Values are in  $\mu\text{Gray}$ .

Radionuclide	PVT scintillator	A-150 tissue equivalent plastic	Water
Cl-36	1.18	1.08	1.19
Sr-90	0.854	0.779	0.865
Y-90	2.49	2.46	2.53

Measured doses were compared to Monte Carlo simulations and VARSKIN Mod 2 calculations. VARSKIN Mod 2 (Pacific Northwest National Laboratory, Richland, WA) is a software program designed to model external beta dose to skin. It uses Berger's point kernel data to calculate dose, and can account for clothing or other intervening substances, such as air gaps, that may lie between the source and the target.

Input consists of defining the source geometry and strength, and any intervening material between the source and skin. Output can include volume-averaged dose, a feature used in this work. VARSKIN calculations were performed in order to provide a check both for the measured values and for the MCNP results.

#### ***4.9 Monte Carlo N-Particle modeling***

Developed at Los Alamos National Laboratory, Monte Carlo N-Particle (MCNP) is a computer code that permits the modeling of radiation transport in user-defined structures (Briesmeister 2002). The user specifies the geometry, material data, source spectrum and shape, number of events, and type of data to record, via an input file (Appendix A). Neutrons, electrons, and gammas can be modeled, and their interactions with the materials recorded. In this study, only electrons are modeled. The quantity of interest was the energy deposited by each electron in a specific cell, in this case the detector volume. In MCNP parlance this is a “tally”, specifically a pulse-height tally, designated as an F8-type tally. To get an accurate record of the energy deposited, the energy-bin spacing was specified at 2 keV. This energy bin spacing matched the energy bin spacing of the measured data.

Dosimetry and spectroscopy MCNP simulations corresponding to measured cases were implemented. In order to ensure that the simulations modeled the measurement conditions as closely as possible, all materials that might have an influence on the results were included. At the same time, it was important to exclude any materials that would not have had an effect, yet would have created extraordinary computational

burdens. Electrons, by nature of their continuous interactions with matter, require a great deal of computational effort, if those interactions are to be accurately modeled. This means long computation times, so any savings that can be made are welcome.

The experimental setup involved the mylar-encapsulated source resting on the hollow source holder. Since this device minimized backscatter, the source holder was not modeled. Instead, the volume behind the source was modeled as a void with importance of zero, meaning once an electron reached this volume, it was no longer followed. To ensure that the source in the source holder was indeed far enough from the tabletop to minimize backscatter, one MCNP run was done that involved designating the volume behind the source as air with an importance of one, and modeling the table as aluminum. Though this geometry resulted in longer run-time, there was not any difference between it and the void case. Therefore, the source holder was doing its job of suppressing backscatter, and the holder and the volume behind it were justifiably ignored. A similar test was done regarding the steel spacer tubes used to shield the LAAPD from ambient light while ensuring fixed measurement geometry. The presence of the tubes did not affect the results compared to not modeling them, although they did stretch the MCNP run-time to unacceptable lengths. The tubes were therefore not modeled.

The essential materials modeled were the source encapsulation, the air between the source and the scintillator face, the scintillator, and the lucite ring surrounding the scintillator. The source encapsulation was specified by the manufacturer as aluminized mylar of thickness  $0.9 \text{ mg cm}^{-2}$ , though no precise elemental weight fractions were

given. Therefore, the encapsulation was modeled as a pure mylar disk of  $0.9 \text{ mg cm}^{-2}$  thickness, on both sides of the source, with a radius of 12 mm. Elemental weight fractions were taken from the NIST web site (NIST 2004), as were those for lucite. The atom fractions for the scintillator material were taken from the Saint-Gobain data-sheets for BC-430 and BC-802 plastics.

The reflective paint on the scintillator surface is a titanium dioxide type, of unknown thickness. To determine if it had any influence on the simulations, a layer of pure  $\text{TiO}_2$  was modeled on the scintillator surface, at thicknesses up to 50 microns. No effect was noted, so the paint was not modeled in the final MCNP runs.

The source size, inside the encapsulation, was determined to be no more than 5 mm in diameter. To determine if source size had an effect on the results, they were modeled as disks of radius 2.5 mm, inside the same encapsulation as before, and compared to the point source cases. There was no discernable difference; therefore, the sources were modeled as points for all simulations.

Omitting either the encapsulation or the air, or both, resulted in spectra that differed significantly from spectra that included both. The encapsulation acts as a source of secondary “knock-on” electrons that show up as excess events at lower spectral energies. The air acts as a filter of low-energy electrons; without it, more excess electrons reach the scintillator than actually should. For these reasons, the air and mylar encapsulation were modeled for all simulations. The final MCNP simulation geometry is illustrated in Fig. 4.20. Structure parameters are listed in Table 4.8.

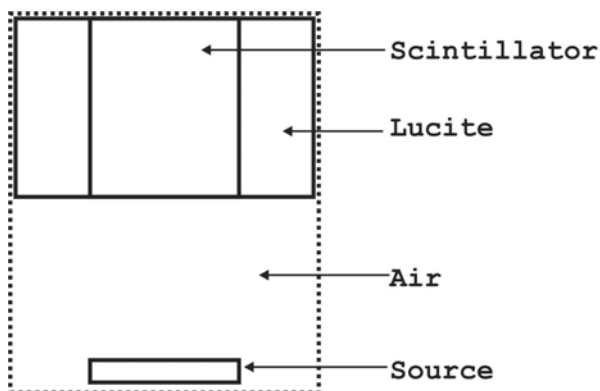


Fig. 4.20: Profile of the MCNP simulation geometry (not to scale). All area outside the dotted boundary is void, with an importance of zero.

Table 4.8. Structure parameters for MCNP modeling.

Structure	Density ( $\text{g cm}^{-3}$ )	Elemental composition (atom fraction)
Air	0.001293	N: 0.8; O: 0.2
Lucite <sup>a</sup>	1.19	H: 0.533; C: 0.334; O: 0.133
Mylar <sup>a</sup>	1.40	H: 0.363; C: 0.455; O: 0.182
BC-430 <sup>b</sup>	1.032	H: 0.526; C: 0.474
BC-802 <sup>b</sup>	1.19	H: 0.533; C: 0.334; O: 0.133

## 4.10 Spectral enhancement

### 4.10.1 Overview

Detection and measurement of beta radiation with this detector, or any other, involves a sequence of events. First, a particle is emitted from a source, passes through some materials such as a source covering and air, and interacts with the detector. At that point the internal processes of the detector take over. Scintillation light may be

<sup>a</sup> Data from <http://physics.nist.gov/cgi-bin/Star/compos.pl>

<sup>b</sup> Data from Saint-Gobain datasheet



produced, or an electric charge is created, or some other physical reaction occurs that can be measured, generally in a way that produces a signal proportional to the amount of energy deposited. From there, a variety of electronic elements process the signal, culminating in an output signal (i.e., an energy spectrum) that can be analyzed. Every step of the process creates some uncertainty in the final result. The sum of these uncertainties represents the response of the detector system, and determines the usefulness of the device.

The chain of events outlined above can be divided into two parts: those events that don't include signal analysis, and all those events that deal with signal processing. The interface between these domains is the detector volume itself, wherein a temporal overlap occurs. The non-signal phase lasts until the beta leaves the system, either absorbed in, or deflected from, the detector volume, but as in our detector, it doesn't deal with the scintillation light produced. The signal-analysis phase starts when the first scintillation photon is created.

Consider a typical non-signal chain of events: A beta particle is emitted from some radioactive source. The beta initially possesses kinetic energy determined by the laws of physics that govern that particular beta emitter's spectral shape. Immediately, however, the beta begins to lose energy as it interacts with its surroundings. It may lose energy in a source cover, then in some other intervening material, such as air. When the beta finally reaches the detector, it will no longer possess its original kinetic energy. Finally, the beta may interact in the detector in such a way that even the fraction of energy it retains after its passage from the source, is not transferred fully.

Therefore, even before the detector's uncertainties begin to influence the process via the signal-analysis phase, the beta presented to it is no longer the original quantity of interest.

If the detector output is to be useful, the detector must convey the information presented to it, such as the absorbed beta energy, from one stage to another without distorting it beyond recognition. There will always be some distortion. In a scintillation detector, there is uncertainty in the number of scintillation photons produced per unit energy deposited, uncertainty in the fraction of photons collected by the photosensitive surface, uncertainty in the photosensor's quantum efficiency, etc. Given some reasonable knowledge regarding all the uncertainties in this chain of events, such as the governing statistical distributions and their means and deviations, it is possible to deconvolve the uncertainties from the end result, thus producing an output that more faithfully represents the original energy emission spectra. But such an effort will not correct the problem of the beta particle's energy degradation during the non-signal phase. The non-signal domain must be dealt with separately.

Assuming the successful stripping from the measured spectrum of all the uncertainties related to the signal-analysis phase, what remains represents a 100% energy absorption efficiency in the detector volume. If a 500 keV event is recorded, it means a beta deposited 500 keV in the detector volume. It does not mean that the energy of the beta was 500 keV when it deposited that energy; the beta might have possessed 600 keV of kinetic energy and only left 500 keV of it behind. Herein is discussed the origin of this fractional energy deposition, the effect it has on the beta spectrum, and

the means of filtering it out in order to produce a truer representation of the beta spectrum, in simulated and in measured cases.

The non-signal phase can be subdivided into two parts, those events that degrade the beta energy before it strikes the detector, and those events that degrade the beta energy as a consequence of interacting with the detector. This suggests that a total solution to the problem of fractional energy deposition (FED) is a combination of simpler solutions. This approach will be taken by simplifying the situation as follows: the beta source is an un-encapsulated, isotropic point in a vacuum (i.e. no backscatter and no energy degradation). This leaves just the beta interaction with the detector as a source of FED events.

The detector volume is the cylinder of BC-430 scintillator plastic described in an earlier section. Analysis of the FED events relies on Monte Carlo N-Particle (MCNP) simulations (see section 4.9). MCNP allows the simulated detector volume to serve as a “perfect” detector- nothing disturbs the beta on its way from source to detector, and the detector will faithfully record events with 100% efficiency. Since MCNP is a statistical process, it cannot be claimed that the detector will record each event with 100% accuracy as to energy deposited, but for simplicity, this has been assumed.

#### **4.10.2 Analysis**

The most basic question to be asked is whether, in the absence of source encapsulation and air gap, there is any adverse effect on the beta-particle energy when it

meets the detector. The only variable in this scenario is the angle of incidence that the beta path makes with the detector face- except for the few betas that strike the detector at normal incidence, all will strike at some angle depending on how far from the detector's center this occurs. This obviously boils down to answering the question, does the angle of incidence of the beta with the detector normal result in FED events, and if so, why?

The simplest way to test the angle-of-incidence (AI) effect is to focus mono-energetic electrons at the detector face, at a variety of angles. If they all produce events at the incident electron energy, then there is no AI effect. Incident electrons of energies 100 keV and 1 MeV (100,000 for each energy) were directed sequentially, at angles to the normal of 0, 15, 30, 45, and 60 degrees, at the detector. The source-detector distance was maintained at 10 mm; in order to preclude the possibility of an electron passing through the edge of the detector, and thereby depositing only a fraction of its energy, the detector's diameter was increased sufficiently to accommodate incident angles of up to 60 degrees without risking an edge event (Fig.4.21). Results are illustrated in Figs. 4.22 and 4.23.

Even at zero degrees angle-of-incidence, there are events recorded at energies less than the incident electron energy. The greater the angle of incidence, the more sub-maximum events occur. Most events are still at the maximum energy (not shown on the graphs, to avoid scaling problems), regardless of angle, but the quantities that occur at lesser energies are large enough to arouse the suspicion that the spectrum might be significantly degraded as a result. The answer to the initial question, whether

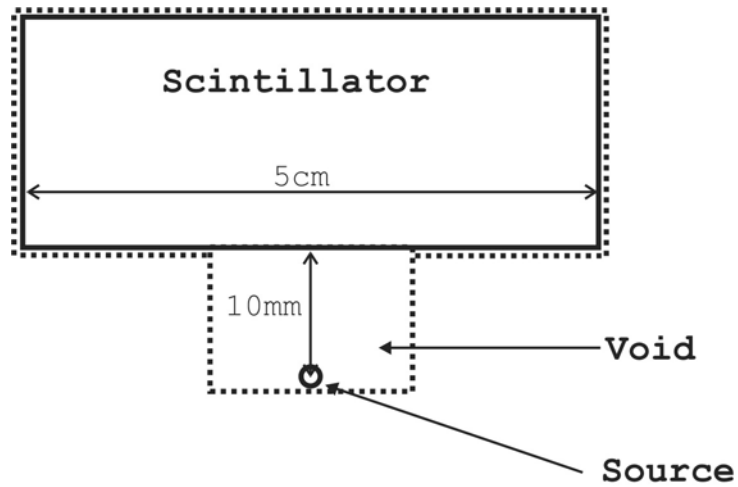


Fig. 4.21: Geometry used to analyze the AI effect. Because the scintillator extends far beyond the area where betas may intersect it, there is no possibility that a beta will pass through the scintillator's edge, thereby depositing only a fraction of its energy. All potential FED events are limited to those resulting from scatter off the surface.

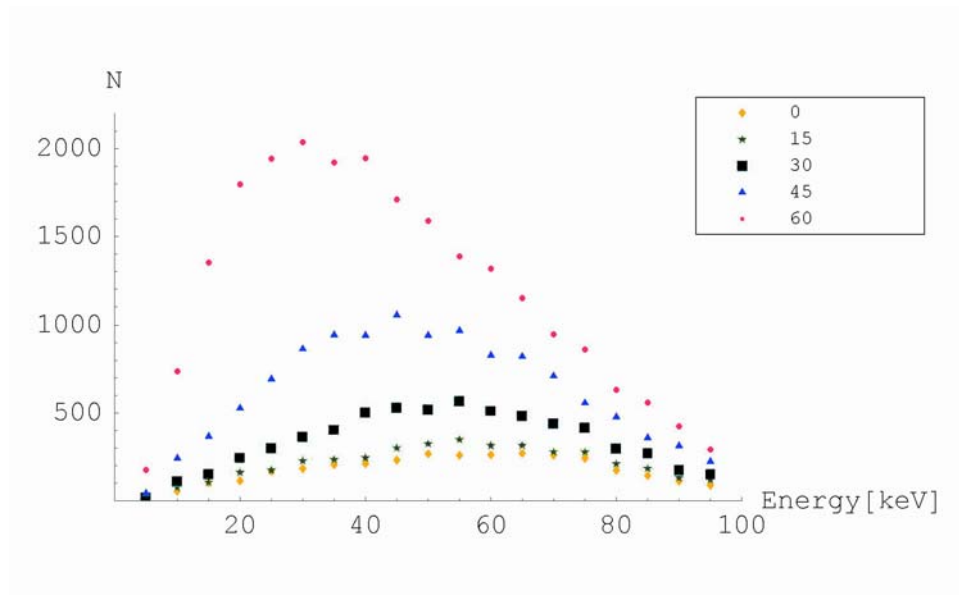


Fig. 4.22: Energy deposition spectrum for 100 keV electrons incident on the scintillator at various angles.

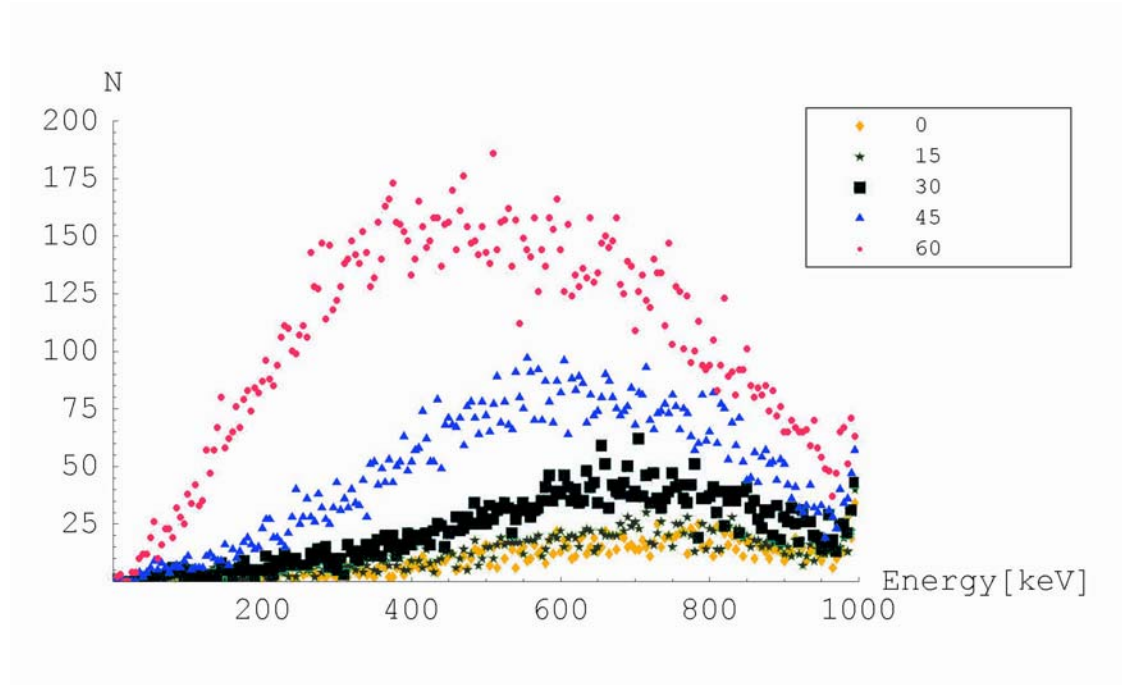


Fig. 4.23: Energy deposition spectrum for 1 MeV electrons incident on the scintillator at various angles.

or not there is an AI effect, has been answered in the affirmative. The angle-of-incidence is important when considering how to attack the problem of fractional energy deposition.

On observing the two plots of energy deposition versus angle-of-incidence, it appears at first glance that the higher energy electrons, of 1 MeV, suffer more than the 100 keV electrons from the AI effect. Actually, the opposite is true. There are more sub-maximum events (by a factor of about 1.25) in the 100 keV case; the reason for its relatively sparse appearance is related to the number of energy bins available for the lower-energy events. Both cases used bins 5 keV wide in the MCNP model, so the 1 MeV case has 200 bins available, while the 100 keV case has only 20. The trend is

nevertheless intuitively seen: lower energy electrons scatter more readily than higher energy electrons, resulting in more FED events. To see why this is so, consider that a 1 MeV electron will penetrate more deeply into the detector volume than a 100 keV electron. When that 1 MeV electron then scatters, it has a better chance, by virtue of having penetrated farther, of scattering completely within the detector volume, thus depositing its full energy. To understand why electrons of both initial energies produce more FED events at greater angles, simply consider that as the angle increases, more volume outside the detector becomes available to scatter into, resulting in a greater likelihood of a FED event (Fig. 4.24).

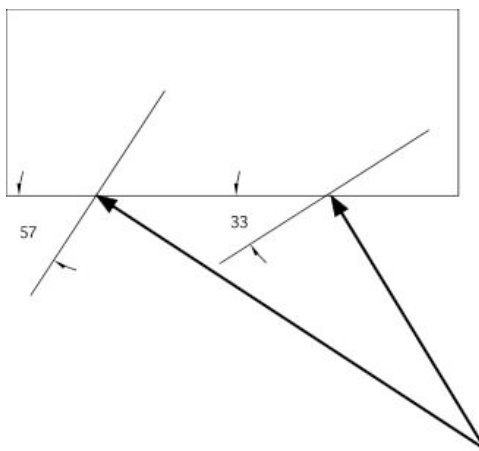


Fig. 4.24: At any energy, a greater angle of incidence will result in a higher probability of scatter leading to a FED event: there is more empty space to scatter into.

The analysis to this point has included only those fractional deposition events that occur when electrons are incident on a plastic scintillator of very broad diameter; the conditions were fixed to preclude the possibility of an electron passing through the

edge of the plastic, thereby depositing only a fraction of its energy. However, the actual detector is of finite extent (15 mm diameter), so the influence this “edge effect” has on the spectrum must be considered. The edge effect is also dependent on the angle of incidence, (the greater the angle, the closer to the scintillator’s edge), so it is considered a part of the AI effect. As it turns out, the edge effect is of paramount importance. To include the edge effect in the analysis, the geometry was changed to that of Fig. 4.25.

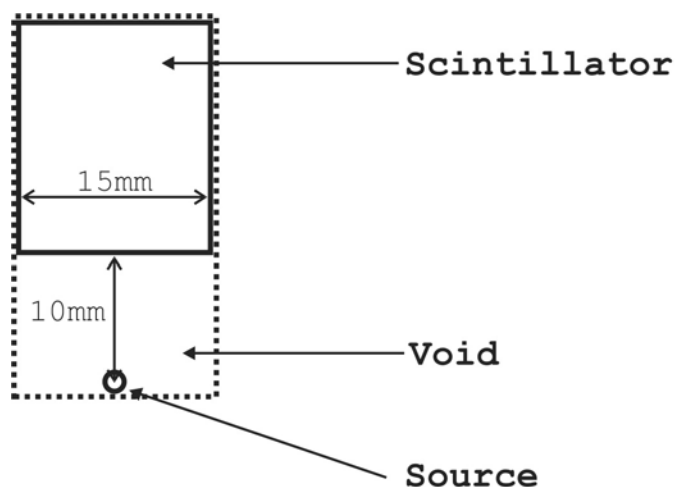


Fig. 4.25: Profile of the MCNP geometry used to analyze the AI effect, including edge effects. All areas outside the dotted line are void, with an electron importance of zero.

Before tackling the problem of removing the AI effect from the spectrum, it is helpful to see an example of a spectrum that has the AI effect present, and its counterpart, a spectrum largely free of the AI effect (Fig.4.26). The spectrum with AI effect included was generated using the source-detector geometry of Fig. 4.25. To eliminate most AI effect from the second spectrum, a source was placed at the center of a hollow



spherical detector, of thickness sufficient to stop all incident electrons. The hollow sphere geometry ensured that each incident electron struck the detector normal to the surface. Results seen in Figs. 4.22 and 4.23 indicated that there is some AI effect even in zero degree incidence cases (due to backscatter from the detector surface), but the effect is smallest at normal incidence, less than 2% of events being AI effect events for the 1 MeV case and about 3.4% for the 100 keV case. The spherical detector configuration simply allows a reasonable comparison between spectra with considerable AI effect present and those with relatively little.

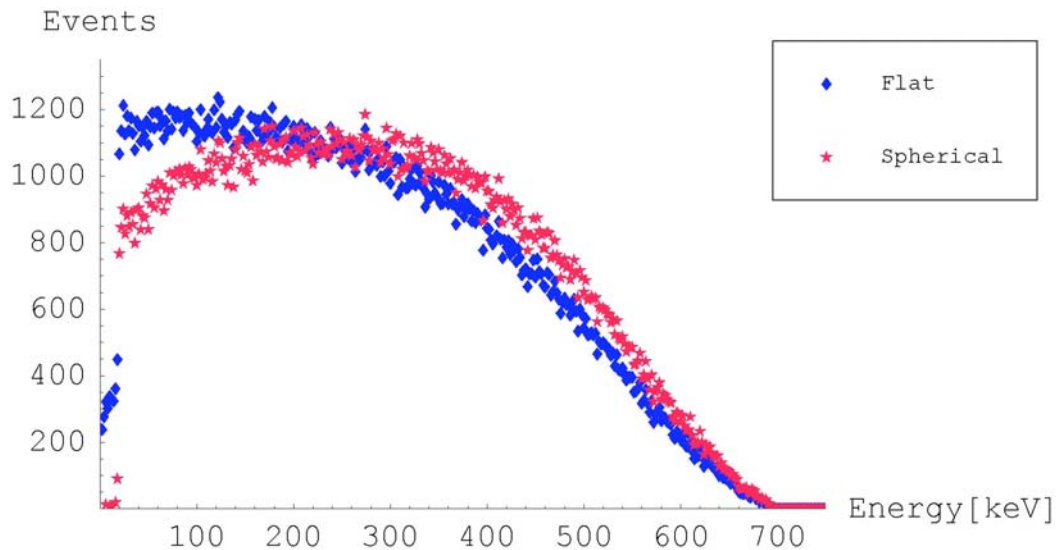


Fig. 4.26: An example of spectra with, and without, the AI effect present. Spectra are from  $^{36}\text{Cl}$ . “Flat” indicates electrons incident on the flat-faced detector; “Spherical” indicates electrons incident on the inside surface of a hypothetical spherical detector.

Examination of Fig.4.26, keeping in mind the absence of source encapsulation and air, suggests that the AI effect might play a prominent role in determining beta spectral shape. The effect is seen at all energies except the very highest, where the few events recorded do not allow significant differences to appear. It now remains to implement a systematic removal of these AI effect events, which cause betas to deposit only a fraction of their incident energy in the detector. Since angle-of-incidence events lead to fractional-energy-deposition events, the total process will be abbreviated “AFED”, for “angular fractional energy deposition”.

#### **4.10.3 Modeling the AFED effect**

Beta spectra are continuous phenomena, but in MCNP they are modeled by choosing a series of energy values, with their associated emission probabilities, and interpolating between those known energies to determine the unknown emission probabilities. So long as the functions vary slowly between known values, this produces accurate emission spectra. The same approach is taken in modeling the AFED. A series of mono-energetic, isotropic sources was defined spanning the energy range of the beta emitters of interest ( $^{14}\text{C}$ ,  $^{36}\text{Cl}$ , and  $^{90}\text{Y}$ ). Yttrium-90 has the largest endpoint beta energy, 2,281 keV, so the range of source energies went up to 2,300 keV. From 0 to 100 keV, deposited energy distributions in the detector model of Fig.4.25 were calculated at 20 keV intervals. From 100 to 2,300 keV, deposited energy distributions were calculated at 100 keV intervals. Each distribution was generated from one million isotropically emitted electrons, of which just over 100,000 intersected the detector vol-

ume. Ultimately, using interpolation, distributions were calculated every 2 keV, a value corresponding to the energy interval for the MCNP pulse height tallies. The mono-energetic emission energy is referred to as the “primary energy”, and the events at non-primary energies are referred to as “fractional deposition events”. Table 4.9 illustrates an abbreviated version of the data for the 600 keV distribution. Results from two of the mono-energetic, isotropic sources are seen in Fig.4.27.

Figure 4.28 is a plot of the fractional deposition values at an arbitrary 300 keV, for kernels ranging from 400 to 2300 keV. The slowly varying nature of the values, a characteristic at all energies, indicates that linear interpolation is a valid technique even for kernels calculated as far apart as 100 keV. Interpolation error is therefore minimal, and can be further minimized by calculating kernels at closer intervals, if desired. In the previous section it was noted that there are two possibilities that can lead to a FED event: scatter out of the detector, and passage of the beta through the detector’s edge. In order to determine the relative contribution of fractional depositions due to scatter alone, distributions were also calculated at 100 keV, 1 MeV, and 2 MeV, for the large diameter scintillator of Fig. 4.21. In this way, the distributions did not include any edge effect. The results were dramatic: whereas for the 2 MeV distribution with edge effect present, only 37% of the incident betas were recorded at 2 MeV, for the 2 MeV distribution without edge effect present, 97% of the incident betas were recorded at 2 MeV. For 1 MeV distributions the results were 65% (with edge effect) and 96% (without edge effect). For 100 keV distributions, with edge effect and without edge effect results were 93% and 94%, respectively. The ratios of fractional

Table 4.9. Example of data calculated from a mono-energetic, isotropic, electron point source incident on the scintillator. Data is for 600 keV electrons. One million electrons were emitted, of which just over 10% intersected the detector volume.

Energy (keV)	Counts	Fraction of total
2	143	0.001426
4	130	0.001327
6	137	0.001386
8	111	0.001207
10	134	0.001337
12	102	0.001017
...	...	...
584	14	0.000140
586	7	0.000069
588	10	0.000099
590	13	0.000129
592	14	0.000139
594	8	0.000079
596	7	0.000069
598	17	0.000169
600	79350	0.791489
Total counts:	100254	

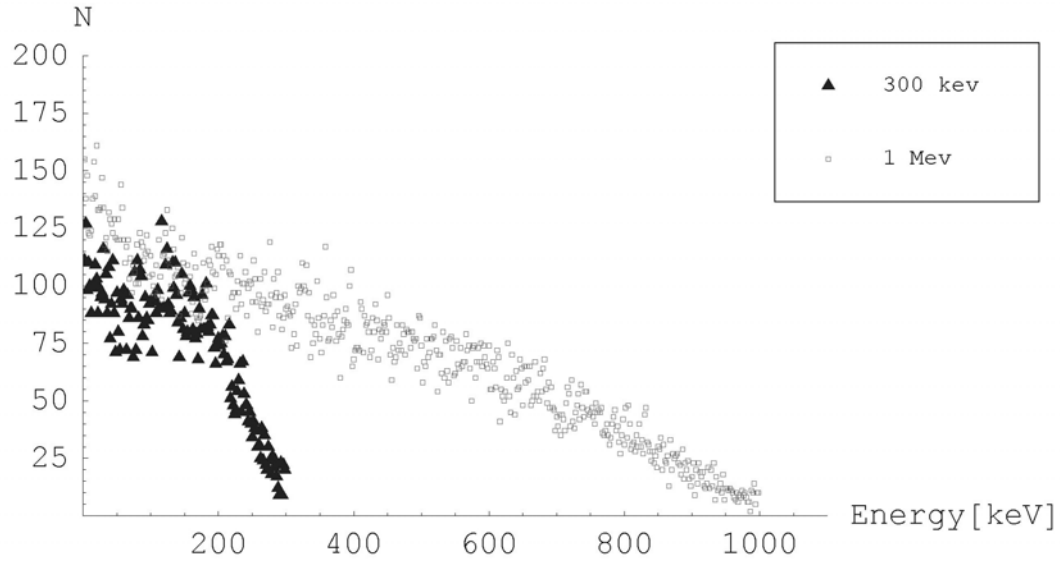


Fig. 4.27: Energy spectra for monoenergetic electrons from point isotropic sources of energies 300 keV and 1 MeV, incident on the scintillator. The primary energy values are not shown for reasons of scale.

depositions due only to scatter and due only to edge effects were 5.6 (100 keV betas), 0.12 (1 MeV betas), and 0.04 (2 MeV betas). Clearly, the edge effect becomes dominant as the energy increases, whereas at lower energies, scatter is more important. The total effect, edge effect plus scatter, is modeled by the distribution at each primary energy and constitutes the AI effect.

The distribution data is analyzed in the following manner. At every energy less than the primary energy (2 keV interval width), the number of AFED events is known. If there had not been an AI effect, all the events would have been recorded at the primary energy. But since there are AI effect events, and fractional deposition occurs, the fraction of AFED events that occurs at each lower energy is determined by simply di-

viding the number of events at each energy by the total number of events. For example, for the 500 keV distribution, the total number of events was 100,278. However, only about 82% of them were recorded at the primary energy, leaving 18% to be distributed across all the energies below 500 keV. At 300 keV, for instance, there were 78 events recorded; this is a fractional deposition of 78 over 100,278, or 0.000778. The same analysis applies to every distribution. The fractional deposition data derived from each primary-energy distribution is called the “kernel” at that primary energy.

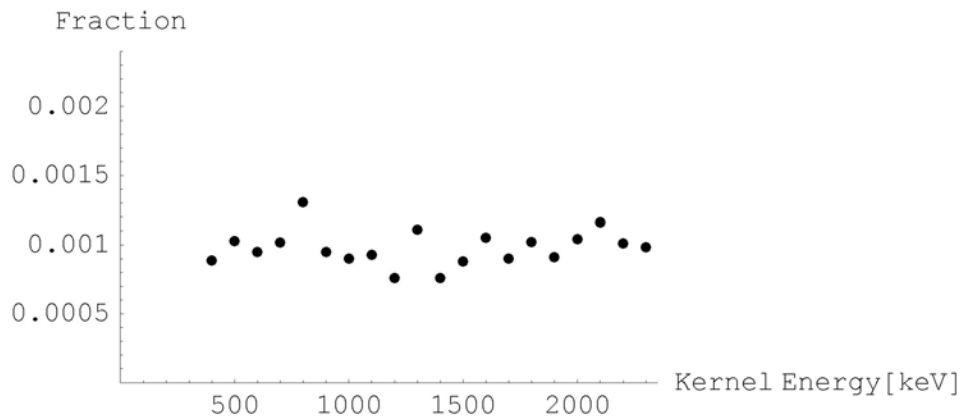


Fig. 4.28: Fractional deposition values at 300 keV, for kernels covering the range 400 to 2300 keV.

#### 4.10.4 AFED removal algorithm

This fractional deposition information leads to a straightforward means of removing the AFED events from the detector-response spectra. The process proceeds as follows: (1) Start at the endpoint (maximum) energy of the detector-response spec-

trum; (2) Retrieve the kernel corresponding to that energy, either by lookup of the MCNP derived kernels or interpolation between MCNP kernels; and (3) Divide the number of counts in the spectrum, at the endpoint energy, by the fractional deposition for that energy. For example, if 500 keV were the endpoint energy, the number of counts at 500 keV would be divided by 0.82. This alters the number of counts at the endpoint energy so it now represents the value it should have had, had there been no AFED events. Since the total number of counts is a value that must be preserved in each spectrum, the number of counts added at the endpoint energy must be accounted for by subtracting an equal number of counts from the lower energies. This is done by stepping energy bin by energy bin, toward zero, and subtracting from each a number of counts proportional to the fractional deposition value at that energy. For example, the number of counts at 300 keV is adjusted by subtracting from it the product of the total counts (100,278) and the fraction of counts (0.000778) that ended up at 300 keV, but should have been recorded at 500 keV. The process now repeats for the entire spectrum. For the 500 keV endpoint case, for instance, the next energy considered would be 498 keV: the kernel would be retrieved, and all the adjustments made. At the end, the spectrum will be free from most AFED events.

#### **4.10.5 Algorithm implementation**

Simulated detector response spectra from  $^{14}\text{C}$ ,  $^{36}\text{Cl}$ , and  $^{90}\text{Y}$  were created using MCNP; these became the test subjects for the algorithm. Input data for the spectra came from the Radiation Dose Assessment Resource (RADAR) website (RADAR

2003). A Mathematica program was written to implement the algorithm. To format the MCNP data files properly for use in Mathematica, they were first imported into Microsoft Excel, and then saved as text files using Microsoft WordPad. As noted previously, MCNP kernels were calculated down to 100 keV at 100 keV intervals, then every 20 keV. Below 20 keV, no interpolation of kernels was done, since no calculated kernel existed below this energy. In practical terms this meant that there were no primary energy adjustments made below 20 keV, nor were the corresponding fractional deposition adjustments made. All less-than-20 keV spectral energies were adjusted for all kernel energies above 20 keV. Overall, this low-energy neglect was of negligible impact. If it had proven to be important, primary kernels could have been calculated below 20 keV.

In addition to the lack of primary adjustment below 20 keV, for each kernel there is an energy range for which no interpolated values can exist. For example, consider the 600 and 700 keV kernels. The energy range between 602 and 698 keV contains no common fractional energy deposition values (since the 600 keV kernel stops at 600 keV). For instance, it is impossible to calculate FED values between 602 and 648 keV for the interpolated 650 keV kernel (Table 4.10). Instead, each interpolated kernel includes only calculated FED values up to the next lowest MCNP generated kernel. For the 650 keV interpolated kernel, for example, there are only FED values up to 600 keV. This introduces some error in the algorithm, but the data indicate that most of the FED events are located 100 keV or more below the primary energy, so this error is quite small.



Table 4.10. The 600 keV and 700 keV kernels were calculated using MCNP; the 650 keV kernel is interpolated using the 600 and 700 keV kernels. The fractions from 600 through 648 keV are not calculated for the 650 keV kernel, because the 600 keV kernel does not have values in this range. Since those fractions are not calculated, a small error is introduced in the algorithm, though with little apparent effect. The fraction at the primary energy (650 keV) is calculated by interpolating between the primary fractions for 600 and 700 keV.

600 keV kernel		650 keV kernel		700 keV kernel	
<u>Energy (keV)</u>	<u>Fraction</u>	<u>Energy (keV)</u>	<u>Fraction</u>	<u>Energy (keV)</u>	<u>Fraction</u>
2	0.001426	2	0.001456	2	0.001486
4	0.001297	4	0.001312	4	0.001327
6	0.001367	6	0.001376	6	0.001386
8	0.001107	8	0.001157	8	0.001207
10	0.001337	10	0.001297	10	0.001257
...	...	...	...	...	...
598	0.000170	598	0.000199	598	0.000229
600	0.791489	600	X	600	0.000319
		602	X	602	0.000319
		604	X	604	0.000140
		...	...	...	...
		648	X	648	0.000150
		650	0.773276	650	0.000140
				652	0.000130
				...	...
				698	0.000110
				700	0.755062

## 5 RESULTS

### 5.1 Dosimetry

Measured dose results for surface and shallow cases are seen in Figs. 5.1 through 5.24. Three sources were examined,  $^{36}\text{Cl}$ ,  $^{210}\text{Bi}$ , and  $^{90}\text{Sr}/^{90}\text{Y}$ . Each graph shows the measured spectrum compared to its corresponding MCNP simulation. Inspection of the figures indicates that the measured dose values are lower than the simulated dose values, and that there is a clear energy dependence of the detector response versus the MCNP model. Only at energies approaching 0.5 MeV do the measured results begin to match the modeled results. The  $^{36}\text{Cl}$  surface measurements (Figs. 5.1 – 5.4) resemble the complete  $^{36}\text{Cl}$  energy spectrum, since most of the  $^{36}\text{Cl}$  betas are fully stopped within the first 1 mm of scintillator. For a higher energy beta emitter such as  $^{90}\text{Sr}/^{90}\text{Y}$  (Figs. 5.9 – 5.12), the surface dose results do not resemble the full spectrum, but represent a partial deposition of beta energy, at least for the  $^{90}\text{Y}$  component. This also follows for  $^{210}\text{Bi}$ , in the surface dose case (Figs. 5.5 – 5.8). The shallow cases demonstrate the considerable attenuating effect that the 1 mm layer of inert plastic has on the beta particles before they reach the underlying scintillation layer (Figs. 5.13 – 5.24).

The measured and modeled dose values are summarized in Tables 5.1 through 5.6. In general, the measurements are lower than both the MCNP and VARSKIN models. VARSKIN will only perform dose averaging to a depth corresponding to the maximum beta range, so it will not calculate a dose for the entire shallow volume for either  $^{90}\text{Sr}$  or  $^{36}\text{Cl}$ . For the  $^{90}\text{Sr}/^{90}\text{Y}$  shallow cases, nearly all events are attributable to

the  $^{90}\text{Y}$  component. For this reason, the VARSKIN results for  $^{90}\text{Sr}/^{90}\text{Y}$  shallow cases include only the  $^{90}\text{Y}$  contribution. For the  $^{36}\text{Cl}$  cases, VARSKIN results were omitted.

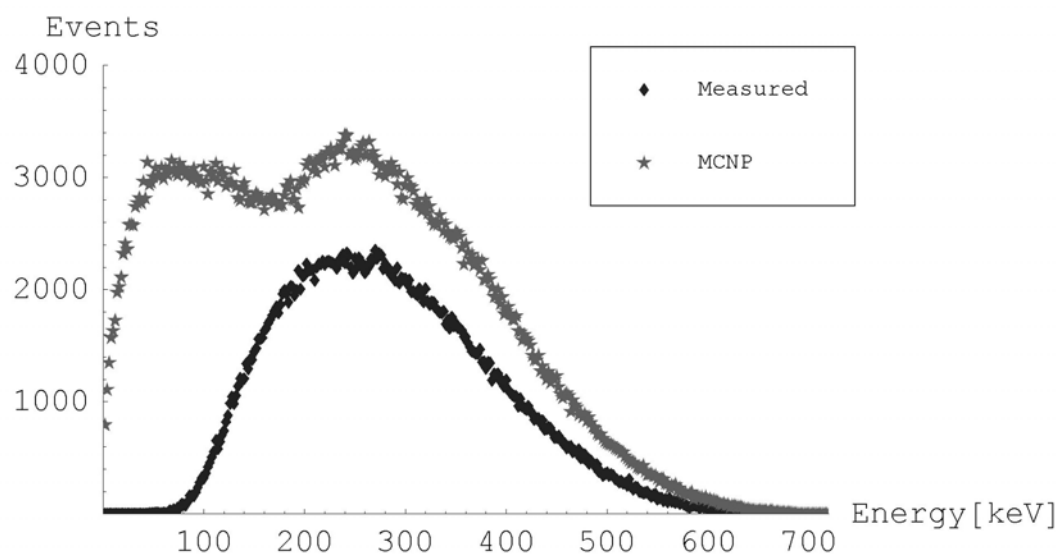


Fig.5.1: Cl-36 surface dose spectrum at source-detector distance (SDD) = 5 mm.

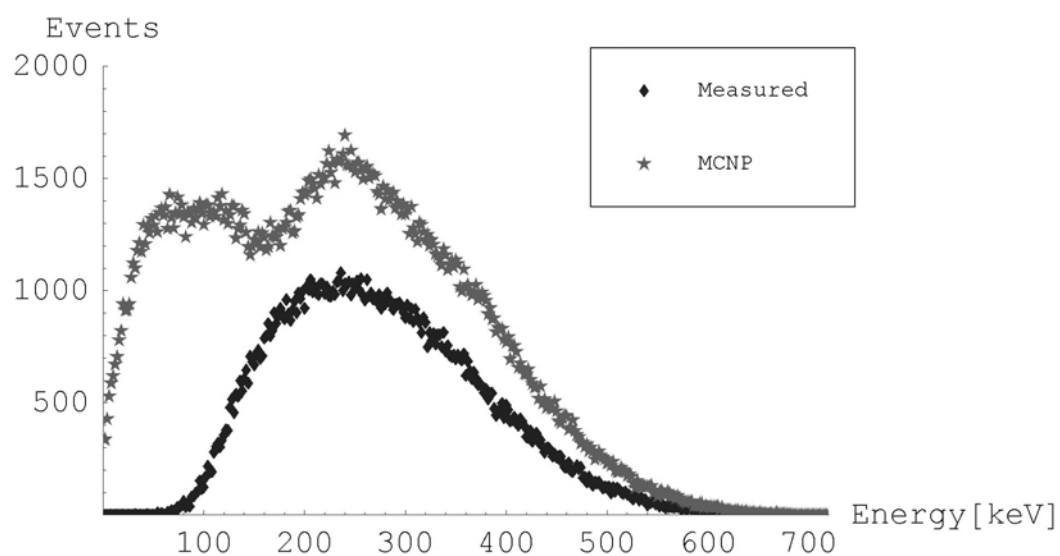


Fig. 5.2: Cl-36 surface dose spectrum at SDD = 10 mm.

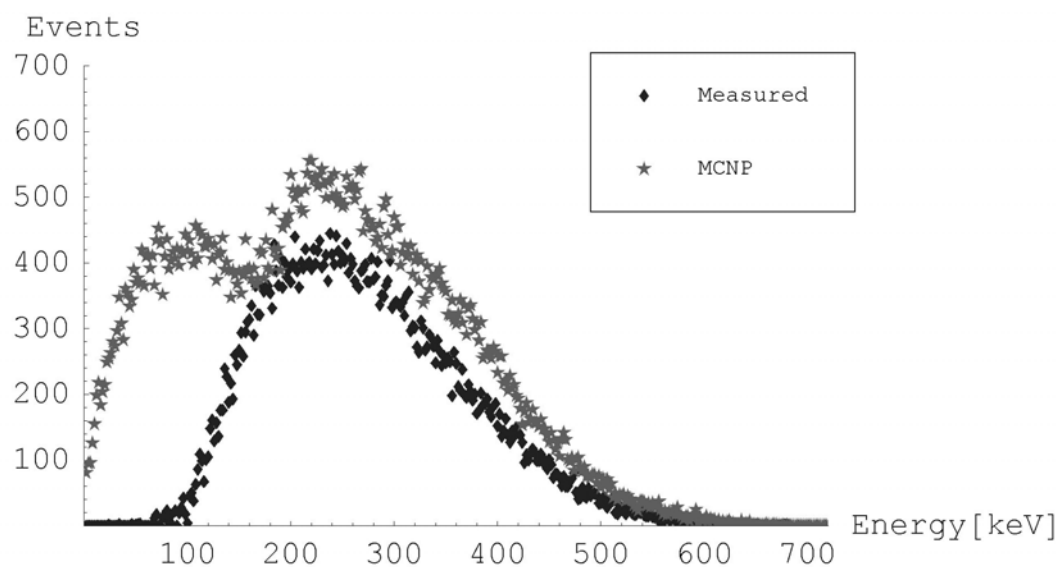


Fig. 5.3: Cl-36 surface dose spectrum at SDD = 20 mm.

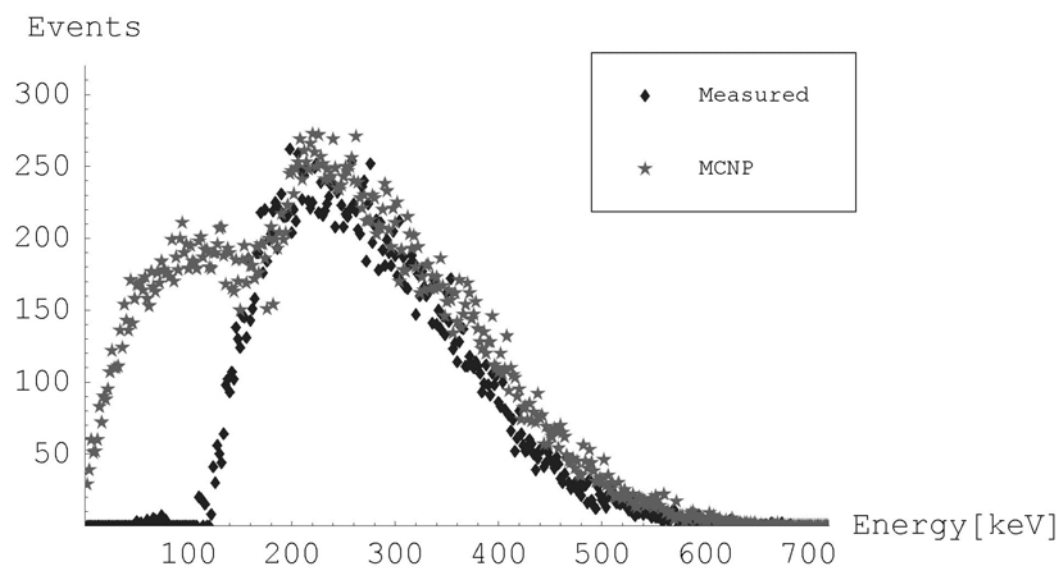


Fig.5.4: Cl-36 surface dose spectrum for SDD = 30 mm.

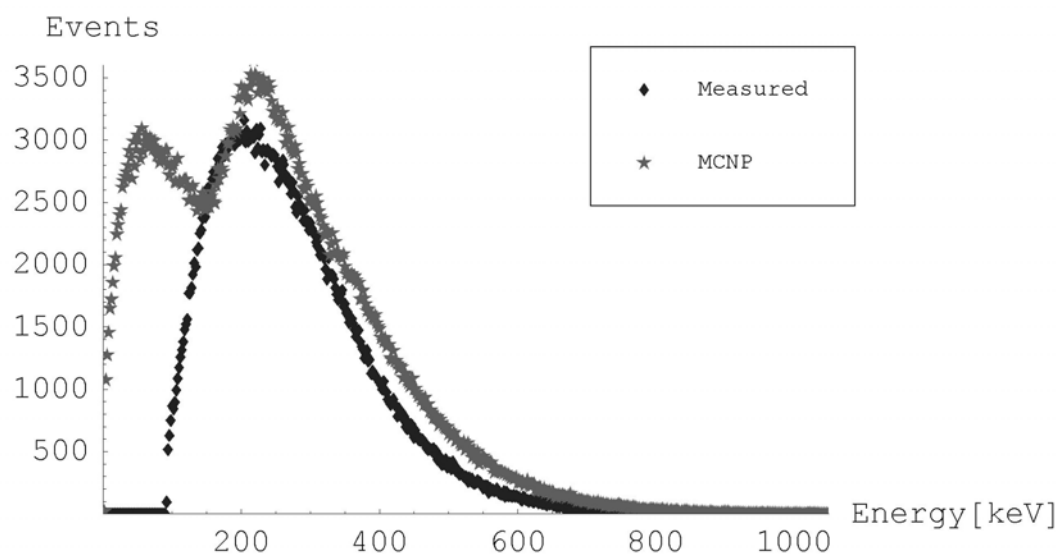


Fig.5.5: Bi-210 surface dose spectrum for SDD = 5 mm.

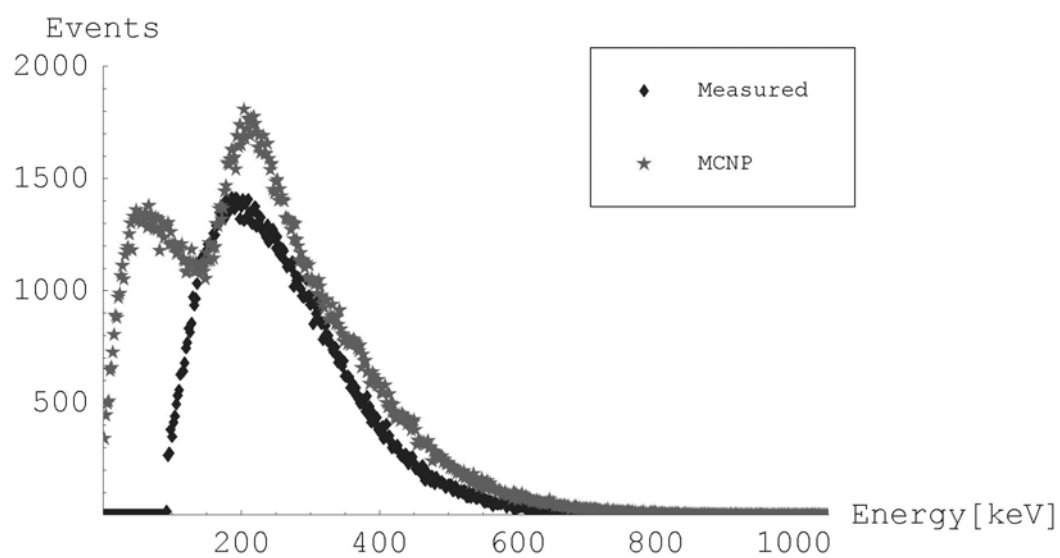


Fig. 5.6: Bi-210 surface dose spectrum for SDD = 10 mm.

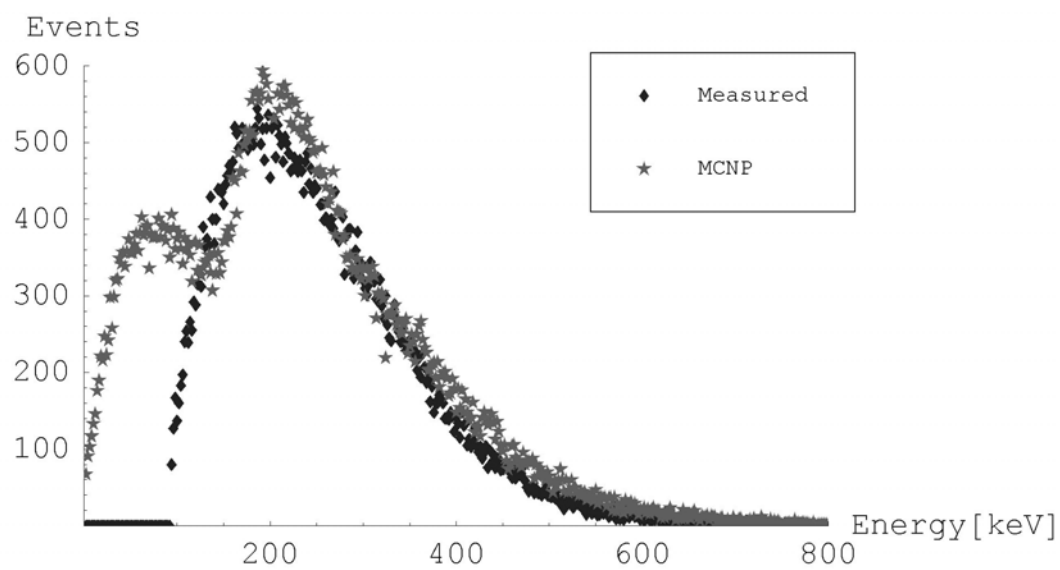


Fig. 5.7: Bi-210 surface dose spectrum for SDD = 20 mm.

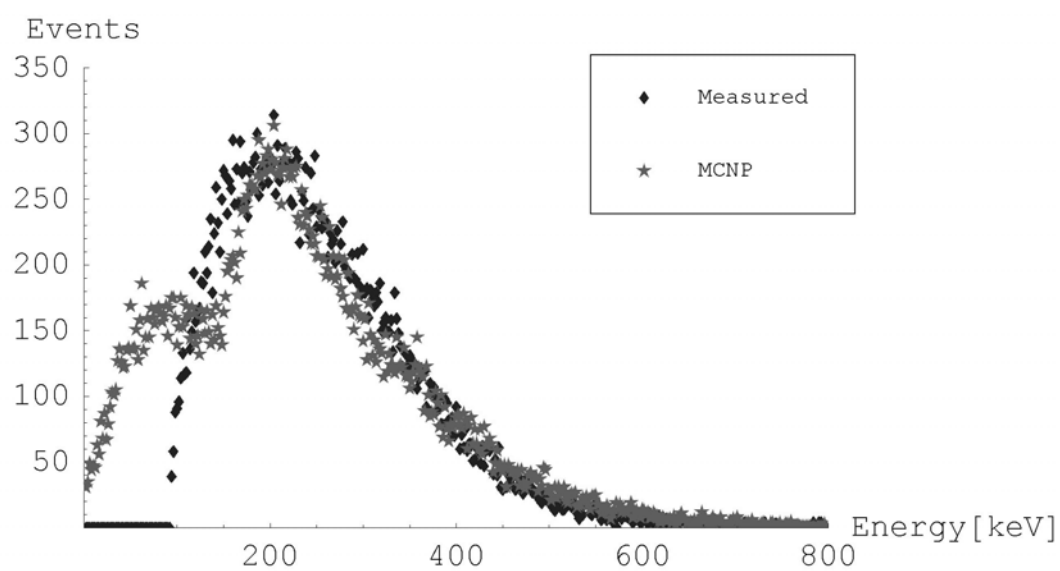


Fig. 5.8: Bi-210 surface dose spectrum for SDD = 30 mm.

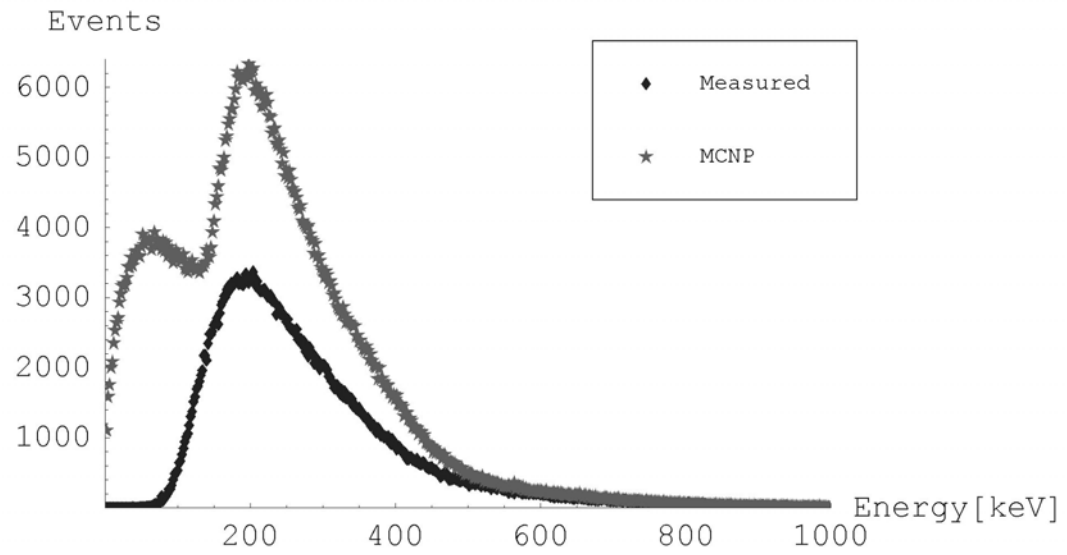


Fig. 5.9: Sr/Y-90 surface dose spectrum for SDD = 5 mm.

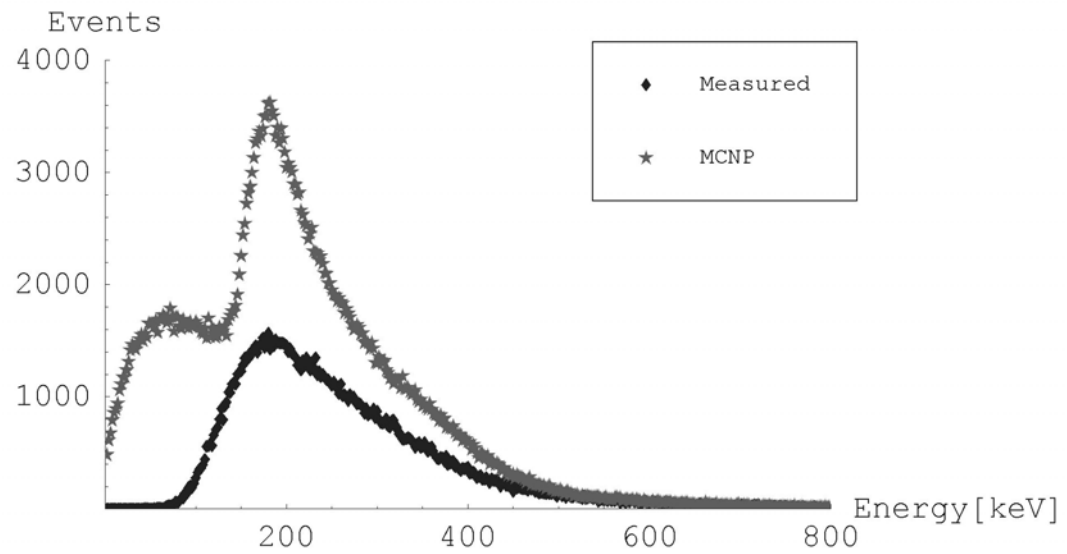


Fig. 5.10: Sr/Y-90 surface dose spectrum for SDD = 10 mm.



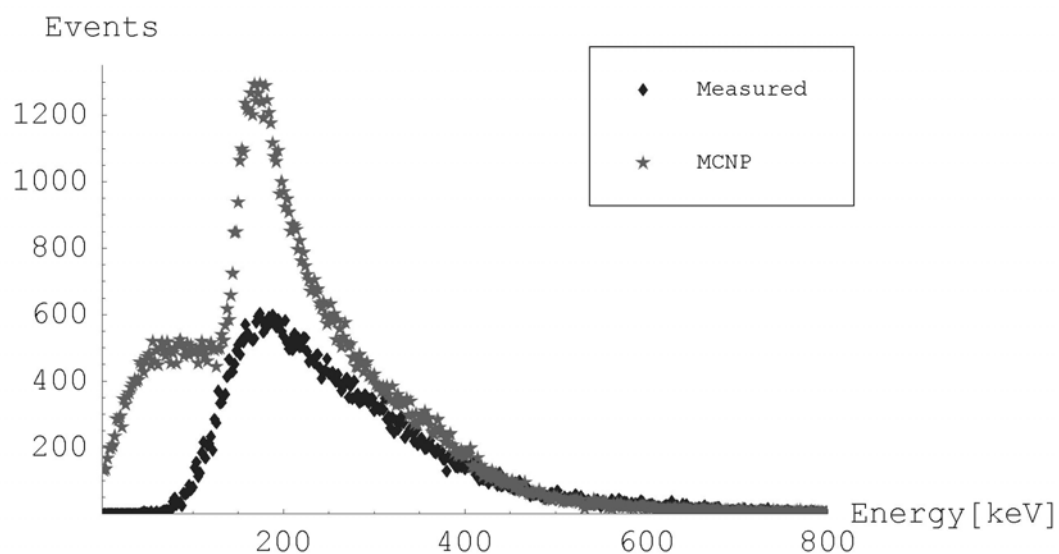


Fig. 5.11: Sr/Y-90 surface dose spectrum for SDD = 20 mm.

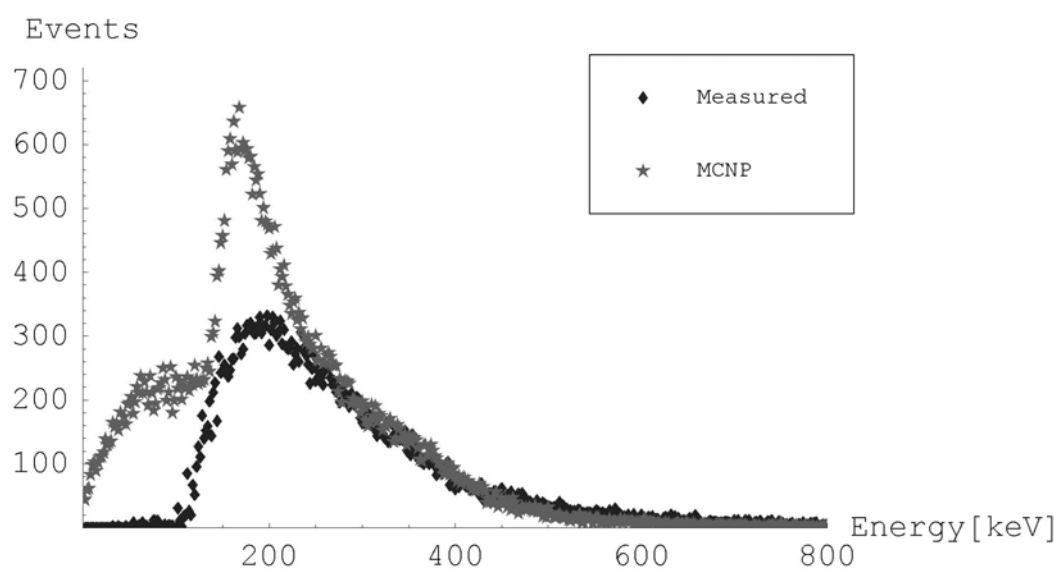


Fig. 5.12: Sr/Y-90 surface dose spectrum for SDD = 30 mm.

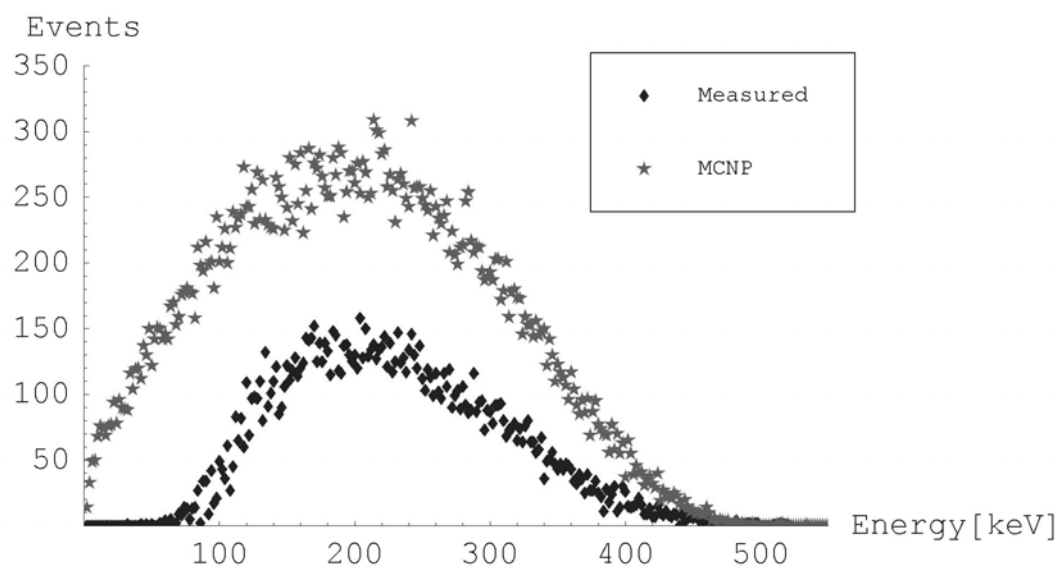


Fig. 5.13: Cl-36 shallow dose spectrum for SDD = 5 mm.

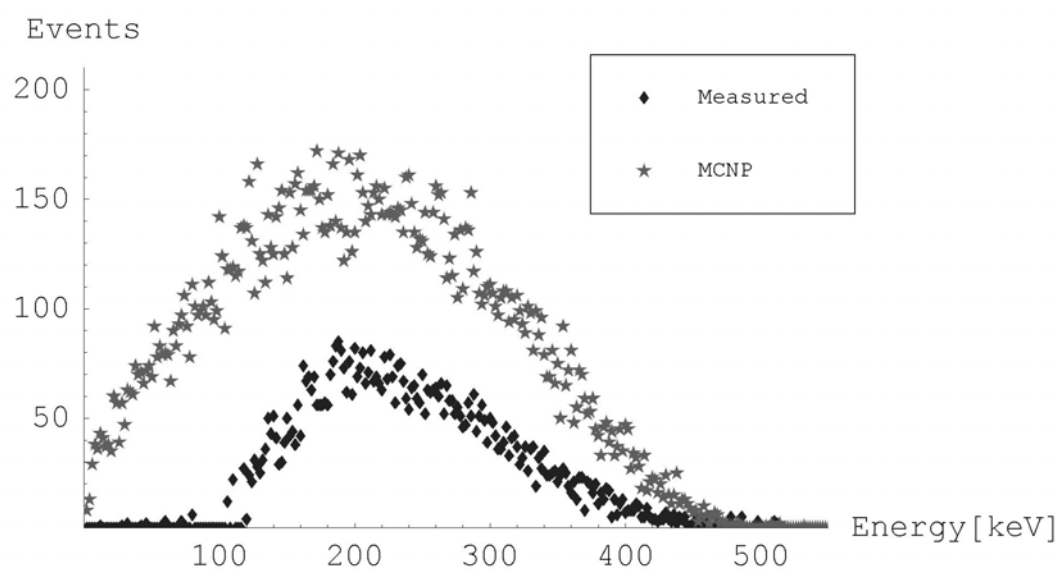


Fig. 5.14: Cl-36 shallow dose spectrum for SDD = 10 mm.

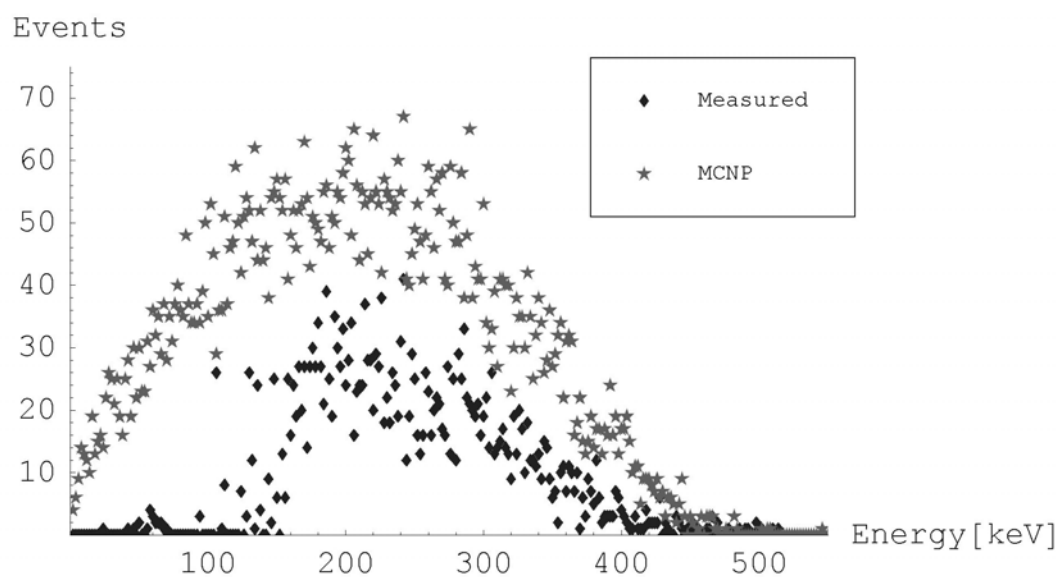


Fig. 5.15: Cl-36 shallow dose spectrum for SDD = 20 mm.

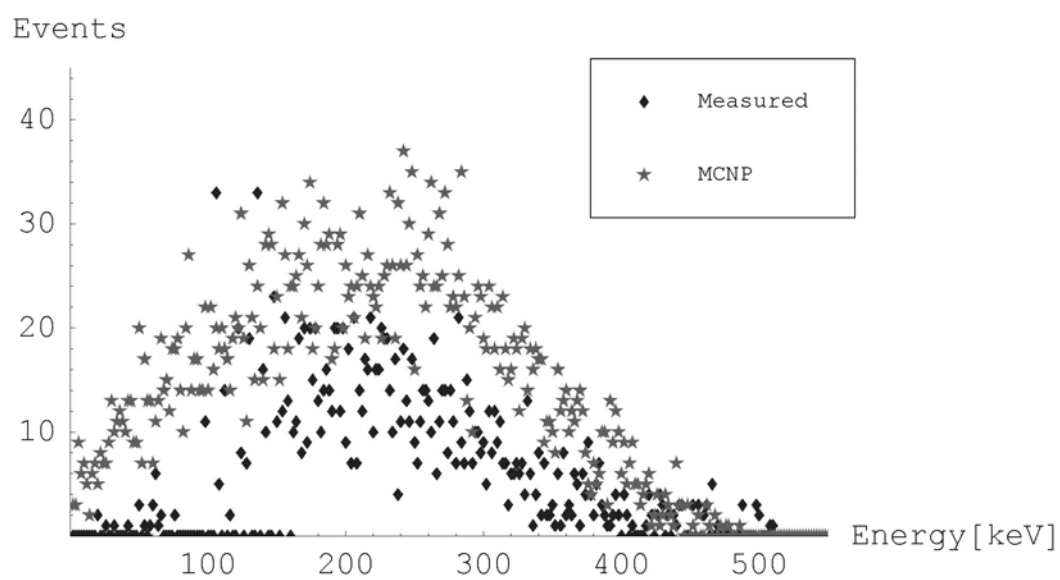


Fig. 5.16: Cl-36 shallow dose spectrum for SDD = 30 mm.

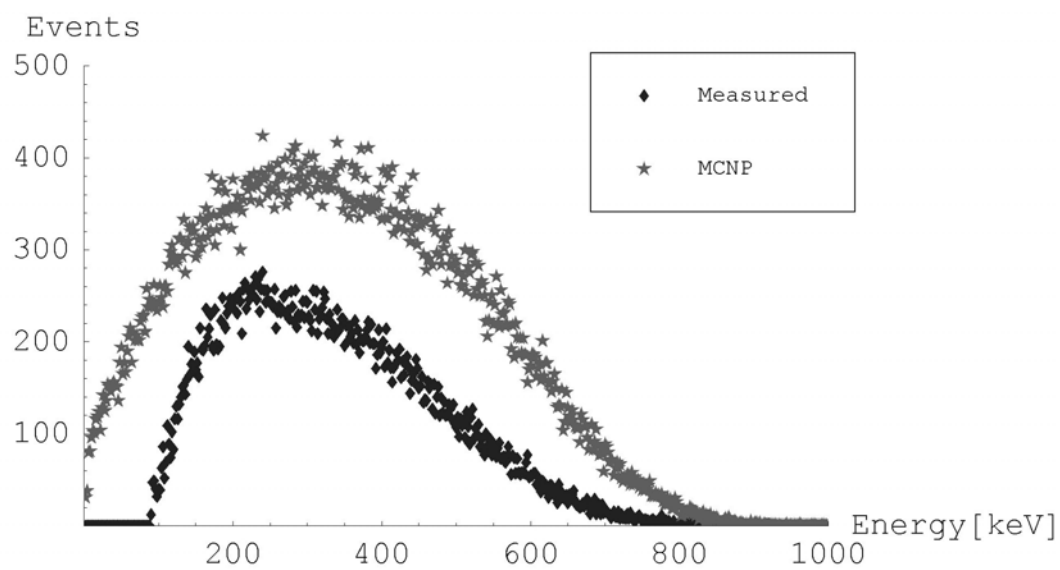


Fig. 5.17: Bi-210 shallow dose spectrum for SDD = 5 mm.

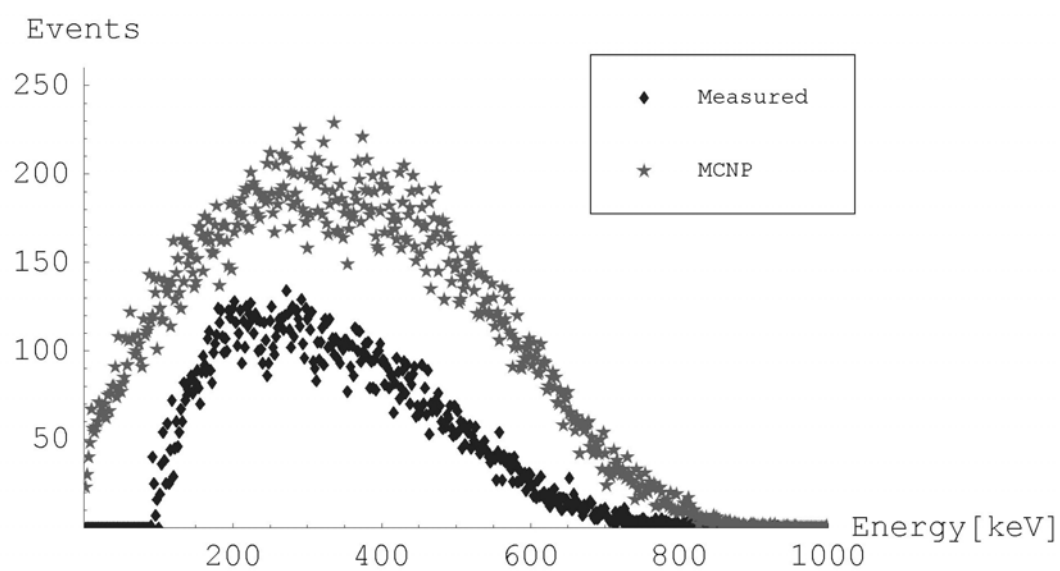


Fig. 5.18: Bi-210 shallow dose spectrum for SDD = 10 mm.

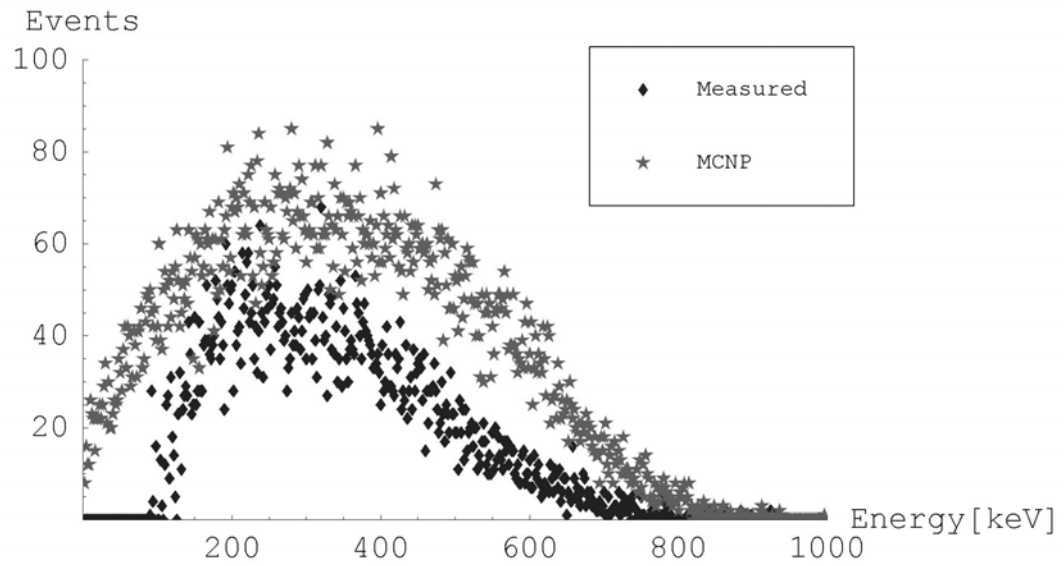


Fig. 5.19: Bi-210 shallow dose spectrum for SDD = 20 mm.

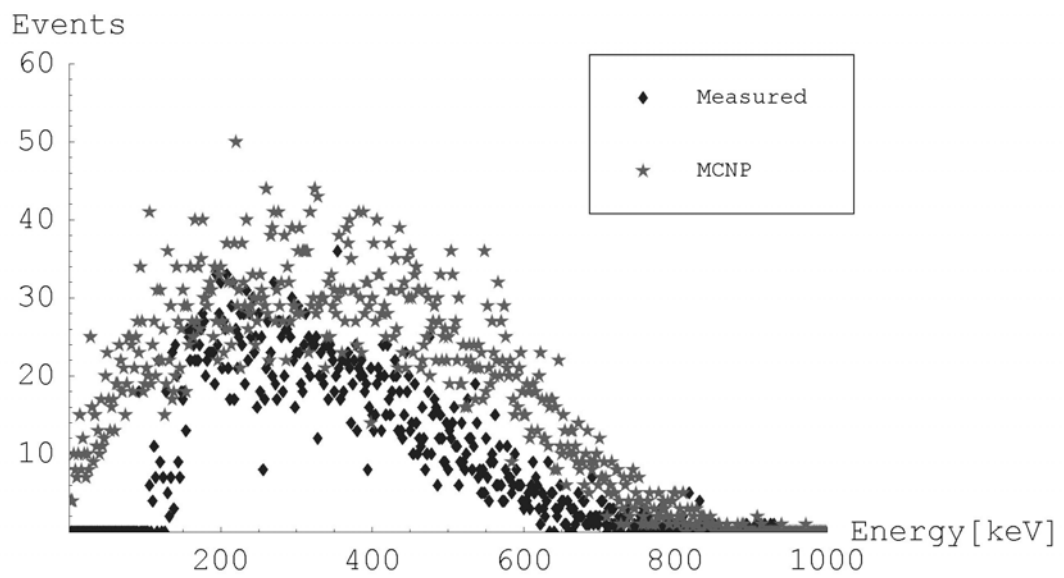


Fig. 5.20: Bi-210 shallow dose spectrum for SDD = 30 mm.

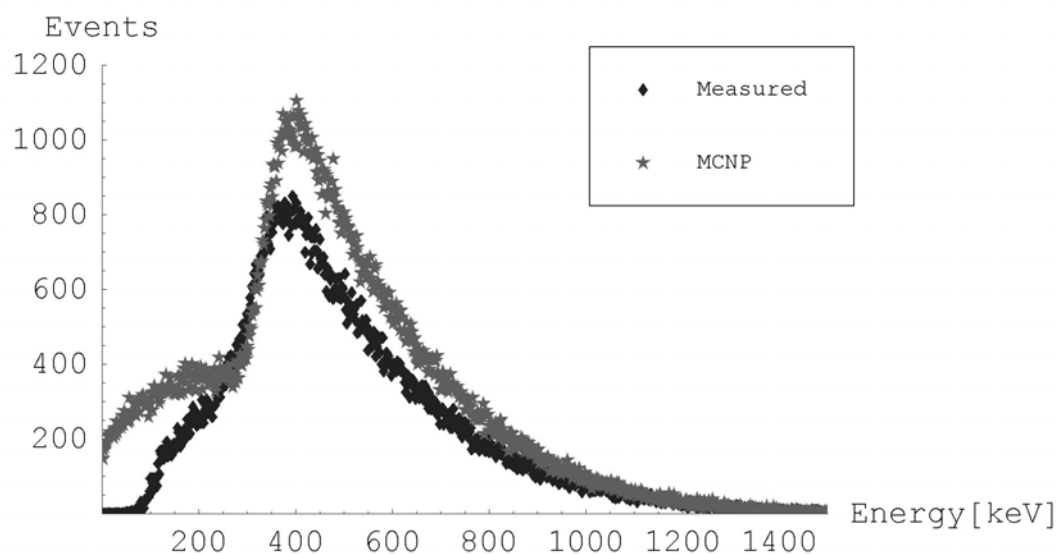


Fig. 5.21: Sr/Y-90 shallow dose spectrum for SDD = 5 mm.

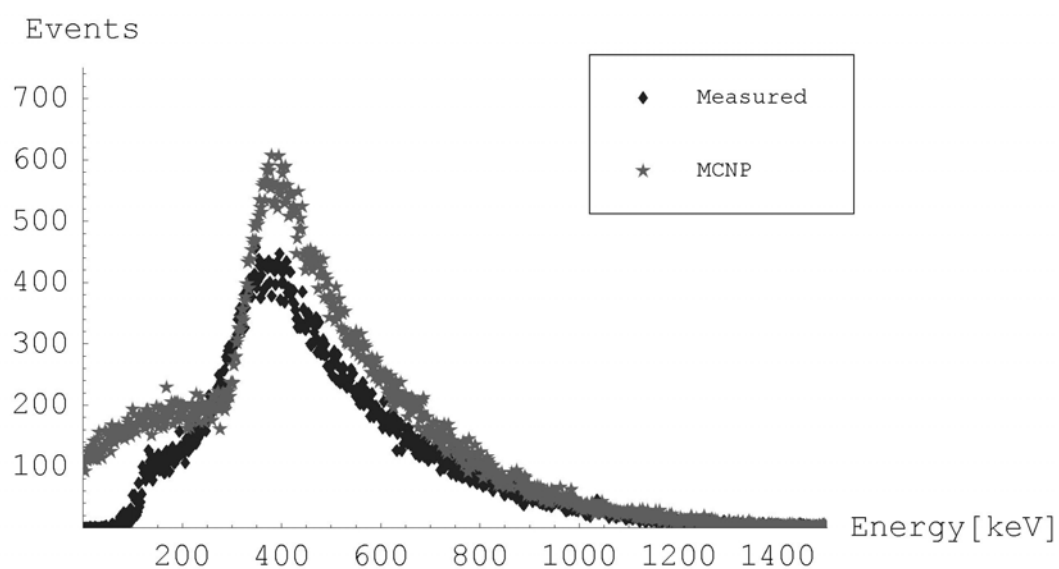


Fig. 5.22: Sr/Y-90 shallow dose spectrum for SDD = 10 mm.

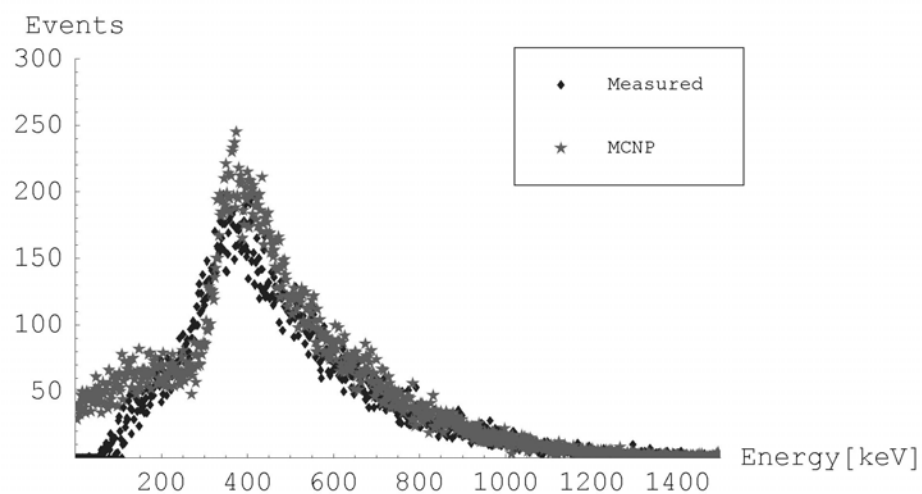


Fig. 5.23: Sr/Y-90 shallow dose spectrum for SDD = 20 mm.

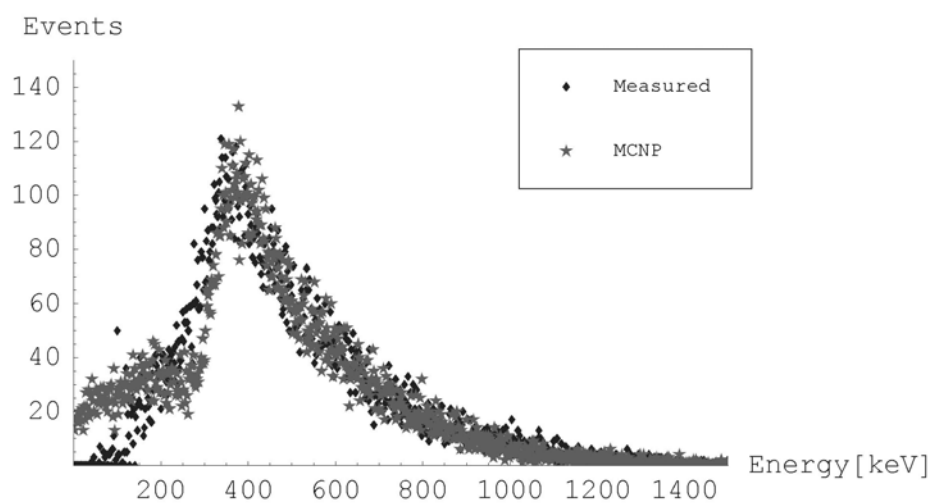


Fig. 5.24: Sr/Y-90 shallow dose spectrum for SDD = 30 mm.

Table 5.1. Measured and modeled surface doses (mGy) at several source-detector distances for  $^{90}\text{Sr}/^{90}\text{Y}$ . The surface is defined as extending to a depth of 1 mm. The mass involved is 0.1824 grams.

$^{90}\text{Sr}/^{90}\text{Y}$			
Source-detector distance (mm)	Measured	MCNP	VARSKIN
5	$9.40 \times 10^{-2}$	$1.65 \times 10^{-1}$	$1.50 \times 10^{-1}$
10	$3.71 \times 10^{-2}$	$6.86 \times 10^{-2}$	$6.16 \times 10^{-2}$
20	$1.47 \times 10^{-2}$	$2.14 \times 10^{-2}$	$1.90 \times 10^{-2}$
30	$8.27 \times 10^{-3}$	$1.01 \times 10^{-2}$	$8.79 \times 10^{-3}$

Table 5.2. Measured and modeled surface doses (mGy) at several source-detector distances for  $^{36}\text{Cl}$ . The surface is defined as extending to a depth of 1 mm. The mass involved is 0.1824 grams.

$^{36}\text{Cl}$			
Source-detector distance (mm)	Measured	MCNP	VARSKIN
5	$7.65 \times 10^{-2}$	$1.29 \times 10^{-1}$	$1.17 \times 10^{-1}$
10	$3.25 \times 10^{-2}$	$5.64 \times 10^{-2}$	$4.94 \times 10^{-2}$
20	$1.19 \times 10^{-2}$	$1.78 \times 10^{-2}$	$1.53 \times 10^{-2}$
30	$6.48 \times 10^{-3}$	$8.40 \times 10^{-3}$	$7.09 \times 10^{-3}$

Table 5.3. Measured and modeled surface doses (mGy) at several source-detector distances for  $^{210}\text{Bi}$ . The surface is defined as extending to a depth of 1 mm. The mass involved is 0.1824 grams.

$^{210}\text{Bi}$			
Source-detector distance (mm)	Measured	MCNP	VARSKIN
5	$9.33 \times 10^{-2}$	$1.28 \times 10^{-1}$	$9.67 \times 10^{-2}$
10	$3.75 \times 10^{-2}$	$5.23 \times 10^{-2}$	$3.94 \times 10^{-2}$
20	$1.33 \times 10^{-2}$	$1.61 \times 10^{-2}$	$1.21 \times 10^{-2}$
30	$7.39 \times 10^{-3}$	$7.52 \times 10^{-3}$	$5.62 \times 10^{-3}$



Table 5.4. Measured and modeled shallow doses (mGy) at several source-detector distances for  $^{90}\text{Sr}/^{90}\text{Y}$ . Shallow is defined as starting 1 mm below the surface and extending to a depth of 3 mm. The mass involved is 0.3647 grams.

$^{90}\text{Sr}/^{90}\text{Y}$			
Source-detector distance (mm)	Measured	MCNP	VARSKIN
5	$3.75 \times 10^{-2}$	$4.88 \times 10^{-2}$	$4.17 \times 10^{-2}$
10	$1.77 \times 10^{-2}$	$2.32 \times 10^{-2}$	$1.95 \times 10^{-2}$
20	$7.12 \times 10^{-3}$	$8.10 \times 10^{-3}$	$6.87 \times 10^{-3}$
30	$4.17 \times 10^{-3}$	$4.01 \times 10^{-3}$	$3.43 \times 10^{-3}$

Table 5.5. Measured and modeled shallow doses (mGy) at several source-detector distances for  $^{36}\text{Cl}$ . Shallow is defined as starting 1 mm below the surface and extending to a depth of 3 mm. The mass involved is 0.3647 grams.

$^{36}\text{Cl}$			
Source-detector distance (mm)	Measured	MCNP	VARSKIN
5	$1.42 \times 10^{-3}$	$3.42 \times 10^{-3}$	-
10	$7.06 \times 10^{-4}$	$1.96 \times 10^{-3}$	-
20	$2.67 \times 10^{-4}$	$7.27 \times 10^{-4}$	-
30	$1.55 \times 10^{-4}$	$3.49 \times 10^{-4}$	-

Table 5.6. Measured and modeled shallow doses (mGy) at several source-detector distances for  $^{210}\text{Bi}$ . Shallow is defined as starting 1 mm below the surface and extending to a depth of 3 mm. The mass involved is 0.3647 grams.

$^{210}\text{Bi}$			
Source-detector distance (mm)	Measured	MCNP	VARSKIN
5	$6.70 \times 10^{-4}$	$1.49 \times 10^{-3}$	$1.26 \times 10^{-3}$
10	$3.19 \times 10^{-4}$	$7.69 \times 10^{-4}$	$6.89 \times 10^{-4}$
20	$1.25 \times 10^{-4}$	$2.72 \times 10^{-4}$	$2.60 \times 10^{-4}$
30	$6.76 \times 10^{-5}$	$1.34 \times 10^{-4}$	$1.30 \times 10^{-4}$

## 5.2 Spectroscopy

Beta spectra for three radionuclides were measured using the plastic scintillator:  $^{36}\text{Cl}$  Chlorine,  $^{210}\text{Bi}$ , and  $^{90}\text{Sr}/^{90}\text{Y}$  Strontium/Yttrium. The spectra are shown in Figures 5.25 through 5.27. Theoretical spectra, drawn from the Radiation Dose Assessment Resource (RADAR), are also shown for comparison. The most important factors influencing the measurements are the losses of beta energy in the source encapsulation and air, and for  $^{210}\text{Bi}$ , backscatter from the aluminum backing. Figure 5.27 includes plots of MCNP detector response for a  $^{210}\text{Bi}$  source without an aluminum backing and with an aluminum backing. This permitted accurate scaling of the theoretical  $^{210}\text{Bi}$  spectrum, as well as illustrated the dramatic effect backscatter can have on a spectrum. Though quite thin, only  $0.9 \text{ mg/cm}^2$ , the encapsulation still has an effect, especially at lower energies. This accounts for the shift to lower energies of such features as the  $^{36}\text{Cl}$  endpoint energy and the “break” in the  $^{90}\text{Sr}/^{90}\text{Y}$  spectrum, where the  $^{90}\text{Sr}$  endpoint is reached and the spectrum becomes pure  $^{90}\text{Y}$ . Other factors that may degrade the results include the inherently poor energy resolution of plastic scintillators and energy losses in the reflective paint covering the scintillator.

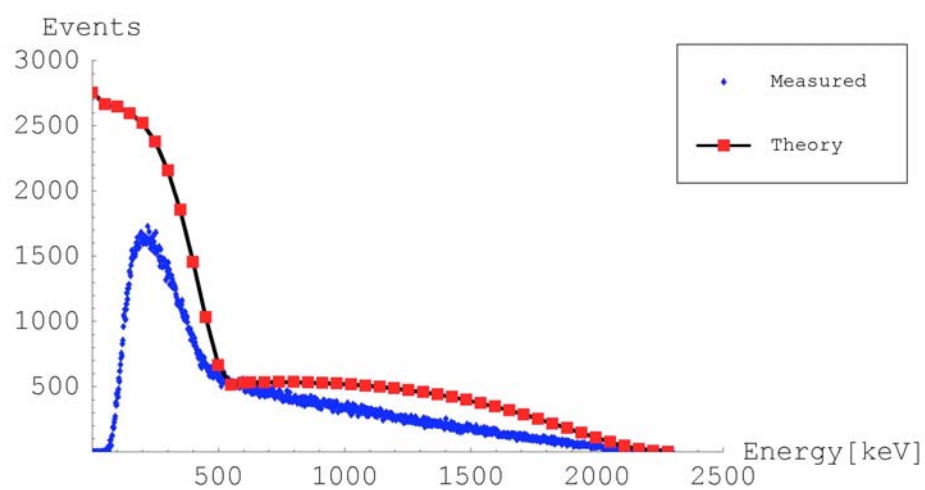


Fig. 5.25: Sr/Y-90 measured spectrum and theoretical emission spectrum.

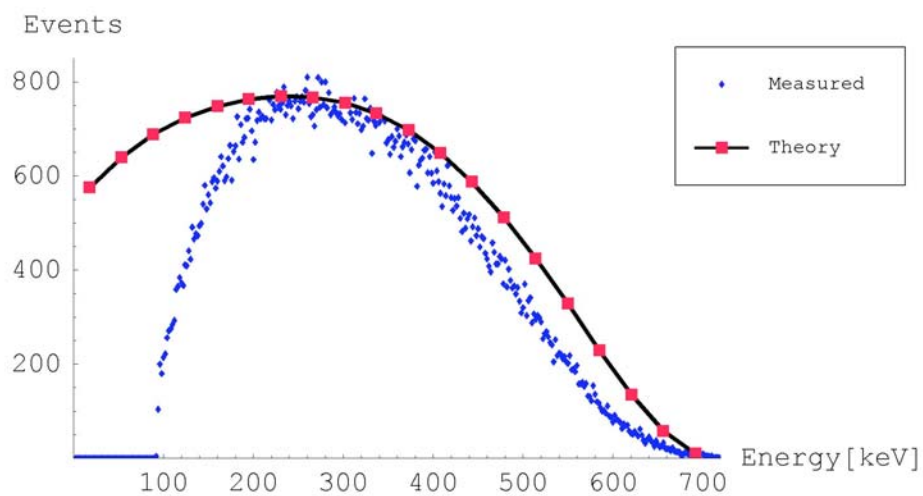


Fig. 5.26: Cl-36 measured spectrum and theoretical emission spectrum.

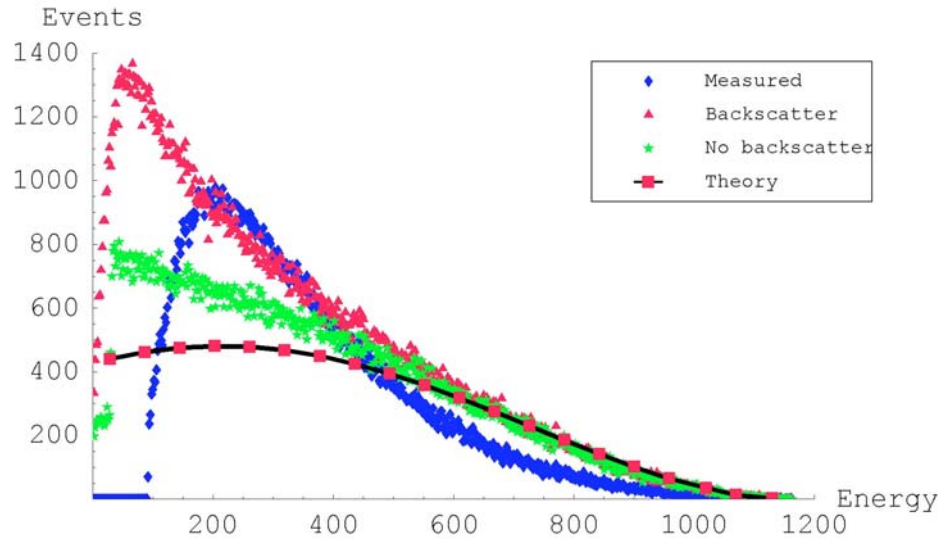


Fig. 5.27: Bi-210 measured spectrum and theoretical emission spectrum. MCNP simulated spectra illustrating the effect of backscatter are included.

In order to study the LAAPD as a beta detector in its own right, the scintillator was removed from the detector module and betas from the various sources were counted. Since the active thickness of the LAAPD is quite small, about 15  $\mu\text{m}$ , most of the betas simply passed through it, leaving some energy behind. The result was that every nuclide examined had the same endpoint on the MCA, though lower energy nuclides such as  $^{99}\text{Tc}$  and  $^{14}\text{C}$  retained some of their characteristic spectral shapes (Figs. 5.28 and 5.29). It appears that the LAAPD by itself can function as a simple counter, but its usefulness as a spectroscopy tool is limited to very low energy beta emitters.

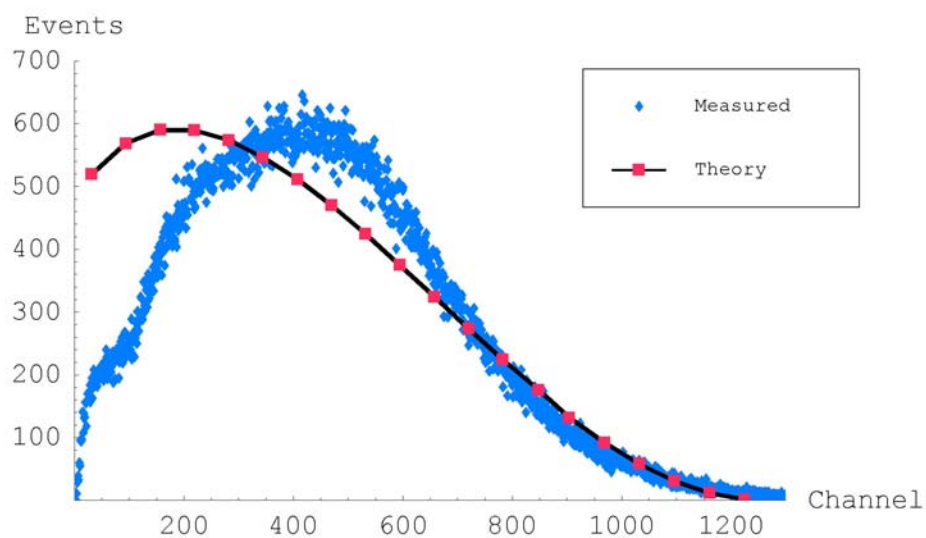


Fig. 5.28: Carbon-14 spectrum recorded by direct interaction in the LAAPD. Shape is similar to theoretical emission spectrum.

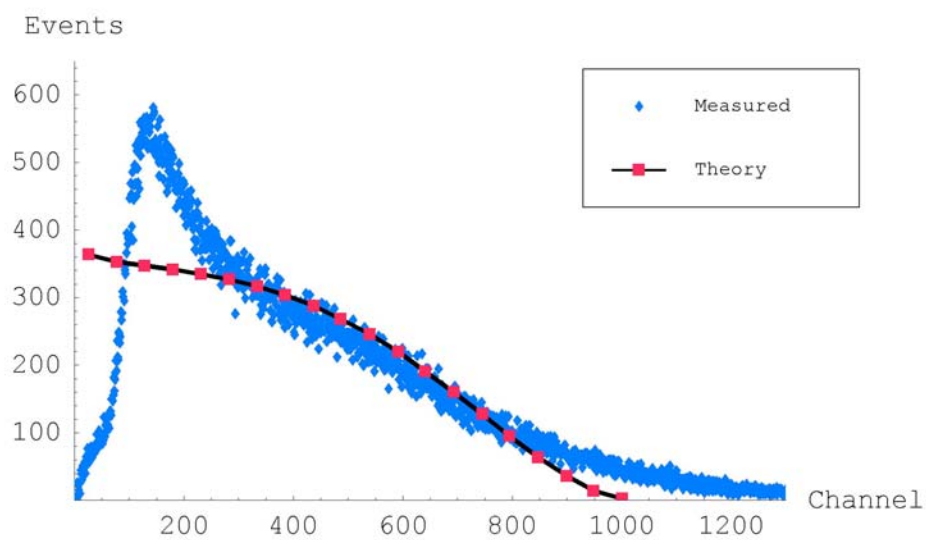


Fig. 5.29: Technetium-99 spectrum recorded by direct interaction in the LAAPD. Shape is similar to theoretical emission spectrum.

### 5.3 Spectral enhancement

The effect of the spectral enhancement algorithm on the simulated MCNP detector spectra is shown in Figs. 5.30 – 5.32. The simulated detector response spectrum (“Detector”), the spectrum after processing with the algorithm (“Processed”), and the theoretical emission spectrum (“Theory”) are all plotted on the same axis. For the case of  $^{14}\text{C}$ , a low-energy emitter, there was very little AI effect, so very little adjustment was needed (Fig. 5.30). Chlorine-36, a higher-energy emitter, demonstrated more AI effect (Fig. 5.31), and  $^{90}\text{Y}$ , a high-energy emitter, was greatly affected (Fig. 5.32). Clearly, the higher the energy, the greater the presence of the AI effect. This is attributed primarily to the increased number of edge-effect events as energy increases.

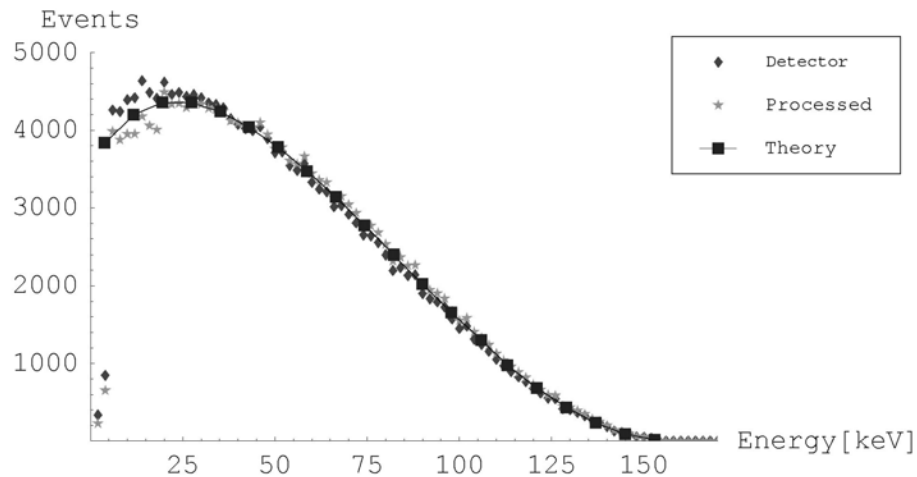


Fig. 5.30: Carbon-14 spectrum, before and after processing, compared to theoretical emission spectrum.

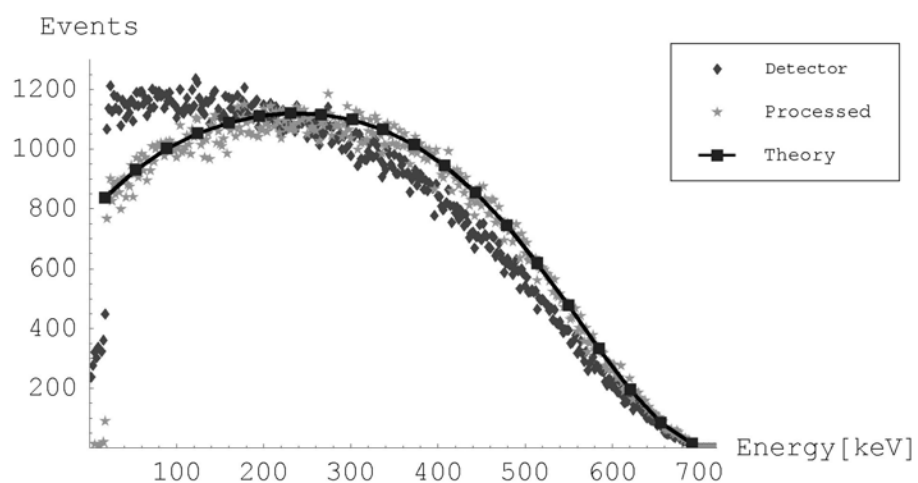


Fig. 5.31: Chlorine-36 spectrum, before and after processing, compared to theoretical emission spectrum.

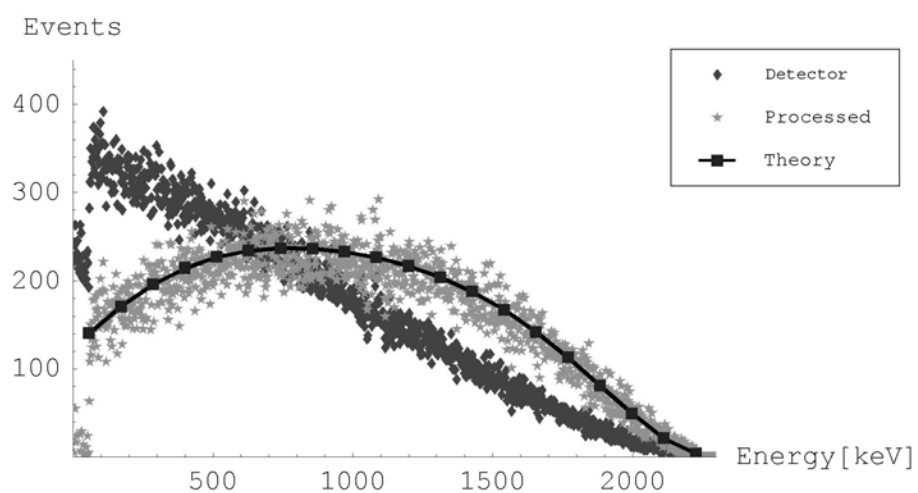


Fig. 5.32: Yttrium-90 spectrum, before and after processing, compared to theoretical emission spectrum.

The algorithm was applied to a measured  $^{90}\text{Sr}/^{90}\text{Y}$  spectrum (Fig. 5.33). The portion of the measured spectrum above the strontium cutoff (546 keV) is nearly a straight line, as it is in the MCNP- generated case as well. At lower energies, the detector suffers from pulse-processing inefficiencies unrelated to the AI effect, so only the  $^{90}\text{Y}$  portion of the measured spectrum is of interest. The algorithm clearly reshapes the measured spectrum, in the energy domain above 546 keV, so as to approach the theoretical energy emission spectrum of  $^{90}\text{Y}$ .

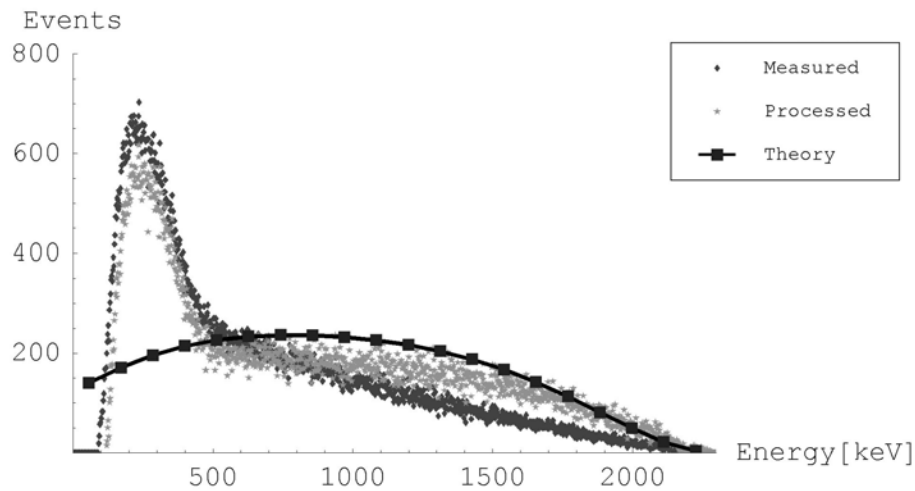


Fig. 5.33: Application of the algorithm to a measured  $^{90}\text{Sr}/^{90}\text{Y}$  spectrum. Only the  $^{90}\text{Y}$  component of the theoretical emission spectrum is shown.



## 6 DISCUSSION

### ***6.1 Factors affecting the results***

Every measured signal is affected to some extent by factors that can be more or less accounted for, and which fall under the general term *noise*. Noise can be divided into two general categories: that generated by background radiation or other unwanted scintillation events, and that generated by the pulse processing electronics, including the LAAPD.

#### **6.1.1 Background radiation**

Background radiation is omnipresent in any laboratory. Though a detector may be shielded from unwanted radiation sources present in the lab, it is difficult to shield against cosmic radiation. There may also be some low-level radioactivity in the shielding. In order to lower the background as much as possible, the scintillator and LAAPD were placed within a lead brick enclosure, closed on all sides but open on top and bottom. This was sufficient to screen most radiation from other laboratory sources, but did not impact cosmic rays or any radiation originating in the earth. As a result, there was always some background present. However, over a typical one-hour count, the background due to unwanted radiation proved to be of little account. In part this was due to the other laboratory sources being enclosed in lead, and in part due to the small cross section presented by the scintillator and LAAPD.

### 6.1.2 Cerenkov radiation

Another source of unwanted scintillation light is Cerenkov radiation. Cerenkov radiation is produced when a relativistic electron passes through a material with an index of refraction high enough such that the speed of the electron exceeds the speed of light in that material. Cerenkov radiation has a bluish color, so the LAAPD will respond to it. However, since the scintillator is a double wave-shifting type, it is expected that most Cerenkov radiation produced in the scintillator will be shifted to a higher wavelength before striking the LAAPD. In order to observe if Cerenkov radiation is noticeably present, a non-scintillating piece of lucite, of the same dimensions as the scintillators, was affixed to the LAAPD. A count was taken for one hour with the inert lucite exposed to  $^{90}\text{Sr}/^{90}\text{Y}$ , the beta emitter of highest available energy. When compared to a background count taken with the same inert plastic, no significant difference was observed. It was concluded that Cerenkov radiation, though undoubtedly present, was in too small a quantity to have a substantial impact on the experimental measurements.

### 6.1.3 Direct LAAPD interactions

The LAAPD is sensitive to both charged particles and to x and gamma radiation. It is very thin, so it presents a small cross section to electromagnetic radiation, particularly at high energies. However, direct exposure to a  $^{133}\text{Ba}$  source, a copious gamma and characteristic x-ray emitter, revealed that a significant number of x-ray

and gamma interactions will occur. The beta sources used for this research were by and large pure beta emitters, so the only real concern regarding electromagnetic interactions directly in the LAAPD, aside from background, was the possible effect of bremsstrahlung radiation on the measurements. Bremsstrahlung radiation is produced when inelastic radiative collisions occur between charged particles and the nuclei of the material they are traversing. The cross section for this to happen is proportional to the square of the atomic number of the medium. Because the medium in this case was composed entirely of low-Z elements, the amount of bremsstrahlung radiation produced was expected to be small. Furthermore, most of the bremsstrahlung x-rays would likely miss the LAAPD altogether. Since the measurement taken for the Cerenkov question would also have indicated the presence of excess counts if bremsstrahlung x-rays had been counted, and there were no excess counts, it was concluded that bremsstrahlung radiation was not present in significant enough quantities to require special handling.

Finally, in regard to excess counts due to unwanted radiation, there was the question of beta particles penetrating the scintillator and expending energy directly in the LAAPD. Again, using the inert lucite in place of the scintillator proved that the scintillator thickness was adequate to absorb all betas incident on it, up to the maximum energy studied, 2.281 MeV. If betas had penetrated the lucite, they would have produced a noticeable spectral pattern.

#### **6.1.4 Handling background, Cerenkov, and direct interactions**

The experiments utilizing the inert plastic piece all indicated the absence of Cerenkov, bremsstrahlung, and direct beta effects. However, if any one of those had proved significant, it would have required a means of determining which one. To eliminate the influence of direct beta effects, for example, the source could have been oriented to the detector such that the betas struck it at right angles, rather than head on. To eliminate Cerenkov effects, a thin piece of opaque material could have been interposed between the lucite dummy scintillator and the LAAPD face, thus blocking all light. Coupled with the change of source-detector orientation, only bremsstrahlung radiation would have been detected, if any were present. As it turned out, none of these remedies were necessary.

#### **6.1.5 Instrumentation noise**

The second source of noise, instrumentation noise, was far more influential than unwanted radiative noise. Avalanche photodiodes, especially those with large diameters such as the one used in this work, produce large quantities of low-energy noise. For this particular LAAPD module, the low-energy noise precluded any measurements below 100 keV. To eliminate this noise from measured data, the discriminator on the stretcher module, as well as the lower-level discriminator on the single channel analyzer, were adjusted to the necessary level. In practice this meant that certain interesting beta emitters, such as  $^{14}\text{C}$  and  $^{99}\text{Tc}$ , could not be measured with the desired detail, because of their low-energy endpoints. Much of their spectra were lost in

the energy region below the cutoff point. Instrumentation noise from NIM bin modules did not have any noticeable impact.

By far the most significant problem in gathering data was the inefficiency of the NIM equipment in processing the LAAPD module signals. The signal from the LAAPD module was too fast and narrow for the NIM modules, especially the delay-line amplifier, to handle properly. The misshapen signal from the unipolar output of the delay-line amplifier was enough to make this clear. The solution found to enable this signal to be of any use, namely the application of the stretcher, was only partially successful. Signals due to beta particles of energies between the lower-energy noise cutoff and maximum energy were often not processed, a situation best seen by examination of the  $^{90}\text{Sr}/^{90}\text{Y}$  measured and MCNP spectra. Not surprisingly, since small signals are proportionally more affected by outside influences than large signals, the problem showed up more as the energy decreased. Naturally, both spectroscopy and dosimetry results were affected. Tables 6.1 and 6.2 illustrate the energy dependence of the efficiency, which is defined as the MCNP value divided by the corresponding measured value, for the  $^{90}\text{Sr}/^{90}\text{Y}$  and  $^{36}\text{Cl}$  spectra. Efficiency values were calculated at 100 keV energy intervals.

Below the noise cutoff level, the efficiency is low to nonexistent. From there it rises, reaching a value of about 0.8 for  $^{90}\text{Y}$ , and a less impressive value of about 0.7 for  $^{36}\text{Cl}$ . The end of the range has an efficiency greater than 1; this is a result of background counts adding to the measured total and an artifact of the MCNP energy input ranges, which do not extend all the way to the maximum possible beta energy. There

is also greater statistical uncertainty at the end of the energy range, where betas are fewer than at lower energies. The overall efficiency, that is, the total measured counts divided by the total MCNP counts, is 48% for both  $^{90}\text{Sr}/^{90}\text{Y}$  and  $^{36}\text{Cl}$ . These values, coupled with the energy-range tabulated efficiencies, demonstrate that most of the counts lost were from low-energy betas.

Table 6.1. Efficiency calculated as a function of energy range for  $^{90}\text{Sr}/^{90}\text{Y}$ .

Energy Range (keV)	Measured counts	MCNP counts	Efficiency
0 – 100	171	69097	0.002475
100 – 200	19741	70875	0.278533
200 – 300	31417	57443	0.546925
300 – 400	23552	42205	0.558038
400 – 500	14682	24228	0.605993
500 – 600	11745	14202	0.826996
600 – 700	10608	12862	0.824755
700 – 800	9586	11805	0.812029
800 – 900	8574	10863	0.789285
1000 – 1100	7686	9985	0.769755
1100 – 1200	6966	8941	0.779107
1200 – 1300	6181	7815	0.790915
1300 – 1400	5485	7077	0.775046
1400 – 1500	4787	6004	0.797302
1500 – 1600	4091	5078	0.805632
1600 – 1700	3570	4260	0.838028
1700 – 1800	2870	3418	0.839672
1800 – 1900	2373	2564	0.925507
1900 – 2000	1754	1834	0.956379
2000 – 2100	1240	1218	1.018062
2100 – 2200	816	666	1.225225
2200 – 2300	328	250	1.312

Table 6.2. Efficiency calculated as a function of energy range for  $^{36}\text{Cl}$ .

Energy Range (keV)	Measured counts	MCNP counts	Efficiency
0 – 100	0	0	N/A
100 – 200	26345	62833	0.419286
200 – 300	37394	55643	0.672034
300 – 400	34221	47877	0.714769
400 – 500	23433	35423	0.661519
500 – 600	10066	18677	0.538952
600 – 700	1696	4312	0.393321
700 – 800	24	1	24

## 6.2 Dosimetry

Using the dose values in Tables 5.1 through 5.6, dose efficiency values, defined as measured doses divided by MCNP doses, were calculated for the surface and shallow cases, at each source-detector distance. The results are plotted in Figs. 6.1 and 6.2. From Fig. 6.1, the surface case, the efficiencies for  $^{90}\text{Sr}/^{90}\text{Y}$  and  $^{36}\text{Cl}$  are nearly equal for each source-detector distance; the values for  $^{210}\text{Bi}$  are somewhat higher. There is also a linear relationship between efficiency and distance from 10 mm to 30 mm. This linearity, paired with the proximity of the curves, suggests that for the surface case, a single, nuclide-independent dose correction factor exists that can predict a dose value, at least within the source-detector distances examined. Of course, the correction factor used is strongly dependent on the source-detector distance, and will not apply to low-energy emitters. The fact that the  $^{210}\text{Bi}$  efficiencies are higher than the others may be an artifact of that source's differing physical structure, which produces considerable backscatter from the source's aluminum backing.

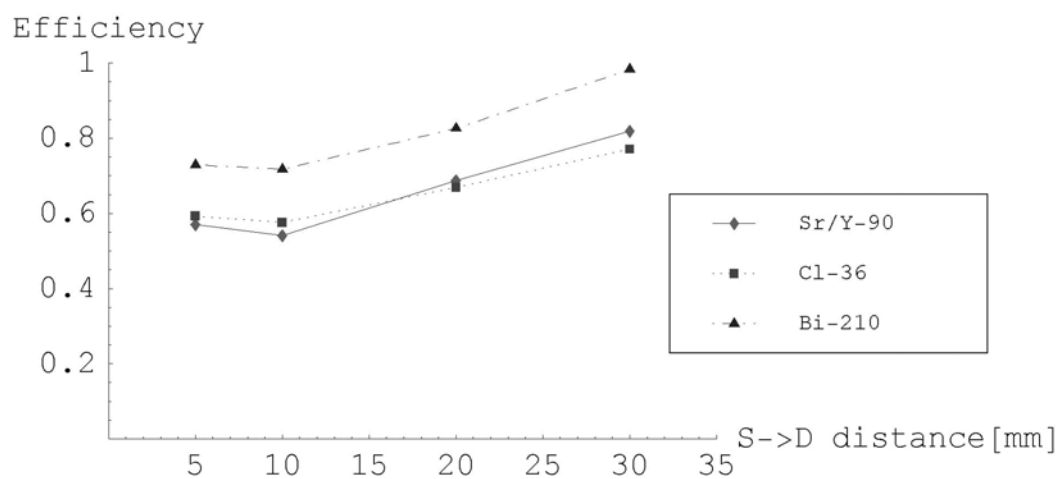


Fig. 6.1: Surface dose efficiencies. Efficiency is defined as measured dose divided by MCNP dose.

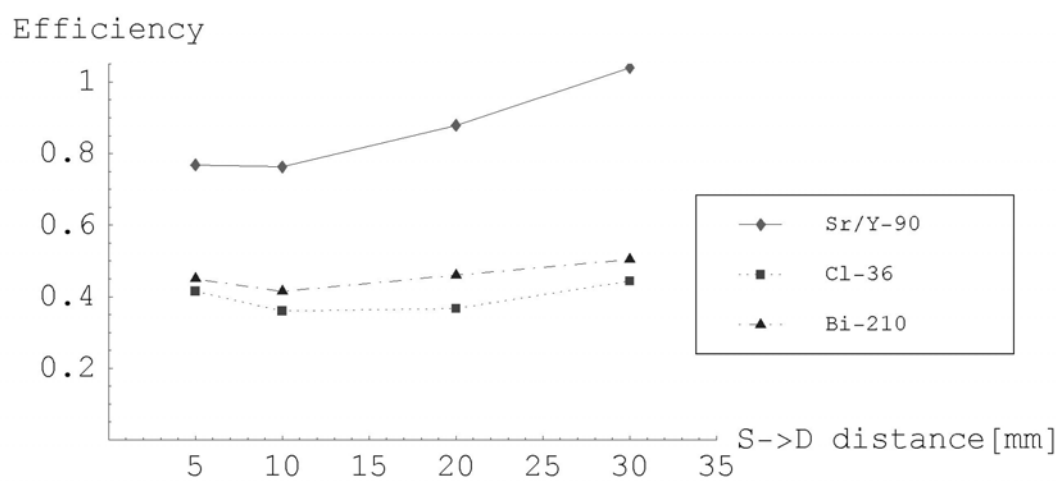


Fig. 6.2: Shallow dose efficiencies. Efficiency is defined as measured dose divided by MCNP dose.



The shallow efficiency curves (Fig. 6.2) do not have the same nuclide-independent features, probably because the  $^{36}\text{Cl}$  and  $^{210}\text{Bi}$  emission spectra lack the high energies needed to deposit as significant a quantity of energy in the scintillator as the  $^{90}\text{Sr}/^{90}\text{Y}$ . The  $^{210}\text{Bi}$  does not exhibit the same behavior as in the surface case, since the backscatter betas are mostly absorbed in the outer, inert layer of the shallow scintillator. As in the surface case, the curve shapes imply that a linear relationship exists between efficiency and source-detector distance. This is particularly noticeable for  $^{90}\text{Sr}/^{90}\text{Y}$ . For beta emitters of comparable endpoint energy there likely exists a single shallow dose correction factor that is nuclide-independent, for each source-detector distance. Bismuth-210 and  $^{36}\text{Cl}$  are similar, for example; another beta emitter with high endpoint energy will likely have efficiencies that lie near those of  $^{90}\text{Y}$ .

Extrapolation of the efficiency-distance line beyond 30 mm quickly results in the efficiency exceeding unity. Therefore, a better interpretation of the efficiency data would propose that as the source-detector distance increases, the efficiency should asymptotically approach a constant value of 1, and the apparent linearity of the data applies only to small source-detector distances. Background events were subtracted from the measured data before doses were calculated, but since the background varies over the course of the day, and possibly from measurement to measurement, there may be some background events that were not subtracted, that contributed to the dose calculation. Such a scenario might explain the efficiency values that exceed unity. Alternatively, small geometric errors between measured and modeled configurations may also result in this anomaly.

The large discrepancies between the measured and modeled results can be attributed to the detector efficiency, especially at low energies. The efficiencies are energy dependent: the lower the energy, the lower the efficiency. MCNP has the advantage of being able to count each and every event, no matter how low its energy, hence the low-energy “humps” found in the MCNP dose simulations are not found in the measured cases. In the case of this detector, thermal noise from the LAAPD prohibits accurate measurement below about 100 keV, so such low-energy features cannot be recorded.

As expected, dose decreases as the source-detector distance increases, for the same measurement time. However, the dose efficiency, as defined above, is not constant. As source-detector distance increases, the efficiency increases significantly, as seen in Figs. 6.1 and 6.2. There are several factors at work. First, since the greater part of the dose difference between measurement and model is attributable to the detector’s low efficiency at low energies, and a larger air gap will preferentially remove low-energy betas from the stream, the proportion of events occurring in the detector from higher energy betas will increase, which will act to close the dose gap somewhat. Second, there is a strong effect on the spectrum with regard to the angles of incidence of the betas on the detector surface (the AI effect, described in section 4.10). At closer distances, a higher proportion of betas will strike the detector at greater angles to the normal, increasing the chance that the beta will glance off the detector, leaving behind only a fraction of its full energy. The MCNP model will record all these low energy fractional events (evidenced by the aforementioned low-energy “humps” in the surface

cases), but the detector will miss many or all of them, thus decreasing the measured dose. But as the source-detector distance is increased, the angle of incidence to the normal decreases, thus lessening the number of low-energy fractional depositions, and increasing the number of events that can be measured. This decreases the dose difference between the measured and MCNP cases.

If the dose is measured and calculated only for events that fall above a certain energy threshold, the differences between measurement and model become very small. For example, above a threshold of 545 keV, the surface dose for  $^{90}\text{Sr}/^{90}\text{Y}$  at 10 mm source-detector distance is  $3.64 \times 10^{-3}$  mGy measured, and  $3.96 \times 10^{-3}$  mGy modeled with MCNP. This represents a percent difference of only -8.1%.

Accurate beta dosimetry is a tricky subject. To calculate dose there has to be a defined volume of mass, but it is a non-trivial matter to calculate how a beta particle will distribute its energy in that given volume. By necessity, any calculated beta dose represents an average energy deposition in some volume. An average dose value may understate the effect of an exposure to betas. Low-energy emitters, such as  $^{36}\text{Cl}$  and  $^{99}\text{Tc}$ , may deposit much of their beta energy in a thin layer that represents only a fraction of the mass used in the dose calculation. This is certainly the case for  $^{36}\text{Cl}$  in the shallow dosimeter. Using thinner and thinner layers will improve the results, but may be impractical from a technical standpoint.

In general, since the 1 mm thick inert plastic layer covering the shallow dose scintillator corresponds approximately to the CSDA range of a 0.4 MeV beta, there is little point in attempting to measure shallow dose for beta emitters of lower maximum

energy with this instrument, since only a fraction, or none, of the scintillator mass is involved. In practical terms, the useful shallow dose energy range is higher, since betas seldom travel their full CSDA range. The results for  $^{36}\text{Cl}$  reflect this situation. As a rule of thumb, surface dose measurements are limited to beta emitters of maximum energy of about 0.3 MeV and higher, due to the low-energy detector deficiencies, and shallow dose measurements are practical for beta emitters with maximum energy greater than that of  $^{36}\text{Cl}$ . Better results will be seen for lower-energy emitters if the shallow layer is made only 1 mm thick, thus reducing the mass over which the energy deposition is averaged.

### ***6.3 Spectroscopy***

Much of the analysis that applied to the dosimetry results also applies to the spectroscopy results. The only difference is the intent behind the measurement; dosimetry is for measuring effect, whereas spectroscopy is for identification. To the extent that this detector is an effective spectroscopic tool, it must be able to identify beta emitters with a minimum of ambiguity.

Beta emitters are identified by the shape of the spectra and the maximum (end-point) beta energy. For certain beta emitters, for example  $^{90}\text{Sr}/^{90}\text{Y}$ , the shape is so distinctive as to make it easy to identify. Many beta emitters have similar shapes, however. Furthermore, if the beta source is encapsulated or has a thick backing, the measured spectral shape may be considerably altered from the theoretical spectral

shape; such is the case with the  $^{210}\text{Bi}$  source examined in this research. Therefore, endpoint energy becomes important in identifying beta emitters.

Endpoint energy is also subject to the influence of encapsulation and the presence of air, or other intervening material that may lie between the source and the detector. If the encapsulation is thin, and the source-detector distance small, the effect on the endpoint energy will be small, provided the energy is large enough so that a few keV lost does not amount to a significant percentage of the total. Such is clearly the case with  $^{90}\text{Sr}/^{90}\text{Y}$ ; the 2,281 keV endpoint energy is barely affected by the thin mylar encapsulation or the small air gap. The effect grows larger as the energy decreases. Table 6.3 indicates the increase in energy lost from a beta emitted with maximum energy, for a number of different radionuclides, as the endpoint energy decreases. In all cases it was assumed that the beta travels in a straight line, normal to the detector face, through 0.9 mg cm<sup>-2</sup> of mylar encapsulation and 10 mm of air.

Table 6.3. Endpoint energy losses through mylar encapsulation and air for several radionuclides.

Nuclide	Maximum energy (MeV)	Energy loss (MeV)	Percent of maximum energy
$^{90}\text{Y}$	2.281	3.63E-03	1.59E-01
$^{36}\text{Cl}$	0.709	3.67E-03	5.17E-01
$^{99}\text{Tc}$	0.292	4.55E-03	1.56E+00
$^{14}\text{C}$	0.156	6.05E-03	3.88E+00

The results of Table 6.3 are a first order calculation only, that is, only an initial value of the stopping power at the maximum energy was used for mylar and air. Because of the nature of the variation of stopping power with energy, a more accurate

CSDA calculation would emphasize the differences between high and low energy emitters. Therefore, the result for  $^{90}\text{Y}$  is a slight overestimation of the energy lost, whereas the values for the other elements are underestimated. Also, since electrons do not follow perfectly straight lines except under unique circumstances, the total path traveled, and energy lost on the way, will be higher.

Though the effect on the measured data of encapsulation and air is noticeable, it is not easily quantified. First, the effect is not large. For nuclides where the effect might be more noticeable, such as  $^{14}\text{C}$ , the endpoint energy was too low for effective measurement, given the detector's trouble handling low-energy pulses. Second, the subjective determination of endpoint energy heightens the uncertainty. Since beta spectra tend to trail off gradually toward the maximum energy, and there is always some background present around that energy, the endpoint cannot be determined to better than 2 or 4 keV of the actual maximum point. It is necessary to recognize that two beta emitters with roughly the same shape and nearly the same endpoint energy may be indistinguishable with this detector. Fortunately, the beta emitters commonly found in the lab or workplace are usually quite distinct, and often it is enough to know the maximum energy of emission, rather than the identity of the emitter, to determine if a hazard exists.

#### ***6.4 Spectral enhancement***

The excellent results achieved when the spectral filtering algorithm was applied to the Monte Carlo simulated data are not surprising. Once the phenomenon of

partial energy deposition had been understood and its origins detected, and an algorithm had been developed to remove the effects, applying that algorithm to “canned” data did not constitute conclusive proof that the algorithm was practical for actual, measured data. For the Monte Carlo simulations, applying the algorithm returned us to the original MCNP input energy distribution. The principle was proven, but not the usefulness of its implementation.

There are a number of issues related to applying the algorithm to measured data. The kernels calculated for the FED removal process were created under very specific conditions: no source encapsulation, and no air between the source and the detector. Measured data includes both. Furthermore, the detector’s difficulty in handling low-energy pulses has been noted. The measured spectrum therefore reflects the influence of events not related to the FED effect. It is not expected that an algorithm designed to ameliorate one problem will be able to ameliorate another, unrelated problem. Nevertheless, it was of great interest to see what, if any effect the algorithm would have on a measured spectrum. It was expected that there would be some positive benefit, even if the processed spectrum remained somewhat deficient. Indeed, this was the case.

The example of Fig. 5.34 indicates that the algorithm, when applied to data measured with this detector, will have a beneficial effect at higher energies. It becomes probable, therefore, that if the detector can be modified in ways that allow it to fully process all events that occur in it, regardless of energy, then the algorithm will significantly enhance any measured spectrum. However, even if the detector can re-

cord all events that occur, the influence of source encapsulation and air will require further processing to fully enhance the spectrum.

Encapsulation has two effects: It causes the betas to lose energy as they pass through it, and it serves as a source of secondary, or “knock-on”, electrons. The air has a similar, if less pronounced effect. Of the two effects, the production of knock-on electrons is the more important. As shown earlier, the mylar and air have a noticeable, but reasonably minor, effect on the beta energy, particularly at higher energies. A knock-on electron, however, may have up to half the energy of the beta that produced it. This causes a build up of events in the lower energy range of the spectrum. Though these events are not prominent in the measurements, due to the detector’s low-energy cutoff, they are distinct in the MCNP simulations. Figure 6.3 illustrates a  $^{36}\text{Cl}$  spectrum with mylar encapsulation and air, compared to one without either.

Removal of the low-energy knock-on events is not as straightforward as the removal of partial-energy deposition events. Figure 6.4 illustrates the result of applying the no-encapsulation/no-air kernels to a  $^{90}\text{Sr}/^{90}\text{Y}$  MCNP spectrum that includes encapsulation and air. The effect is positive at the higher energies, but only partially accounts for the build up of low-energy events.

Calculating kernels that include the effects of encapsulation and air, in an effort to deal with the remaining low-energy events, is troublesome. For one thing, every beta loses some energy on its way to the detector. This means there is a distribution of energies corresponding to events that would be considered primary energies (full deposition events), rather than a single channel containing primary energies. There-



fore, it is not so simple a matter to determine how many betas deposited their full energy in the detector. Inevitably, there will be increased uncertainty in the number of primary events, especially at lower energies.

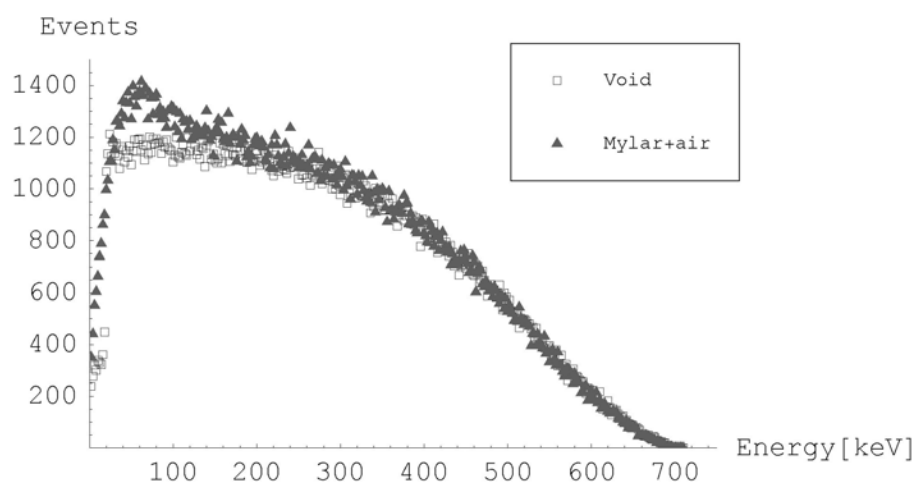


Fig. 6.3: Chlorine-36 spectrum showing the influence of mylar encapsulation and air on the MCNP modeled spectrum.

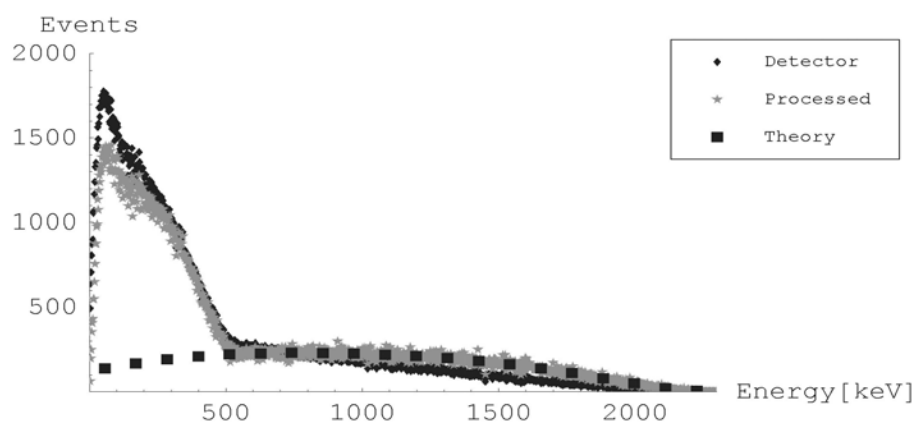


Fig. 6.4: Effect of processing a Strontium/Yttrium-90 spectrum that included the effects of mylar encapsulation and air.

Another possibility is to hypothesize that the remaining low-energy events, after the no-encapsulation/no-air kernels have been applied, are strictly due to knock-on electron events. Using the dictum that a knock-on electron can have an energy no greater than half that of the electron that hit it, one can hypothesize a distribution of knock-on electrons that has an energy range from 0 to  $E_{\text{max}}/2$  keV, where  $E_{\text{max}}$  is the maximum beta energy. Provided an estimate or calculation of the number of knock-on electrons can be made, the events they produced can be subtracted from the spectrum according to the hypothesized distribution. Such an effort is left to future work.

## 7 CONCLUSIONS

A beta detector has been designed and built that utilizes plastic scintillators and a large-area avalanche photodiode to perform beta dosimetry and spectroscopy. The dosimetry results, based on comparisons to Monte Carlo simulations, indicate that the detector is capable of determining dose to a high degree of accuracy for point sources, provided the beta emitters are of high energy. Low-energy sources are recorded less accurately, due to partial-volume energy deposition and insensitivity of the detector to low-energy pulses. Since low-energy external betas pose less of a health hazard than high-energy betas, being largely absorbed in clothing or the dead layer of the skin, the shortcomings with respect to low-energy insensitivity are not as severe as the data might indicate. The spectroscopy results indicate that this detector is capable of recording a variety of beta spectra over a wide range of energies, subject to the need to maintain a low-energy cutoff to prevent excessive noise. A technique has been developed that enhances beta spectra by removing partial-energy deposition events, which cause spectral distortion.

The need for instrumentation that can readily detect, identify and quantify radioactive materials is becoming increasingly urgent. Efforts are ongoing to permit detection and tracking of radioactive material in transit and in situ, before it can be used in a criminal manner. However, there is always the possibility that radioactive material may evade screening and be utilized for destructive purposes, perhaps as a “dirty bomb”. In that case there will be a need for instrumentation that can quantify effects of such a case. The health physics profession is uniquely qualified to play the leading

role in developing such instruments. As a contribution to that vital role, the instrument described in this thesis was developed. Its purpose is the detection, identification and quantification of beta radiation. Since beta radiation is an important component of many radioactive decay processes, and may pose a considerable health hazard, it must be accounted for along with the other modalities. Detectors devoted to measuring beta dose and identifying beta emitters are less common than those that detect radiation modalities considered to be more hazardous due to their penetrating capabilities, such as gammas and neutrons. The development of this scintillator and LAAPD-based beta detector contributes in a small way to filling a gap in critical health physics instrumentation.

There are several factors affecting the performance of the detector described herein. The primary factor affecting both spectroscopic and dosimetric results is the difficulty the NIM instrumentation has in processing the fast signal from the LAAPD module. If instrumentation is used that can properly process the LAAPD signal, then the overall response at low energies should improve significantly. The LAAPD module is promising as a detector tool. Though it suffered some breakdowns related to the high-voltage compensation circuit, once these were fixed it proved reliable over long periods of use.

Another factor of significance, related to the dosimetry results, is the partial-volume effect, whereby low-energy emitters deposit their energy fully within only the leading portion of the scintillator volume. This causes an underestimation of the dose because the entire scintillator mass is used in the dose calculation. The best solution to

this problem is to reduce the thickness of each scintillator layer, so that the mass involved is irradiated across its full depth.

In addition to the aforementioned factors, another major improvement to the detector would involve reducing the noise from the photodiode. This can best be accomplished by cooling the LAAPD, likely by using a thermoelectric unit. The literature has examples of LAAPDs that were able to record low-energy characteristic X-ray events directly in the silicon, provided the temperature was low enough. To achieve even better response, liquid nitrogen cooling could be done, though this would require some careful engineering to ensure the integrity of the LAAPD module.

Liberal use of Monte Carlo N-particle code has been used throughout this research to provide points of comparison and to explore the interactions of betas with material under a variety of circumstances. In the future, it makes sense to model any proposed detector with MCNP prior to building it. This will bring to light any factors that might require a revision of the design. For example, the presence of knock-on electrons at low energies, due to encapsulation and air, might suggest designing a detector that can operate in vacuum with unencapsulated sources. Or, the significant spectral distortion caused by the edge effect might suggest the use of a scintillator of broad diameter, coned down to a narrower central portion that can eliminate most edge events.

Future research related to this detector may follow several paths. The first path would involve solving the technical issues discussed above, namely the introduction of more suitable pulse-processing instrumentation and the reduction of noise by cooling,

as well as refinement of the AFED event removal algorithm to account for knock-on electrons and the effects of encapsulation. The second path may involve development of the detector as a field-ready instrument. The LAAPD module, and the scintillators that can be attached to it, can be formed into a small, portable-sized detector. Given a suitable power source, such as a rechargeable battery pack, a meter or small display, and some off-the-shelf electronics, it is easy to visualize this detector as a hand-held instrument in the field, capable of simultaneously identifying beta emitters and measuring beta dose. Since most beta emitters are likely to be accompanied by gamma emitters, a means of filtering out unwanted Compton events must also be developed. The edge-effect processing algorithm can be included as firmware. Finally, the LAAPD module need not be restricted to beta measurements; with denser scintillators it can also be adapted for gamma spectroscopy and dosimetry.

## BIBLIOGRAPHY

Advanced Photonix, Inc. 1991. Noise characteristics of Advanced Photonix avalanche photodiodes. Company document.

Allday A. 2002. AttenCHE.exe.  
<http://www.staff.city.ac.uk/~micfar/s'waredownloads.htm>.

Allier CP, van Loef EVD, Dorenbos P, Hollander RW, van Eijk CWE, Krämer KW, Güdel H. 2002. Readout of a LaCl<sub>3</sub>(Ce<sup>3+</sup>) scintillation crystal with a large area avalanche photodiode. Nucl. Inst. and Meth. A485: 547-550.

Attix FH. 1986. Introduction to Radiological Physics and Radiation Dosimetry. New York: J Wiley & Sons. 607 p.

Bambynek M, Flühs D, Quast U, Wegener D, Soares CG. 2000. A high-precision, high-resolution and fast dosimetry system for beta sources applied in cardiovascular brachytherapy. Med. Phys. 27(4): 662-667.

Baron AQR, Ruby SL. 1994. Time resolved detection of X-rays using large area avalanche photodiodes. Nucl. Inst. and Meth. A343: 517-526.

Baranov VA, Filchenkov VV, Konin AD, Zhuk VV. 1996. A study of the characteristics of scintillation detectors with a diffuse reflector. Nucl. Inst. and Meth. A374: 335-340.

Bea J, Gadea A, Garcia-Raffi LM, Rico J, Rubio B, Tain JL. 1994. Simulation of light collection in scintillators with rough surfaces. Nucl. Inst. and Meth. A350: 184-191.

Beddar AS, Mackie TR, Attix FH. 1992a. Water-equivalent plastic scintillation detectors for high-energy beam dosimetry: I. Physical characteristics and theoretical considerations. Phys. Med. Biol. 37(10): 1883-1900.

Beddar AS, Mackie TR, Attix FH. 1992b. Water-equivalent plastic scintillation detectors for high-energy beam dosimetry: II. Properties and measurements. Phys. Med. Biol. 37(10): 1901-1913.

Belogurov S, Bressi G, Carugno G, Moszynski M, Czarnacki W, Kapusta M, Szawłowski M. 2003. Characterization of Yb:YAG and Yb:YAP scintillators by means of LAAPD at temperature around 100 K. Nucl. Inst. and Meth. A496: 385-389.

Berger MJ. Beta-ray dose in tissue-equivalent material immersed in a radioactive cloud. Health Phys. 26(Jan.): 1-12; 1974.

Bingo K. 1977. Absorbed dose rate meter for beta-rays. Proceedings of the International Radiation Protection Association. No. 119: 131-134.

Bingo K, Suga S, Kajimoto Y, Numakunai T. 1980. Beta-ray survey meter for measuring absorbed dose rate independently of beta-ray energy. Health Phys. 39(July): 21-28.

Briesmeister JF (ed). 2000. A general Monte Carlo N-particle transport code, Version 4C. Report LA-13709-M (Los Alamos National Laboratory).

Brown GI. 2002. Invisible Rays: A History of Radioactivity. Phoenix Mill: Sutton Publishing Limited. 248 p.

Bush-Goddard SP. 2000. Beta Spectroscopy using Deconvolution and Spectral Stripping Techniques with a Triple Layer Phoswich Detector [dissertation]. Ann Arbor (MI): University of Michigan. 173 p.

Cember H. 1992. Introduction to Health Physics (2<sup>nd</sup>). New York: McGraw-Hill. 519 p.

Clift MA, Sutton RA, Webb DV. 2000. Water equivalence of plastic organic scintillators in megavoltage radiotherapy bremsstrahlung beams. Phys. Med. Biol. 45: 1885-1895.

Cottingham WN, Greenwood DA. 1986. An Introduction to Nuclear Physics. Cambridge: Cambridge University Press. 212 p.

Cross WG. 1997. Empirical expressions for beta ray point source dose distributions. Radiat. Prot. Dos. 69(2): 85-96.

Cross WG, Ing H, Freedman N. 1983. A short atlas of beta-ray spectra. Phys. Med. Biol. 28(11): 1251-1260.

Cross WG, Marr JD. 1960. Radiation Dosimetry. Atomic Energy of Canada Report 802: 58-60.

Cross WG, Wong PY, Freedman NO. 1991. Dose distributions for electrons and beta rays incident normally on water. Radiat. Prot. Dos. 35(2): 77-91.

de Boer SF, Beddar AS, Rawlinson JA. 1993. Optical filtering and spectral measurements of radiation-induced light in plastic scintillation dosimetry. Phys. Med. Biol. 38: 945-958.



de Sousa MC, Aubert B, Ricard M. 2000. Evaluation of physical performance of a scintillation dosimeter for patient dosimetry in diagnostic radiology. *Br. J. Radiol.* 73: 1297-1305.

Dorenbos P, de Haas JTM, van Eijk CWE. 1995. Non-proportionality in the scintillation response and the energy resolution obtainable with scintillation crystals. *IEEE Trans. on Nucl. Sci.* 42(6): 2190-2202.

Erkkila BH, Brake RJ, Waechter DA. 1983. Los Alamos portable Beta-ray spectrometer. NUREG/CP-0050: Proceedings of the International Beta Dosimetry Symposium.

Evans RD. 1955. *The Atomic Nucleus*. New York: McGraw-Hill. 972 p.

Falk F, Sparrman P. 1970. A computer method for the evaluation of the optical properties of scintillation detector assemblies. *Nucl. Inst. and Meth.* A85: 253-258.

Fell TP. 1991. A simple method for calculating skin dose from external beta emitters. *Radiat. Prot. Dos.* 36(1): 31-35.

Fernandes LMP, Lopes JAM, Monteiro CMB, dos Santos JMF, Morgado RE. 2002. Non-linear behavior of large-area avalanche photodiodes. *Nucl. Inst. and Meth.* A478: 395-399.

Flühs D, Heintz M, Indenkampen F, Wieczorek C. 1996. Direct reading measurement of absorbed dose with plastic scintillators- the general concept and applications to ophthalmic plaque dosimetry. *Med. Phys.* 23(3): 427-434.

Gelezunas VL, Siebt W, Huth G. 1977. Uniform large-area high-gain silicon avalanche radiation detectors from transmutation doped silicon. *Appl. Phys. Lett.* 30(2): 118-120.

Grozev PA, Vapirev EI, Botsova LI. 1992. Energy distribution of beta-particles transmitted through an absorber. *Appl. Radiat. Isot.* 43(3): 463-465.

Gualdrini GF, Padoani F. 1994. Monte Carlo code comparisons for the calculation of absorbed dose per unit fluence in slab phantoms for electron energies from 50 keV to 10 MeV. *Radiat. Prot. Dos.* 54(3/4): 203-207.

Hall EJ. 2000. *Radiobiology for the Radiologist* (5<sup>th</sup>). Philadelphia: Lippincott. 588 p.

Hirayama H. 1994. Calculation of absorbed dose at 0.07, 3.0 and 10.0 mm depths in a slab phantom for monoenergetic electrons. *Radiat. Prot. Dos.* 51(2): 107-124.

Horowitz YS, Horowitz A, Hirning CR, Yuen P, Cross W, Aikens M. 1993. The cog-beta ray spectrometer for mixed field beta/photon dosimetry. *Radiat. Prot. Dos.* 47(1/4): 415-418.

Huth GC, McKinney RA, Locker RJ. 1968. Development of a germanium avalanche-type semiconductor nuclear particle detector and discussion of avalanche detector arrays. *IEEE Trans. on Nucl. Sci.* 15: 246-251.

[ICRU] International Commission on Radiation Units and Measurements. 1994. Report 56, Dosimetry of External Beta Rays for Radiation Protection. Bethesda, MD.

Johnson KM. 1965. High-speed photodiode signal enhancement at avalanche breakdown voltage. *IEEE Trans. on Elec. Dev.* ED-12: 55-63.

Johnson LO, Alvarez L, Hoggan JM, Dickson RL. 1983. Pulse shape discrimination in a portable beta-gamma dose rate meter. *IEEE Trans. on Nucl. Sci.* NS-30(1): 543-546.

Kirkby DR, Delpy DT. 1996. Measurement of tissue temporal point spread function (TPSF) by use of a gain-modulated avalanche photodiode detector. *Phys. Med. Biol.* 41: 939-949.

Kirov AS, Hurlbut C, Dempsey J.F, Shrinivas SB, Epstein JW, Binns WR, Dowkontt PF, Williamson JF. 1999. Towards two-dimensional brachytherapy dosimetry using plastic scintillator: New highly efficient water equivalent plastic scintillator materials. *Med. Phys.* 26(8): 1515-1523.

Knoll GF. 2000. *Radiation Detection and Measurement (3<sup>rd</sup>)*. New York: J Wiley & Sons. 802 p.

Kobayashi S, Yamaoka K, Amami M, Kobayashi M. 1995. Evaluation of the avalanche photo diode (APD) as scintillation sensor. *Nucl. Inst. and Meth.* A364: 95-102.

Kocher DC, Eckerman KF. 1981. Electron dose-rate conversion factors for external exposure of the skin. *Health Phys.* 40(April): 467-475.

Koren B. 2001. A primer on photodiodes: The dominant technology for light detection applications. *OE Magazine.* 12(December).

Korzhik M, Khrutchinsky A, Lecoq P. 2002. The phenomenon of scintillation in solids. Nucl. Inst. and Meth. A486: 381-384.

Lecomte R, Martel C, Carrier C. 1989. Status of BGO-avalanche photodiode detectors for spectroscopic and timing measurements. Nucl. Inst. and Meth. A278: 585-597.

Lee TK, Sandison GA. 2003. The energy-dependent electron loss model: backscattering and application to heterogeneous slab media. Phys. Med. Biol. 48: 259-273.

Locker R. J, Huth GC. 1966. A new ionizing radiation detection concept which employs semiconductor avalanche multiplication and the tunnel diode element. Appl. Phys. Lett. 9(6): 227-230.

Loevinger R. 1950. Distribution of absorbed energy around a point source of beta radiation. Sci. 112(2914): 530-531.

Loevinger R. 1954. The dosimetry of beta radiations. Radiol. 62(January): 74-82.

Loevinger R. 1956. The dosimetry of beta sources in tissue. The point-source function. Radiol. 66(January): 55-62.

Lorenz E, Natkaniec S, Renker D, Schwartz B. 1994. Fast readout of plastic and crystal scintillators by avalanche photodiodes. Nucl. Inst. and Meth. A344: 64-72.

Lutz G. 1999. Semiconductor Radiation Detectors. Berlin: Springer-Verlag. 353 p.

Mainardi RT, Bonzi EV, Martinez VD. 1997. Design of tissue equivalent scintillators for precise dosimetry purposes. Radiat. Phys. Chem. 50(20): 159-163.

Martin JE. 2000. Physics for Radiation Protection. New York: J Wiley & Sons. 790 p.

Martz DE, Rich BL, Johnson LO. 1986. A portable beta spectrometer for tissue dose measurement. Radiat. Prot. Dos. 14(2): 183-186.

McIntyre RJ. 1966. Multiplication noise in uniform avalanche diodes. IEEE Trans. on Elec. Dev. ED-13(1): 164-168.

McKay KG, McAfee KB. 1953. Electron multiplication in silicon and germanium. *Phys. Rev.* 91(5): 1079-1084.

Merwin SE, Swinth KL. 1989. Performance of an exoelectron dosimeter badge for personnel beta dosimetry. *Radiat. Prot. Dos.* 28(3): 219-222.

Moszynski M, Czarnacki W, Kapusta M, Szawłowski M, Klamra W, Schotanus P. 2002. Energy resolution and light yield non-proportionality of pure NaI scintillator studied with large area avalanche photodiodes at liquid nitrogen temperatures. *Nucl. Inst. and Meth.* A486: 13-17.

Moszynski M, Kapusta M, Balcerzyk M, Szawłowski M, Wolski D, Wegrzecka I, Wegrzecka M. 2001a. Comparative study of avalanche photodiodes with different structures in scintillation detection. *IEEE Trans. on Nucl. Sci.* 48(4): 1205-1210.

Moszynski M, Kapusta M, Mayhugh M, Wolski D, Flyckt SO. 1997a. Absolute light output of scintillators. *IEEE Trans. on Nucl. Sci.* 44(3): 1052-1061.

Moszynski M, Kapusta M, Wolski D, Szawłowski M, Klamra W. 1997b. Blue enhanced large area avalanche photodiodes in scintillation detection with LSO, YAP and LuAP crystals. *IEEE Trans. on Nucl. Sci.* 44(3): 436-442.

Moszynski M, Kapusta M, Wolski D, Szawłowski M, Klamra W. 1998. Energy resolution of scintillation detectors readout with large area avalanche photodiodes and photomultipliers. *IEEE Trans. on Nucl. Sci.* 45(3): 472-477.

Moszynski M, Ludziejewski T, Wolski D, Klamra W, Norlin LO. 1994. Properties of the YAG scintillator. *Nucl. Inst. and Meth.* A345: 461-467.

Moszynski M, Ludziejewski T, Wolski D, Klamra W, Szawłowski M, Kapusta M. 1996. Subnanosecond timing with large area avalanche photodiodes and LSO scintillator. *IEEE Trans. on Nucl. Sci.* 43(3): 1298-1302.

Moszynski M, Szawłowski M, Kapusta M, Balcerzyk M. 2001b. Large area avalanche photodiodes in scintillation and x-rays detection. *Nucl. Inst. and Meth.* A485: 504-521.

Moszynski M, Szawłowski M, Kapusta M, Balcerzyk M, Wolski D. 2000. Large area avalanche photodiodes in x-rays and light detection. *IEEE Trans. on Nucl. Sci.* 47(4): 1297-1302.

[NIST] National Institute of Standards and Technology. 2004. Physical Reference Data: <http://physics.nist.gov/PhysRefData/Star/Text/ESTAR.html>.

Ochi A, Nishi Y, Tanimori T. 1996. Study of a large area avalanche photodiode as a fast photon and a soft X-ray detector. Nucl. Inst. and Meth. A378: 267-274.

Palazzolo M, Prati P, Ricco G, Taiuti M. 1992. A beta spectrometer for monitoring environmental matrices. Health Phys. 62(2): 155-161.

Pansart JP. 1997. Avalanche photodiodes for particle detection. Nucl. Inst. and Meth. A387: 186-193.

[RADAR] Radiation Dose Assessment Resource. 2003. <http://www.doseinfo-radar.com/RADARDecay.html>.

Reiff G, Squillante MR, Serreze HB, Entine G. 1983. Large area silicon avalanche photodiodes: Photomultiplier tube alternate. Mat. Res. Soc. Symp. Proc. 16: 131-140.

Renker D. 2002. Properties of avalanche photodiodes for applications in high energy physics, astrophysics and medical imaging. Nucl. Inst. and Meth. A486: 164-169.

Saleh BEA, Teich MC. 1991. Fundamentals of Photonics. New York: J Wiley & Sons. 966 p.

Schaart DR, Jansen JTM, Zoetelief J, de Leege PFA. 2002. A comparison of MCNP4C electron transport with ITS 3.0 and experiment at incident energies between 100 keV and 20 MeV: influence of voxel size, substeps and energy indexing algorithm. Phys. Med. Biol. 47: 1459-1484.

Schmelz C, Bradbury SM, Holl I, Lorenz E, Renker D, Ziegler S. 1995. Feasibility study of an avalanche photodiode readout for a high resolution PET with nsec time resolution. IEEE Trans. on Nucl. Sci. 42(4): 1080-1084.

Schorr MG, Torney FL. 1950. Solid non-crystalline scintillation phosphors. Phys. Rev. 80:474.

Selvi S, Celiktaş C. 2002. Revealing low-energy part of the beta spectra. Nucl. Inst. and Meth. A482: 449-456.

Shen L, Catchen GL, Levine SH. 1987. Experimental and computational techniques for b-particle dosimetry. Health Phys. 53(1): 37-47.

Shi Y, Wan B, Hu L, Sun Y, Liu S, Ling B. 2002. Application of avalanche photodiode for soft x-ray pulse-height analyses in the Ht-7 tokamak. *Nucl. Inst. and Meth. A488*: 566-571.

Simons GG, Higginbotham JF. 1990. Beta-particle spectroscopy with active gamma-ray discrimination. *Nucl. Inst. and Meth. A293*: 551-554.

Solovov VN, Hitachi A, Chepel V, Lopes MI, Ferreira Marques R, Policarpo AJPL. 2000. Detection of scintillation light of liquid xenon with a LAAPD. *Nuclear Science Symposium Conference Record, 2000 IEEE. 1*: 58-62.

Suffert M. 1992. Silicon photodiode readout of scintillators and associated electronics. *Nucl. Inst. and Meth. A322*: 523-528.

Swinth KL, Sisk DR, Simons GG. 1989. A proportional scintillation counter beta spectrometer. *IEEE Trans. on Nucl. Sci. 36(1)*: 1166-1171.

Sysoeva E, Tarasov V, Zelenskaya O. 2002. Comparison of the methods for determination of scintillation light yield. *Nucl. Inst. and Meth. A486*: 67-73.

Sze SM. 1981. *Physics of Semiconductor Devices*. New York: J Wiley & Sons. 523 p.

Vapirev EI, Jordanov T, Amin S, Stoilov N, Georgieva K. 1996. Scintillation spectroscopy for beta ray dose measurements. *Radiat. Prot. Dos. 64(4)*: 303-308.

Vargas WE, Niklasson GA. 1997. Pigment mass density and refractive index determination from optical measurements. *J. Phys.: Condens. Matter. 9*:1661-1670.

Watt DE, Alkharam AS. 1995. A feasibility study of scintillator microdosimeters for measurement of the biological effectiveness of ionising radiations. *Radiat. Prot. Dos. 61(1-3)*: 211-214.

Webb PP, McIntyre RJ. 1976. Large area reach-through avalanche diodes for x-ray spectroscopy. *IEEE Trans. on Nucl. Sci. NS-23(1)*: 138-144.

Williamson JF, Dempsey JF, Kirov AS, Monroe JI, Binns WR, Hedtjärn H. 1999. Plastic scintillator response to low-energy photons. *Phys. Med. Biol. 44*: 857-871.

## **APPENDICES**

## **APPENDIX A: MCNP INPUT FILES**

These MCNP input files are for the beta emitters  $^{36}\text{Cl}$ ,  $^{90}\text{Sr}$ ,  $^{90}\text{Y}$ , and  $^{210}\text{Bi}$ .

They all are for a source-detector distance of 10 mm, and cover the spectroscopy, surface dose and shallow dose configurations. Other source-detector distances can be obtained by simply changing the values associated with the detector position.

An example of an MCNP input file for creating the kernels used in the AFED removal algorithm is also attached.



```

Sr90 source in air, 10 mm from detector $Title card
10  0          -1      imp:e=0 $void to left of source
20  200 -1.40     1 -2 -5  imp:e=1 $mylar encapsulation
30  0          1 -2 5    imp:e=0 $void around encapsulation edges
40  400 -0.001293 2 -3 -7  imp:e=1 $air between source and detector
50  0          2 -3 7    imp:e=0 $void outside air gap
60  600 -1.032   3 -4 6    imp:e=1 $scintillator plastic
70  700 -1.19     3 -4 6 -7 imp:e=1 $lucite ring around scintillator
80  0          3 -4 7    imp:e=0 $void outside lucite
90  0          4        imp:e=0 $void to right of scintillator

1  PX -6.429E-4 $left encapsulation surface
2  PX 6.429E-4  $right encapsulation surface
3  PX 1.0      $detector face at x=10mm
4  PX 2.3      $layer of scintillator 13mm thick
5  CX 1.25     $encapsulation edge
6  CX 0.75     $scintillator cylinder
7  CX 1.0      $lucite ring cylinder

m200 1000 0.042 6000 0.625 8000 0.333 $mylar
m400 7000 0.8 8000 0.2          $air
m600 1000 0.526 6000 0.474      $scintillator PVT
m700 1000 0.533 6000 0.334 8000 0.133 $lucite
mode e                          $electron problem
c   Point source, Sr90, 29927 dpm $source comment
SDEF ERG=D1 WGT=1.79562e6        $source definition
SI1  A 1.37E-02 4.10E-02 6.83E-02 9.56E-02 1.23E-01
      1.50E-01 1.77E-01 2.05E-01 2.32E-01 2.59E-01
      2.87E-01 3.14E-01 3.41E-01 3.69E-01 3.96E-01
      4.23E-01 4.50E-01 4.78E-01 5.05E-01 5.32E-01
SP1   7.79E-02 7.60E-02 7.50E-02 7.40E-02 7.30E-02
      7.17E-02 7.01E-02 6.80E-02 6.53E-02 6.19E-02
      5.78E-02 5.27E-02 4.68E-02 4.01E-02 3.27E-02
      2.48E-02 1.71E-02 9.75E-03 4.28E-03 1.01E-03
F8:E 30
E8:E 0.002 298I 0.6
nps 1.79562E6 $1 hr
ctme 200

```

Fig. A.1: Strontium-90 spectroscopy configuration.

```

Cl-36 source in air, 10 mm from detector,full $Title card
10  0      -1      imp:e=0 $void to left of source
20  200 -1.40    1 -2 -5  imp:e=1 $mylar encapsulation
30  0      1 -2 5    imp:e=0 $void around encapsulation edges
40  400 -0.001293 2 -3 -7  imp:e=1 $air between source and detector
50  0      2 -3 7    imp:e=0 $void outside air gap
60  600 -1.032   3 -4 6    imp:e=1 $scintillator plastic
70  700 -1.19    3 -4 6 -7 imp:e=1 $lucite ring around scintillator
80  0      3 -4 7    imp:e=0 $void outside lucite
90  0      4      imp:e=0 $void to right of scintillator

1  PX -6.429E-4 $left encapsulation surface
2  PX 6.429E-4  $right encapsulation surface
3  PX 1.0      $detector face at x=10mm
4  PX 2.3      $layer of scintillator 13mm thick
5  CX 1.25     $encapsulation edge
6  CX 0.75     $scintillator cylinder
7  CX 1.0      $lucite ring cylinder

m200 1000 0.042 6000 0.625 8000 0.333 $mylar
m400  7000 0.8 8000 0.2      $air
m600  1000 0.526 6000 0.474  $scintillator PVT
m700  1000 0.533 6000 0.334 8000 0.133 $lucite
mode  e      $electron problem
c    Point source, Cl-36, 44400 dpm $source comment
SDEF  ERG=D1 WGT=2.664E6      $source definition
SI1   A 1.78e-02 5.32e-02 8.87e-02 1.24e-01 1.60e-01
      0.195 0.231 0.266 0.302 0.337
      0.373 0.408 0.443 0.479 0.514
      0.550 0.585 0.621 0.656 0.692
SP1   0.0523 0.0581 0.0626 0.0658 0.0680
      0.0694 0.0700 0.0697 0.0687 0.0666
      0.0634 0.0590 0.0534 0.0465 0.0386
      0.0299 0.0208 0.0122 0.00523 0.000847
F8:E  30      $pulses in cell 30 (scintillator)
E8:E  0.002 358I 0.72  $record pulses every 0.002 MeV
nps   2.664E6      $1 hr count
ctme  200

```

Fig. A.2: Chlorine-36 spectroscopy configuration.

```

Bi210 source in air, 10 mm from detector $Title card
10  0  -10          imp:e=0 $void to source's -x
20  200 -0.001293 9 -2 -6  imp:e=1 $air gap
25  0          9 -2 6  imp:e=0 $void
30  300 -1.032  2 -3 -5  imp:e=1 $scintillator plastic
40  400 -1.19   2 -3 5 -6 imp:e=1 $lucite ring
50  0          2 -3 6  imp:e=0 $void outside detector
70  0          3      imp:e=0 $void +x from end of detector
80  700 -1.40   8 -9 -7  imp:e=1 $mylar covering
90  900 -2.69  10 -8 -7  imp:e=1 $aluminum
92  0          10 -9 7  imp:e=0 $void

2  PX 1.0 $detector face at x=10mm
3  PX 2.3 $layer of scintillator 13mm thick
5  CX 0.75 $scintillator cylinder
6  CX 1.0 $lucite ring cylinder
7  CX 1.25 $mylar covering
8  PX -6.429E-4 $left cover
9  PX 6.429E-4 $right cover
10 PX -0.1 $aluminum backing

m200 7000 0.8 8000 0.2          $air
m300 1000 0.526 6000 0.474      $scintillator PVT
m400 1000 0.533 6000 0.334 8000 0.133 $lucite
m700 1000 0.363 6000 0.455 8000 0.182 $mylar
m900 13000 1.0                  $aluminum
mode e                          $electron problem
c  Point source, Bi210, 33207 dpm $source comment
SDEF ERG=D1 WGT=1.99244e6      $source definition
SI1  A 2.91E-02  8.72E-02 1.45E-01  2.03E-01 2.61E-01
      3.19E-01 3.78E-01 4.36E-01 4.94E-01 5.52E-01
      6.10E-01 6.68E-01 7.26E-01 7.84E-01 8.42E-01
      9.00E-01 9.58E-01 1.02E+00 1.07E+00 1.13E+00
SP1  7.59E-02  7.96E-02 8.19E-02 8.29E-02 8.24E-02
      8.06E-02 7.75E-02 7.32E-02 6.79E-02 6.17E-02
      5.48E-02 4.74E-02 3.97E-02 3.20E-02 2.45E-02
      1.75E-02 1.12E-02 6.16E-03 2.33E-03 4.22E-04
F8:E 30
E8:E 0.002 579I 1.162
nps 1.99244E6 $1 hr
ctme 200

```

Fig. A.3: Bismuth-210 spectroscopy input file.

```

Y90 source in air, 10 mm from detector $Title card
10  0      -1      imp:e=0 $void to left of source
20  200 -1.40    1 -2 -5  imp:e=1 $mylar encapsulation
30  0      1 -2 5    imp:e=0 $void around encapsulation edges
40  400 -0.001293 2 -3 -7  imp:e=1 $air between source and detector
50  0      2 -3 7    imp:e=0 $void outside air gap
60  600 -1.032   3 -4 6    imp:e=1 $scintillator plastic
70  700 -1.19    3 -4 6 -7 imp:e=1 $lucite ring around scintillator
80  0      3 -4 7    imp:e=0 $void outside lucite
90  0      4      imp:e=0 $void to right of scintillator

1  PX -6.429E-4 $left encapsulation surface
2  PX 6.429E-4  $right encapsulation surface
3  PX 1.0      $detector face at x=10mm
4  PX 2.3      $layer of scintillator 13mm thick
5  CX 1.25     $encapsulation edge
6  CX 0.75     $scintillator cylinder
7  CX 1.0      $lucite ring cylinder

m200 1000 0.042 6000 0.625 8000 0.333 $mylar
m400 7000 0.8 8000 0.2      $air
m600 1000 0.526 6000 0.474  $scintillator PVT
m700 1000 0.533 6000 0.334 8000 0.133 $lucite
mode e      $electron problem
c  Point source, Y90, 29927 dpm  $source comment
SDEF ERG=D1 WGT=1.79562e6      $source definition
SI1  A 5.71E-02 1.71E-01 2.86E-01 4.00E-01 5.14E-01
      6.28E-01 7.42E-01 8.57E-01 9.71E-01 1.08
      1.20 1.31 1.43 1.54 1.66
      1.77 1.88 2.00 2.11 2.23
SP1  4.26E-02 5.18E-02 5.94E-02 6.49E-02 6.86E-02
      7.08E-02 7.17E-02 7.15E-02 7.04E-02 6.85E-02
      6.57E-02 6.19E-02 5.69E-02 5.07E-02 4.30E-02
      3.42E-02 2.46E-02 1.50E-02 6.43E-03 1.13E-03
F8:E 30
E8:E 0.002 1148I 2.3
nps 1.79562E6 $1 hr
ctme 200

```

Fig. A.4: Yttrium-90 spectroscopy input file.

Sr-90 source in air, 10 mm from detector,surface dose \$Title card

```

10  0  -8          imp:e=0 $void to source's -x
20  200 -0.001293 9 -2  imp:e=1 $air gap
30  300 -1.032  2 -3 -5  imp:e=1 $scintillator plastic
35  350 -1.19   3 -4 -5  imp:e=1 $plastic backing
40  400 -1.19   2 -4 5 -6 imp:e=1 $lucite ring
50  0         2 -4 6  imp:e=0 $void outside detector
70  0         4       imp:e=0 $void +x from end of detector
80  700 -1.40   8 -9 -7  imp:e=1 $mylar covering
90  800 -0.001293 8 -9 7  imp:e=1 $air

```

```

2  PX 1.0 $detector face at x=10mm
3  PX 1.1 $layer of scintillator 1mm thick
4  PX 2.3 $inert plastic backing 12 mm thick
5  CX 0.75 $scintillator cylinder
6  CX 1.0 $lucite ring cylinder
7  CX 1.25 $mylar covering
8  PX -6.429E-4 $left cover
9  PX 6.429E-4 $right cover

```

```

m200  7000 0.8 8000 0.2          $air
m300  1000 0.526 6000 0.474      $scintillator PVT
m350  1000 0.533 6000 0.334 8000 0.133 $plastic backing
m400  1000 0.533 6000 0.334 8000 0.133 $lucite
m700  1000 0.042 6000 0.625 8000 0.333 $mylar
m800  7000 0.8 8000 0.2          $air
mode  e          $electron problem
c  Point source, Sr90, 29927 dpm  $source comment
SDEF  ERG=D1 WGT=1.79562e6      $source definition
SI1  A 1.37E-02 4.10E-02 6.83E-02 9.56E-02 1.23E-01
      1.50E-01 1.77E-01 2.05E-01 2.32E-01 2.59E-01
      2.87E-01 3.14E-01 3.41E-01 3.69E-01 3.96E-01
      4.23E-01 4.50E-01 4.78E-01 5.05E-01 5.32E-01
SP1  7.79E-02 7.60E-02 7.50E-02 7.40E-02 7.30E-02
      7.17E-02 7.01E-02 6.80E-02 6.53E-02 6.19E-02
      5.78E-02 5.27E-02 4.68E-02 4.01E-02 3.27E-02
      2.48E-02 1.71E-02 9.75E-03 4.28E-03 1.01E-03
F8:E  30          $pulses in cell 30 (scintillator)
E8:E  0.002 298I 0.6  $record pulses
nps  1.79562e6      $1 hr count
ctme  200

```

Fig. A.5: Strontium-90 surface dose MCNP input file.

```

Cl-36 source in air, 10 mm from detector,surface dose $Title card
10  0  -8          imp:e=0 $void to source's -x
20  200 -0.001293 9 -2    imp:e=1 $air gap
30  300 -1.032   2 -3 -5  imp:e=1 $scintillator plastic
40  400 -1.19    2 -4 5 -6 imp:e=1 $lucite ring
50  0          2 -4 6    imp:e=0 $void outside detector
60  600 -1.19    3 -4 -5  imp:e=1 $inert plastic
70  0          4        imp:e=0 $void +x from end of detector
80  700 -1.40    8 -9 -7  imp:e=1 $mylar covering
90  800 -0.001293 8 -9 7   imp:e=1 $air

2  PX 1.0 $detector face at x=10mm
3  PX 1.1 $layer of scintillator 1mm thick
4  PX 2.3 $layer of inert plastic 12mm thick, for backscatter
5  CX 0.75 $scintillator cylinder
6  CX 1.0 $lucite ring cylinder
7  CX 1.25 $mylar covering
8  PX -6.429E-4 $left cover
9  PX 6.429E-4 $right cover

m200  7000 0.8 8000 0.2          $air
m300  1000 0.526 6000 0.474      $scintillator PVT
m400  1000 0.533 6000 0.334 8000 0.133 $lucite
m600  1000 0.533 6000 0.334 8000 0.133 $BC802 (methyl methacrylate,lucite)
m700  1000 0.042 6000 0.625 8000 0.333 $mylar
m800  7000 0.8 8000 0.2          $air
mode  e                      $electron problem
c    Point source, Cl-36, 44400 dpm $source comment
SDEF  ERG=D1 WGT=2.664E6          $source definition
SI1   A 1.78e-02 5.32e-02 8.87e-02 1.24e-01 1.60e-01
      0.195 0.231 0.266 0.302 0.337
      0.373 0.408 0.443 0.479 0.514
      0.550 0.585 0.621 0.656 0.692
SP1   0.0523 0.0581 0.0626 0.0658 0.0680
      0.0694 0.0700 0.0697 0.0687 0.0666
      0.0634 0.0590 0.0534 0.0465 0.0386
      0.0299 0.0208 0.0122 0.00523 0.000847
F8:E  30          $pulses in cell 30 (scintillator)
E8:E  0.002 358I 0.720 $record pulses every 0.002 MeV
nps   2.664E6
ctme  200

```

Fig. A.6: Chlorine-36 surface dose MCNP input file.

```

Bi210 source in air, 10 mm from detector,surface dose $Title card
10  0  -10          imp:e=0 $void to source's -x
20  200 -0.001293 9 -2 -6  imp:e=1 $air gap
25  0          9 -2 6  imp:e=0 $void
30  300 -1.032  2 -3 -5  imp:e=1 $scintillator plastic
35  350 -1.19   3 -4 -5  imp:e=1 $plastic backing
40  400 -1.19   2 -4 5 -6 imp:e=1 $lucite ring
50  0          2 -4 6  imp:e=0 $void outside detector
70  0          4          imp:e=0 $void +x from end of detector
80  700 -1.40   8 -9 -7  imp:e=1 $mylar covering
90  900 -2.69  10 -8 -7  imp:e=1 $aluminum
92  0          10 -9 7  imp:e=0 $void
2   PX 1.0 $detector face at x=10mm
3   PX 1.1 $layer of scintillator 1mm thick
4   PX 2.3 $inert plastic backing 12 mm thick
5   CX 0.75 $scintillator cylinder
6   CX 1.0 $lucite ring cylinder
7   CX 1.25 $mylar covering
8   PX -6.429E-4 $left cover
9   PX 6.429E-4 $right cover
10  PX -.01    $aluminum backing
m200 7000 0.8 8000 0.2          $air
m300 1000 0.526 6000 0.474          $scintillator PVT
m350 1000 0.533 6000 0.334 8000 0.133 $plastic backing
m400 1000 0.533 6000 0.334 8000 0.133 $lucite
m700 1000 0.363 6000 0.455 8000 0.182 $mylar
m900 13000 1.0          $aluminum
mode e          $electron problem
c   Point source, Bi210, 33207 dpm  $source comment
SDEF ERG=D1 WGT=1.99244e6          $source definition
SI1  A 2.91E-02 8.72E-02 1.45E-01 2.03E-01 2.61E-01
      3.19E-01 3.78E-01 4.36E-01 4.94E-01 5.52E-01
      6.10E-01 6.68E-01 7.26E-01 7.84E-01 8.42E-01
      9.00E-01 9.58E-01 1.02E+00 1.07E+00 1.13E+00
SP1  7.59E-02 7.96E-02 8.19E-02 8.29E-02 8.24E-02
      8.06E-02 7.75E-02 7.32E-02 6.79E-02 6.17E-02
      5.48E-02 4.74E-02 3.97E-02 3.20E-02 2.45E-02
      1.75E-02 1.12E-02 6.16E-03 2.33E-03 4.22E-04
F8:E 30
E8:E 0.002 579I 1.162
nps 1.99244E6  $1 hr
ctme 200

```

Fig. A.7: Bismuth-210 surface dose MCNP input file.

Y-90 source in air, 10 mm from detector,surface dose \$Title card

```

10  0  -8          imp:e=0 $void to source's -x
20  200 -0.001293 9 -2    imp:e=1 $air gap
30  300 -1.032   2 -3 -5  imp:e=1 $scintillator plastic
35  350 -1.19    3 -4 -5  imp:e=1 $plastic backing
40  400 -1.19    2 -4 5 -6 imp:e=1 $lucite ring
50  0          2 -4 6    imp:e=0 $void outside detector
70  0          4          imp:e=0 $void +x from end of detector
80  700 -1.40    8 -9 -7  imp:e=1 $mylar covering
90  800 -0.001293 8 -9 7   imp:e=1 $air

```

```

2  PX 1.0 $detector face at x=10mm
3  PX 1.1 $layer of scintillator 1mm thick
4  PX 2.3 $inert plastic backing 12 mm thick
5  CX 0.75 $scintillator cylinder
6  CX 1.0 $lucite ring cylinder
7  CX 1.25 $mylar covering
8  PX -6.429E-4 $left cover
9  PX 6.429E-4 $right cover

```

```

m200  7000 0.8 8000 0.2          $air
m300  1000 0.526 6000 0.474      $scintillator PVT
m350  1000 0.533 6000 0.334 8000 0.133 $plastic backing
m400  1000 0.533 6000 0.334 8000 0.133 $lucite
m700  1000 0.363 6000 0.455 8000 0.182 $mylar
m800  7000 0.8 8000 0.2          $air
mode  e          $electron problem
c  Point source, Y90, 29927 dpm  $source comment
SDEF  ERG=D1 WGT=1.79562e6      $source definition
SI1  A 5.71E-02 1.71E-01 2.86E-01 4.00E-01 5.14E-01
      6.28E-01 7.42E-01 8.57E-01 9.71E-01 1.08
      1.20  1.31  1.43  1.54  1.66
      1.77  1.88  2.00  2.11  2.23
SP1  4.26E-02 5.18E-02 5.94E-02 6.49E-02 6.86E-02
      7.08E-02 7.17E-02 7.15E-02 7.04E-02 6.85E-02
      6.57E-02 6.19E-02 5.69E-02 5.07E-02 4.30E-02
      3.42E-02 2.46E-02 1.50E-02 6.43E-03 1.13E-03
F8:E  30          $pulses in cell 30 (scintillator)
E8:E  0.0020568 1116I 2.2995024  $record pulses
nps  1.79562e6      $1 hr count
ctme  200

```

Fig. A.8: Yttrium-90 surface dose MCNP input file.



```

Sr-90 source in air, 10 mm from detector,shallow dose $Title card
10  0  -8          imp:e=0 $void to source's -x
20  200 -0.001293 9 -1  imp:e=1 $air gap
30  300 -1.19   1 -2 -5  imp:e=1 $inert plastic
35  350 -1.032  2 -3 -5  imp:e=1 $scintillator
40  400 -1.19   3 -4 -5  imp:e=1 $inert plastic
45  450 -1.19   1 -4 5 -6 imp:e=1 $lucite ring
50  0          1 -4 6  imp:e=0 $void outside detector
70  0          4          imp:e=0 $void +x from end of detector
80  700 -1.40   8 -9 -7  imp:e=1 $mylar covering
90  800 -0.001293 8 -9 7  imp:e=1 $air
1  PX 1.0 $detector face at x=10mm
2  PX 1.1 $inert layer
3  PX 1.3 $layer of scintillator 2mm thick
4  PX 2.3 $inert plastic backing 10 mm thick
5  CX 0.75 $scintillator cylinder
6  CX 1.0 $lucite ring cylinder
7  CX 1.25 $mylar covering
8  PX -6.429E-4 $left cover
9  PX 6.429E-4 $right cover
m200 7000 0.8 8000 0.2          $air
m300 1000 0.533 6000 0.334 8000 0.133 $inert plastic
m350 1000 0.526 6000 0.474          $scintillator PVT
m400 1000 0.533 6000 0.334 8000 0.133 $inert plastic
m450 1000 0.533 6000 0.334 8000 0.133 $lucite
m700 1000 0.042 6000 0.625 8000 0.333 $mylar
m800 7000 0.8 8000 0.2          $air
mode e          $electron problem
c  Point source, Sr90, 29927 dpm  $source comment
SDEF ERG=D1 WGT=1.79562e6          $source definition
SI1  A 1.37E-02 4.10E-02 6.83E-02 9.56E-02 1.23E-01
      1.50E-01 1.77E-01 2.05E-01 2.32E-01 2.59E-01
      2.87E-01 3.14E-01 3.41E-01 3.69E-01 3.96E-01
      4.23E-01 4.50E-01 4.78E-01 5.05E-01 5.32E-01
SP1   7.79E-02 7.60E-02 7.50E-02 7.40E-02 7.30E-02
      7.17E-02 7.01E-02 6.80E-02 6.53E-02 6.19E-02
      5.78E-02 5.27E-02 4.68E-02 4.01E-02 3.27E-02
      2.48E-02 1.71E-02 9.75E-03 4.28E-03 1.01E-03
F8:E 35          $pulses in cell 35 (scintillator)
E8:E 0.002 2981 0.6  $record pulses
nps 1.79562e6          $1 hr count
ctme 200

```

Fig. A.9: Strontium-90 shallow dose MCNP input file.

```

Cl-36 source in air, 10 mm from detector,shallow dose $Title card
10  0  -8          imp:e=0 $void to source's -x
20  200 -0.001293 9 -2  imp:e=1 $air gap
30  300 -1.032  10 -3 -5 imp:e=1 $scintillator plastic
40  400 -1.19   2 -4 5 -6 imp:e=1 $lucite ring
50  0         2 -4 6  imp:e=0 $void outside detector
60  600 -1.19   3 -4 -5 imp:e=1 $inert plastic
70  0         4       imp:e=0 $void +x from end of detector
80  700 -1.40   8 -9 -7 imp:e=1 $mylar covering
90  800 -0.001293 8 -9 7  imp:e=1 $air
95  900 -1.19   2 -10 -5 imp:e=1 $inert front layer
2   PX 1.0  $detector face at x=10mm
3   PX 1.3  $layer of scintillator 2mm thick
4   PX 2.3  $layer of inert plastic 10mm thick, for backscatter
5   CX 0.75 $scintillator cylinder
6   CX 1.0  $lucite ring cylinder
7   CX 1.25 $mylar covering
8   PX -6.429E-4 $left cover
9   PX 6.429E-4  $right cover
10  PX 1.1  $inert plastic 1mm thick
m200 7000 0.8 8000 0.2          $air
m300 1000 0.526 6000 0.474      $scintillator PVT
m400 1000 0.533 6000 0.334 8000 0.133 $lucite
m600 1000 0.533 6000 0.334 8000 0.133 $BC802 (methyl methacrylate,lucite)
m700 1000 0.042 6000 0.625 8000 0.333 $mylar
m800 7000 0.8 8000 0.2          $air
m900 1000 0.533 6000 0.334 8000 0.133 $BC802 (methyl methacrylate,lucite)
mode e          $electron problem
c   Point source, Cl-36, 44400 dpm $source comment
SDEF ERG=D1 WGT=2.664E6          $source definition
SI1  A 1.78e-02 5.32e-02 8.87e-02 1.24e-01 1.60e-01
      0.195 0.231 0.266 0.302 0.337
      0.373 0.408 0.443 0.479 0.514
      0.550 0.585 0.621 0.656 0.692
SP1  0.0523 0.0581 0.0626 0.0658 0.0680
      0.0694 0.0700 0.0697 0.0687 0.0666
      0.0634 0.0590 0.0534 0.0465 0.0386
      0.0299 0.0208 0.0122 0.00523 0.000847
F8:E 30          $pulses in cell 30 (scintillator)
E8:E 0.002 358I 0.72  $record pulses every 0.002 MeV
nps 2.664E6
ctme 200

```

Fig. A.10: Chlorine-36 shallow dose MCNP input file.

```

Bi210 source in air, 10 mm from detector,shallow dose $Title card
10  0  -10          imp:e=0 $void to source's -x
20  200 -0.001293 9 -1 -6  imp:e=1 $air gap
25  0      9 -1 6  imp:e=0 $void
30  300 -1.19   1 -2 -5  imp:e=1 $inert front plastic
35  350 -1.032   2 -3 -5  imp:e=1 $scintillator
38  380 -1.19   3 -4 -5  imp:e=1 $inert backing
40  400 -1.19   1 -4 5 -6 imp:e=1 $lucite ring
50  0      1 -4 6  imp:e=0 $void outside detector
70  0      4      imp:e=0 $void +x from end of detector
80  700 -1.40   8 -9 -7  imp:e=1 $mylar covering
90  900 -2.69  10 -8 -7  imp:e=1 $aluminum
92  0      10 -9 7  imp:e=0 $void
1   PX 1.0 $front of detector
2   PX 1.1 $layer of inert plastic
3   PX 1.3 $layer of scint plastic 2mm thick
4   PX 2.3 $inert plastic backing 10 mm thick
5   CX 0.75 $scintillator cylinder
6   CX 1.0 $lucite ring cylinder
7   CX 1.25 $mylar covering
8   PX -6.429E-4 $left cover
9   PX 6.429E-4 $right cover
10  PX -.01   $aluminum backing
m200 7000 0.8 8000 0.2          $air
m300 1000 0.533 6000 0.334 8000 0.133 $plastic front
m350 1000 0.526 6000 0.474          $scintillator PVT
m380 1000 0.533 6000 0.334 8000 0.133 $plastic backing
m400 1000 0.533 6000 0.334 8000 0.133 $lucite
m700 1000 0.363 6000 0.455 8000 0.182 $mylar
m900 13000 1.0          $aluminum
mode e          $electron problem

```

Fig. A.11: Bismuth-210 shallow dose MCNP input file.

Fig. A.11: (Continued)

SDEF ERG=D1 WGT=1.99244e6 \$source definition  
 SII A 2.91E-02 8.72E-02 1.45E-01 2.03E-01 2.61E-01  
 3.19E-01 3.78E-01 4.36E-01 4.94E-01 5.52E-01  
 6.10E-01 6.68E-01 7.26E-01 7.84E-01 8.42E-01  
 9.00E-01 9.58E-01 1.02E+00 1.07E+00 1.13E+00  
 SP1 7.59E-02 7.96E-02 8.19E-02 8.29E-02 8.24E-02  
 8.06E-02 7.75E-02 7.32E-02 6.79E-02 6.17E-02  
 5.48E-02 4.74E-02 3.97E-02 3.20E-02 2.45E-02  
 1.75E-02 1.12E-02 6.16E-03 2.33E-03 4.22E-04  
 F8:E 35  
 E8:E 0.002 579I 1.162  
 nps 1.99244E6 \$1 hr

```

Y-90 source in air, 10 mm from detector,shallow dose $Title card
10  0  -8          imp:e=0 $void to source's -x
20  200 -0.001293 9 -1  imp:e=1 $air gap
30  300 -1.19   1 -2 -5  imp:e=1 $inert plastic
35  350 -1.032  2 -3 -5  imp:e=1 $scintillator
40  400 -1.19   3 -4 -5  imp:e=1 $inert plastic
45  450 -1.19   1 -4 5 -6 imp:e=1 $lucite ring
50  0          1 -4 6  imp:e=0 $void outside detector
70  0          4          imp:e=0 $void +x from end of detector
80  700 -1.40   8 -9 -7  imp:e=1 $mylar covering
90  800 -0.001293 8 -9 7  imp:e=1 $air
1   PX 1.0  $detector face at x=10mm
2   PX 1.1  $inert layer
3   PX 1.3  $layer of scintillator 2mm thick
4   PX 2.3  $inert plastic backing 10 mm thick
5   CX 0.75 $scintillator cylinder
6   CX 1.0  $lucite ring cylinder
7   CX 1.25 $mylar covering
8   PX -6.429E-4 $left cover
9   PX 6.429E-4 $right cover
m200 7000 0.8 8000 0.2          $air
m300 1000 0.533 6000 0.334 8000 0.133 $inert plastic
m350 1000 0.526 6000 0.474          $scintillator PVT
m400 1000 0.533 6000 0.334 8000 0.133 $inert plastic
m450 1000 0.533 6000 0.334 8000 0.133 $lucite
m700 1000 0.042 6000 0.625 8000 0.333 $mylar
m800 7000 0.8 8000 0.2          $air
mode e          $electron problem
c   Point source, Y90, 29927 dpm  $source comment
SDEF ERG=D1 WGT=1.79562e6          $source definition
SI1  A 5.71E-02 1.71E-01 2.86E-01 4.00E-01 5.14E-01
      6.28E-01 7.42E-01 8.57E-01 9.71E-01 1.08
      1.20  1.31  1.43  1.54  1.66
      1.77  1.88  2.00  2.11  2.23
SP1  4.26E-02 5.18E-02 5.94E-02 6.49E-02 6.86E-02
      7.08E-02 7.17E-02 7.15E-02 7.04E-02 6.85E-02
      6.57E-02 6.19E-02 5.69E-02 5.07E-02 4.30E-02
      3.42E-02 2.46E-02 1.50E-02 6.43E-03 1.13E-03
F8:E 35          $pulses in cell 35 (scintillator)
E8:E 0.002 1148I 2.3  $record pulses
nps 1.79562e6          $1 hr count
ctme 200

```

Fig. A.12: Yttrium-90 shallow dose MCNP input file.

Monoenergetic source in void, 10 mm from detector \$Title card

```

10  100 -1.032  1 -4 -3  imp:e=1 $scintillator plastic
20  0      2 -1 -3  imp:e=1 $void
30  0      -2      imp:e=0 $void
40  0      2 -1 3  imp:e=0 $void
50  0      4      imp:e=0 $void
60  0      1 -4 3  imp:e=0 $void

```

```

1  PX 1.0 $plane 10mm from source
2  PX -.1 $plane behind source
3  CX 0.75 $cylinder
4  PX 2.3 $right plane

```

```

m100  1000 0.526 6000 0.474      $scintillator PVT
mode  e                      $electron problem
c    monoenergetic source      $source comment
SDEF  ERG=0.08 WGT=1000000      $source definition
F8:E  10
E8:E  0 .002 38I 0.08
nps  1000000
ctme  200

```

Fig. A.13: Kernel calculation MCNP input file.

## APPENDIX B: MATHEMATICA PROGRAM FOR IMPLEMENTING THE AFED REMOVAL ALGORITHM

```

data[1] = Import["C:\Kernel_data\eff100.txt", "List"]; (*import all primary kernels*)
data[2] = Import["C:\Kernel_data\eff200.txt", "List"];
data[3] = Import["C:\Kernel_data\eff300.txt", "List"];
data[4] = Import["C:\Kernel_data\eff400.txt", "List"];
data[5] = Import["C:\Kernel_data\eff500.txt", "List"];
data[6] = Import["C:\Kernel_data\eff600.txt", "List"];
data[7] = Import["C:\Kernel_data\eff700.txt", "List"];
data[8] = Import["C:\Kernel_data\eff800.txt", "List"];
data[9] = Import["C:\Kernel_data\eff900.txt", "List"];
data[10] = Import["C:\Kernel_data\eff1000.txt", "List"];
data[11] = Import["C:\Kernel_data\eff1100.txt", "List"];
data[12] = Import["C:\Kernel_data\eff1200.txt", "List"];
data[13] = Import["C:\Kernel_data\eff1300.txt", "List"];
data[14] = Import["C:\Kernel_data\eff1400.txt", "List"];
data[15] = Import["C:\Kernel_data\eff1500.txt", "List"];
data[16] = Import["C:\Kernel_data\eff1600.txt", "List"];
data[17] = Import["C:\Kernel_data\eff1700.txt", "List"];
data[18] = Import["C:\Kernel_data\eff1800.txt", "List"];
data[19] = Import["C:\Kernel_data\eff1900.txt", "List"];
data[20] = Import["C:\Kernel_data\eff2000.txt", "List"];
data[21] = Import["C:\Kernel_data\eff2100.txt", "List"];
data[22] = Import["C:\Kernel_data\eff2200.txt", "List"];
data[23] = Import["C:\Kernel_data\eff2300.txt", "List"];
initspectrum = Import["C:\Kernel_data\Mylar_spectra\Sry.txt", "List"];
(*initspectrum is the spectrum that includes all scatter and edge effects*)

spectrum=initspectrum;
maxkern=Floor[2 Length[spectrum]/100]+1 (*determine highest energy kernel
needed*)

Do[spectrum=Append[spectrum,0],{n,1,Length[data[maxkern]]-Length[spectrum]};
Do[initspectrum=Append[initspectrum,0],{n,1,Length[data[maxkern]]-
Length[initspectrum]}; (*all lists must be of the same length*)

Length[initspectrum]
Length[data[maxkern]] (*verify lengths are equal*)

maxfracs = Import["C:\Kernel_data\max_fracs.txt", "List"]; (*primary kernel maximum
fractions*)

```

```

Do[Do[data[i]=Append[data[i],0],{n,Length[data[maxkern]]-
Length[data[i]]},{i,maxkern-1}] (*pad with zeros to make lengths equal*)

energymax=2290; (*Maximum beta energy; multiple of 2 only, keV; User specified*)
energymmin = 100; (*Don't change this; first pass is done 100 keV and up*)

(*Enhance spectrum from 100 keV up to Emax*)
For[energy=energymax,energy>=energymmin, energy=energy-2,
  a=Mod[energy/100,1];
  b=energy/100-a;
  upperkernel=data[b+1];
  lowerkernel=data[b];
  kernel=(upperkernel-lowerkernel)*a+lowerkernel;
  peakfrac=(maxfracs[[b+1]]-maxfracs[[b]])*a+maxfracs[[b]];
  spectrum[[energy/2]]=spectrum[[energy/2]]/peakfrac;
  spectrum=spectrum-kernel*spectrum[[energy/2]];
  Clear[upperkernel]; Clear[lowerkernel]; Clear[kernel];]; (*end of for loop*)

<<Graphics`MultipleListPlot` (*Standard add-on package*)

(*observe effects after first pass; adjust plot range as needed*)
firstpass=MultipleListPlot[initpectrum,spectrum,
  AxesLabel->{Channel,Events},
  PlotJoined->False,
  SymbolStyle->{Hue[0.67],Hue[0.95]},
  PlotLegend->{"Original","Modified"},
  LegendPosition->{0.45,0.15},
  LegendSize->{.5,3},
  PlotRange->{{0,1500},{0,2000}},
  AxesOrigin->{0,0}]

highpectrum=spectrum; (*preserve changes so far*)

(*import kernels from 20 to 80 keV*)
data[20] = Import["C:\Kernel_data\eff020.txt","List"];
data[40] = Import["C:\Kernel_data\eff040.txt","List"];
data[60] = Import["C:\Kernel_data\eff060.txt","List"];
data[80] = Import["C:\Kernel_data\eff080.txt","List"];
data[100]=data[1];

(*max fracs for low-E kernels*)
lowmaxfracs={0.947924, 0.944117, 0.939980, 0.935675, 0.932273};

```



```
Do[Do[data[20*j]=Append[data[20*j],0],{n,Length[data[maxkern]]-
Length[data[20*j]]}],{j,4}>(*make lists same length*)
```

```
lowenmax=98; (*don't change*)
lowenmin=20; (*don't change*)
```

```
(*enhance spectrum from 20 to 98 keV*)
For[lowenergy=lowenmax,lowenergy≥lowenmin, lowenergy=lowenergy-2,
  a=20*Mod[lowenergy/20,1];
  b=lowenergy-a;
  upperkernel=data[b+20];
  lowerkernel=data[b];
  c=a/20;
  d=b/20;
  kernel=(upperkernel-lowerkernel)*c+lowerkernel;
  lowpeakfrac=(lowmaxfracs[[d+1]]-lowmaxfracs[[d]])*c+lowmaxfracs[[d]];
  spectrum[[lowenergy/2]]=spectrum[[lowenergy/2]]/lowpeakfrac;
  spectrum=spectrum-kernel*spectrum[[lowenergy/2]];
  Clear[upperkernel]; Clear[lowerkernel]; Clear[kernel];]; (*end of for loop*)
```

```
(*import data from spherical detector*)
sphericaldata = Import["C:\Kernel_data\Spherical_data\SrY90_sphere.txt","List"];
```

```
(*put lists in proper form for plotting*)
initial=Table[{2*i,initpectrum[[i]]},{i,1,Length[initpectrum]}];
final=Table[{2*i,spectrum[[i]]},{i,1,Length[spectrum]}];
ideal=Table[{2*i,sphericaldata[[i]]},{i,1,Length[sphericaldata]}];
```

```
(*plot results compared to initial spectrum*)
finalresult=MultipleListPlot[initial,final,
AxesLabel->{"Energy[keV]",Events},
PlotJoined->False,
SymbolStyle->{GrayLevel[0.1],GrayLevel[0.5]},
PlotLegend->{"Detector","Final"},
LegendPosition->{0.45,0.15},
LegendSize->{.5,.3},
SymbolShape->{PlotSymbol[Diamond,3],PlotSymbol[Star,3],PlotSymbol[Box,2]},
PlotRange->{{0,170},{0,5000}},
AxesOrigin->{0,0},
TextStyle->{FontSize->14},
ImageSize->{576,500}]
```

```
Export["B:\Anglefigs\Flat_sphere\yttrium.jpg",finalresult,ImageSize-> 72
6.75,ImageResolution->300] (*save plot as a JPEG*)
```

```
(*import theoretical spectrum for comparison*)
theoenergy=Import["C:\Kernel_data\Theoretical_spectra\Y90_energies.txt","List"];
theoprob=Import["C:\Kernel_data\Theoretical_spectra\Y90_probs.txt","List"];
theoenergy=1000 theoenergy; (*don't change*)
theoprob=3200 theoprob; (*adjust as necessary*)
theospectrum=Table[{theoenergy[[i]],theoprob[[i]]},{i,1,Length[theoenergy]}];
```

```
(*plot initial, processed, and theoretical spectra*)
spectracompare=MultipleListPlot[initial,final,theospectrum,
AxesLabel->{"Energy[keV]",Events},
PlotJoined->{False,False,False},
SymbolStyle->{GrayLevel[0.1],GrayLevel[0.5],GrayLevel[0.1]},
PlotLegend->{"Detector","Processed","Theory"},
PlotStyle->{Thickness[0.007]},
LegendPosition->{0.45,0.15},
LegendSize->{.5,.3},
SymbolShape->{PlotSymbol[Diamond,2.5,Filled->True],
PlotSymbol[Star,3],
PlotSymbol[Box,3,Filled->True]},
PlotRange->{{0,2300},{0,2000}},
AxesOrigin->{0,0},
TextStyle->{FontSize->14},
ImageSize->{576,500}]
```

```
Export["D:\Dissertation\Figures\Spectra\Sry_mylar.jpg",spectracompare,ImageSize->
72 6.75,ImageResolution->300] (*save as a JPEG*)
```